1.1 QUANTUM DYNAMICS DIVISION

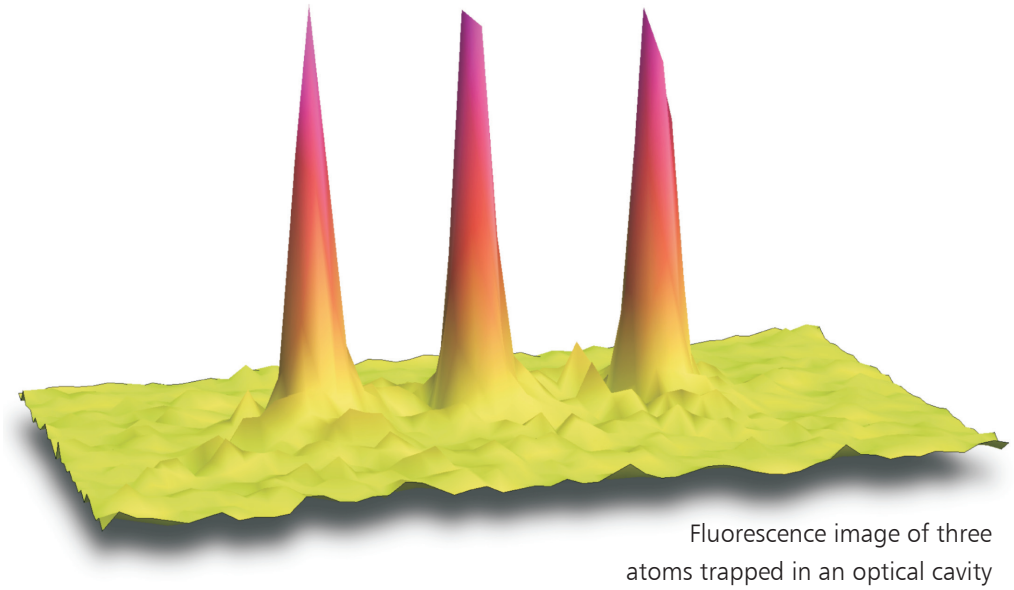

Fluorescence image of three atoms trapped in an optical cavity

Prof. Gerhard Rempe

GROUP MEMBERS

SCIENTIFIC STAFF

- L. D. van Buuren
- S. Dürr
- D. L. Moehring
- K. Murr
- P. W. H. Pinkse
- A. Ourjoumtsev
- S. C. Webster*

(* took new position during report period)

PH.D. CANDIDATES

- D. M. Bauer
- J. Bochmann
- M. Hijlkema*
- M. Koch
- A. Kubanek
- M. Lettner
- M. Motsch
- M. Mücke
- T. Puppe*
- T. Rieger*
- C. Sames
- I. Schuster
- C. Sommer
- H. Specht
- N. Syassen*
- C. Vo
- T. Volz*
- B. Weber
- T. Wilk*
- M. Zeppenfeld

(* received Ph.D. during report period)

DIPLOMA CANDIDATES

- C. Erbel*
- D. Dietze*
- A. Fuhrmanek*
- B. Hagemann
- G. Langfahl-Klabes*,
- T. Müller*
- S. Pohle*
- M. Schenk*

(* received Diploma during report period)

SCIENTIFIC COLLABORATORS

- J. I. Cirac (Garching, Germany)
- J. Bulthuis (Amsterdam, Netherlands)
- J.-J. Garcia-Ripoll (Madrid, Spain)
- T. Köhler (Oxford, UK)
- A. Kuhn (Oxford, UK)
- P. Maunz (Maryland, USA)
- W. L. Meerts (Nijmegen, Netherlands)
- G. Morigi (Barcelona, Spain)
- S. A. Rangwala (Bangalore, India)
- M. Schmitt (Düsseldorf, Germany)
- R. de Vivie-Riedle (Munich, Germany)

JUNIOR RESEARCH GROUP

- T. Schätz
  - Ph.D. candidates:
    - A. Friedenauer
    - S. Kahra
    - H. Schmitz
    - C. Schneider
  - Diploma candidates:
    - R. Matjeschk

1.1.1 SUMMARY OF SCIENTIFIC ACTIVITIES

The group's research activities focus on the experimental and theoretical investigation of fundamental quantum effects in a broad range of research fields including

- Bose-Einstein condensation,
- cavity quantum electrodynamics,
- quantum information science,
- cold molecules.

Highlights include but are not limited to the first

- realization of a quantum state with exactly one molecule at each site of an optical lattice,
- demonstration of a coherent superposition between atom pairs and molecules,
- realization of a one-dimensional strongly correlated gas of bosonic molecules,
- observation of a quantum-Zeno effect in the tunnelling of ultracold molecules,
- implementation of a genuine quantum protocol with one-and-only-one neutral atom,
- demonstration of a quasi-deterministic quantum interface between an atom and a photon,
- generation of a sequence of entangled photons on the push of a button,
- observation of a genuine quantum state with one atom bound to two optical photons.

All these achievements have so far been obtained exclusively in our group. This success would have been impossible without the indefatigable commitment of a great team of co-workers.

1.1.1.1 BOSE-EINSTEIN CONDENSATION

Ultracold molecules in optical lattices offer novel ways to create strongly-correlated quantum systems. A variety of exotic quantum phases have been predicted with properties strikingly different from those studied in the terrain of weakly interacting quantum systems. In the past two years, we focused our activities on the preparation of ultracold molecules in optical lattices and the exploration of the character of these many-body quantum systems. In these studies, we clearly reached the strongly-correlated regime.

PREPARATION OF A QUANTUM STATE WITH EXACTLY ONE MOLECULE AT EACH SITE OF AN OPTICAL LATTICE

Densities in ultracold atomic gases are usually very small. Experiments are therefore in the weakly-correlated regime, with interactions between the particles so weak that the ensemble can well be described by a mean-field theory. The strongly-correlated regime can be reached by applying an optical lattice which reduces the volume that is available to the particles and, hence, increases the effective density. A landmark experiment in this field was the creation of an atomic Mott insulator in 2002. We now managed, so far as the only group worldwide, to prepare a similar quantum state for molecules, namely a state that contains exactly one molecule at each site of an optical lattice [1,2]. This is achieved by first creating an atomic Mott insulator with a central region that contains exactly two atoms at each lattice site and then associating molecules using a Feshbach resonance. Pairs of atoms at the same site are converted into molecules with conversion efficiency close to unity. This central region of the optical lattice is surrounded by a shell of lattice sites containing one atom each. These isolated atoms are not affected by the Feshbach resonance. After associating molecules in the centre, the remaining atoms are removed from the sample using a microwave field and radiation pressure from a laser that is resonant with an atomic transition. The experimental data shown in Figure 1 demonstrate that the desired quantum state is actually prepared.

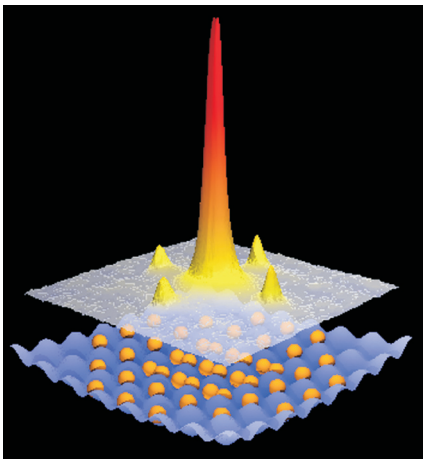

Figure 1: Quantum state with one molecule at each lattice site. An optical lattice (blue) is loaded such that the central region contains two atoms at each site. A surrounding shell contains one atom per site. A Feshbach resonance is used to associate the atom pairs to molecules. The properties of the system are inferred from measured momentum distributions, such as the one shown at the top [1].

This state offers a variety of fascinating perspectives. First, laser-induced Raman transitions could be used to transfer the molecules into their internal ground state. By lowering the lattice, one could then produce a Bose-Einstein condensate of ground-state molecules.

Second, when performing the same experiment with heteronuclear molecules associated from a mixture of two different species, the ground-state molecules might have a substantial electric dipole-dipole interaction, making the observation of novel quantum phases possible and opening up perspectives for quantum information processing.

ATOM-MOLECULE OSCILLATIONS IN A MOTT INSULATOR

The molecule association technique in Ref. [1] relies on a slow ramp of the magnetic field across the Feshbach resonance. Alternatively, the magnetic field can be jumped from an off-resonant value onto the Feshbach resonance. This induces temporal oscillations between free atom pairs and bound molecules, as shown in Figure 2. We experimentally observe up to 29 periods of large-amplitude atom-molecule oscillations [3].

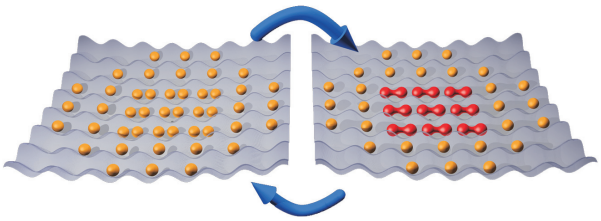

Figure 2: Atom molecule oscillations in a Mott insulator. A sudden jump of the magnetic field onto a Feshbach resonance is used to induce temporal oscillations between free atom pairs and bound molecules in an optical lattice [3].

STRONG DISSIPATION INHIBITS LOSSES AND INDUCES STRONG CORRELATIONS IN COLD MOLECULAR GASES

In all quantum-gas experiments so far, the strongly-correlated regime was reached by employing strong elastic interactions and weak inelastic interactions. The latter produces losses. We have now shown that strong inelastic interactions can inhibit particle losses by driving the system into the strongly-correlated regime [4].
Molecules associated from bosonic atoms, such as the ^{87}Rb atoms in our experiment, have large rate coefficients for inelastic molecule-molecule collisions [5]. We load our optical lattice with exactly one molecule per site. We then lower the lattice along one spatial dimension, thus allowing the molecules to tunnel between different sites and explore their inelastic interactions. We find that the resulting one-dimensional gas closely resembles a Tonks-Girardeau gas, where strong elastic interactions prevent particles from being at the same position. In our experiment, the strong inelastic interactions lead to a reflection of the particles off each other, creating a state that is described by the same wave function as a Tonks-Girardeau gas. The physical origin of this reflection can be understood from an analogy to Fresnel's formulas in classical optics or as a manifestation of the continuous quantum Zeno effect [4].

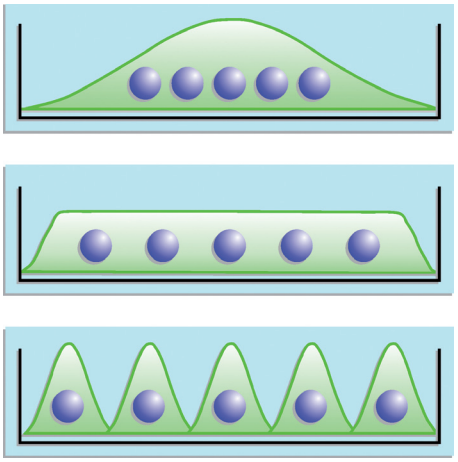

Figure 3: Strongly correlated state in one spatial dimension. Top: Noninteracting particles in a box all occupy the same wave function. Middle: For weak repulsion, the density distribution is deformed, but the particles still all occupy the same wave function. Bottom: For strong repulsion, a Tonks gas is obtained, where no two particles occupy the same wave function. We drive the system into such a strongly-correlated state using inelastic instead of elastic interactions [4].

1.1.1.2 CAVITY QUANTUM ELECTRODYNAMICS

A two-state atom interacting with a resonant mode of the radiation field is the elementary system underlying the Einstein theory of spontaneous and stimulated emission. In its modern conception the physics of this system is more subtle, however, than Einstein anticipated. According to quantum theory, the interaction produces new energy states, with the property that for strong coupling photons and atoms loose their individual identity. The aim of our project is to investigate such a system in theory and experiment. We routinely operate in the strong-coupling regime with single atoms trapped in a high-quality cavity and cooled with novel cavity-enhanced light forces [6,7].
We have now extended our trapping technique by implementing a blue intracavity dipole trap [8]. This trap has the unique advantage that an atom stored in the cavity is hardly perturbed by the trapping light. With the good control we have over the system, we have also been able to demonstrate for the first time the existence

of a quantum state made of one atom and two optical photons [9]. Such a state has no classical analogue and has been observed in a nonlinear spectroscopy technique developed in our group.

BLUE TRAP AND DISPERSIVE OBSERVATION OF SINGLE ATOMS

An established tool to localize an atom in the cavity mode is the optical dipole trap. So far only red-detuned dipole traps have been demonstrated in cavity quantum electrodynamics (QED). Since the atom is trapped at regions of high intensities, the atomic energy levels experience an unwanted light shift. This does not occur for a blue-detuned dipole trap. The idea of this trap is to use detuned cavity modes to shape a potential landscape which realizes three-dimensional confinement around a dark trap centre, see Figure 4. Strong coupling and a light shift much smaller than the trap height is directly observed in the transmission spectra. As a practical application, we demonstrated that an atom can reliably and near-instantaneously be detected without scattering spontaneous photons [8].

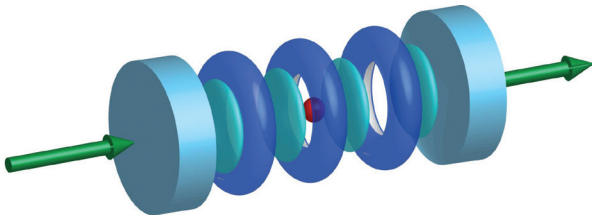

Figure 4: A blue intracavity dipole trap has a dark centre. This leaves the energy levels of the atom (red) at their unperturbed value [8].

NONLINEAR SPECTROSCOPY OF PHOTONS BOUND TO ONE ATOM

Under the condition of strong coupling a system composed of a single atom and a single cavity mode has properties which are distinctively different from those of the bare atom (without the cavity), or the bare cavity (without the atom), or just the sum of the two. In fact the composite system has its own characteristic energy spectrum. This spectrum consists of an infinite ladder of pairs of states, the dressed states. Observations of the lowest excited state doublet of the compound atom-cavity system were first reported for atomic beams, and in our group with a single atom. This doublet, however, arises wherever two coupled classical oscillators model the linear interaction between the radiation field and matter.
The next higher-lying doublet contains two quanta of energy and lacks a classical explanation. Such a state is multiphotonic in nature (see Figure 5) and therefore has intrinsic nonlinear properties. For decades, this nonlinearity has been searched for without success. We have now resolved such a state and have shown that it responds nonlinearly to the input excitation. The agreement with quantum theory is remarkable, and at the same time in sharp discord with classical theory [9]. Our findings open up the new research field of nonlinear cavity QED.

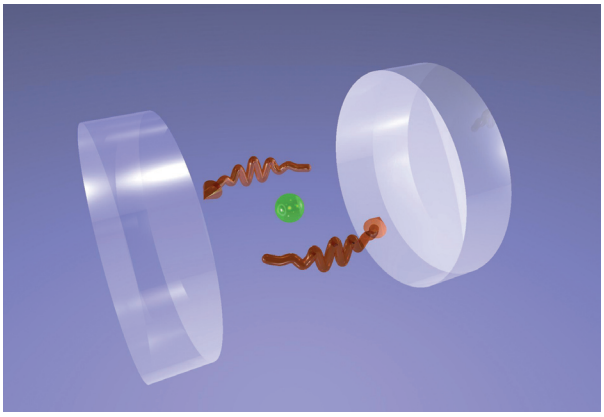

Figure 5: One atom (green) bound to two photons (red) between two highly reflecting mirrors [9].

Future experiments will focus on the quantum properties of the light emitted by the atom-cavity system in the quantum-nonlinear regime. This requires a better control over the atomic motion. Towards this end, we constructed a new cavity with better optical access for cooling and better length-control capabilities without compromising on mirror quality or coupling strength.

1.1.1.3 QUANTUM INFORMATION PROCESSING

In addition to studying fundamental quantum physics, cavity QED systems are promising tools for scalable quantum information processing. We have achieved much progress here, including the first demonstration of entanglement generation between an intracavity atom and single emitted photons. We have also demonstrated an efficient single-photon server with one-and-only-one *trapped* atom coupled to an optical cavity. Both of these experiments pave the way for the realization of a distributed quantum network.

POLARIZATION CONTROLLED SINGLE PHOTONS

Critical to the development of a distributed quantum processor is to establish a link between stationary memory qubits (atoms) and travelling messenger qubits

(photons). Building on our well established procedure of single photon generation using vacuum-stimulated Raman transitions [10], we realized a fundamental requirement for atom-photon entanglement by efficiently producing single photons with a controllable polarization [11]. As the experimental protocol used in these experiments had well defined initial and final states, the efficiency of single photon production could be greatly increased compared to previous experiments, in this case as high as 41%.

SINGLE-ATOM SINGLE-PHOTON QUANTUM INTERFACE

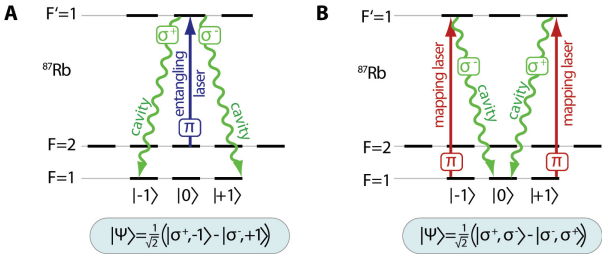

Figure 6: Entanglement and state mapping, with laser and cavity driving vacuum-stimulated Raman adiabatic passages. (A) Creation of atom-photon entanglement. (B) Atomic state mapping onto a second photon. At the end of the protocol, the entanglement is shared between two flying photons, with the atom disentangled [12].

Controlled generation of photons of well defined polarization allows for further demonstration of an entangled atom-photon quantum interface. To this end, we have successfully entangled a single atom with a single emitted photon and have further mapped the quantum state of the atom onto a second photon [12]. After state preparation, the triggered emission of a first photon entangles the internal state of the atom and the polarization state of the photon. The entanglement generation is measured by mapping the quantum state of the atom onto the polarization state of a second emitted photon, see Figure 6. By analyzing the polarization state of the two emitted photons, we confirm that the atom-photon and two-photon systems are indeed entangled. While previous experiments with atoms in free space have demonstrated atom-photon entanglement, ours was the first to demonstrate qubit state mapping from a single atomic qubit to a single photon.

We have further shown first steps towards local control of the atomic qubit, which may allow for the creation of multi-photon and/or multi-atom entangled states. The strong coupling of the atom to the cavity mode makes these schemes intrinsically deterministic, establishing the basic element required to realize a distributed quantum network with atoms and photons.

SINGLE-PHOTON SERVER WITH ONE TRAPPED ATOM

In order to achieve *scalable* distributed entanglement, it is important for the interaction time between the atom and the cavity to be sufficiently long compared to the time necessary for atomic state manipulations and remote atom entanglement. By combining our cavity QED experience with techniques for trapping single atoms, we have increased our interaction time between the atom and the cavity by up to six orders of magnitude compared to our falling-atom experiment [13]. Together with the highly efficient atom-photon entanglement schemes discussed above, this allows for near deterministic multi-particle entanglement.

The first step for generating atom-photon entanglement from our trapped-atom-cavity system is to demonstrate a source of single photons. With our long trapping times, we are able to generate and characterize a single photon source with one-and-only-one atom [14]. This is demonstrated by exciting the atom-cavity system with a sequence of laser pulses and analyzing the emitted photon stream with single-photon detectors. The quality of the source is specified by its intensity correlation function evaluated during a short time interval after system preparation, and its subsequent performance can be granted for up to a minute (Figure 7).

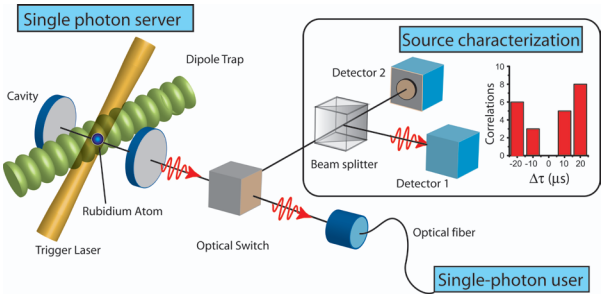

Figure 7: Illustration of a single-photon server. The performance of the system as a source of single photons is repeatedly monitored and assured for the end user [14].

We have also implemented an imaging system to laser address and monitor intracavity atoms with micrometer resolution, see Figure 8. This system also allows for the confirmation of a single atom in real time, important for future multi-atom entanglement protocols.

We are currently in the process of scaling to multiple atom-cavity systems in order to establish an entanglement between different quantum nodes. This requires the construction of additional apparatuses

capable of trapping a single atom within a second high-finesse cavity. During the last year, we have assembled and characterized such a completely independent apparatus. All the relevant lasers have been implemented and measured atom-storage times compare well to our existing system. It should therefore be possible to efficiently generate entanglement between two remotely-located atom-cavity systems in the near future.

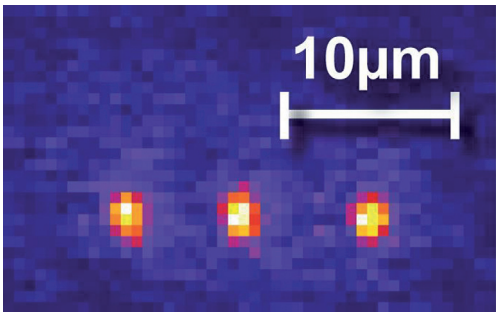

Figure 8: High resolution image of a register of three rubidium atoms trapped within our high-finesse cavity.

1.1.1.4 COLD POLAR MOLECULES

The research field of cold molecules promises new chemistry in a domain where the kinetic energy is no longer available to activate a reaction. Cold polar molecules are also good candidates for the implementation of quantum-information processing schemes and the investigation of fundamental symmetries of nature. We have developed a robust technique to separate slow molecules from fast molecules of a thermal effusive source. The slow molecules are electrically guided over large distances into a separate vacuum chamber for further studies [15,16]. High fluxes at low velocities have been achieved. Several laboratories worldwide have started to set up similar sources.
Molecules from a thermal source still occupy many rotational states. In the last two years we have developed a laser-based method to measure the rotational distribution in our guided beam. Moreover, we have built a new cryogenic source which reduces the velocity and the internal temperature of the molecules by collisions with a cold helium buffer gas.

HIGH-RESOLUTION SPECTROSCOPY OF FORMALDEHYDE

To be able to perform state-selective detection of cold molecules, high-resolution room-temperature spectroscopy of our prototype molecule, formaldehyde (H_2CO), was necessary as the literature data were not of sufficient accuracy. Doppler-limited absorption spectra of two complete vibrational bands were obtained, and the states involved in the transitions were assigned, thus improving the knowledge about the molecular constants [17]. Although the electronic transitions in H_2CO in the near ultraviolet are weak and the excited states dissociate, we managed to measure several lines Doppler free by means of saturation spectroscopy [18].

STATE-SELECTIVE SPECTROSCOPIC DETECTION

With the insight obtained from the high-resolution spectroscopy, we have developed an optical pumping technique which allows us to remove molecules in a well-defined rotational state from the electric guide. This is achieved by means of a continuous-wave ultraviolet laser (see Figure 9) which transfers the molecules either into a state which is not guided or which dissociates. By monitoring the resulting decrease of the molecular flux we have determined the rotational distribution of the most abundant states in our guided beam of H_2CO. Our findings are well explained by theory [19]. As the guide allows the laser beam to be collinear with the molecules over a significant length, the method is well suited for high-resolution spectroscopy of weak transitions.

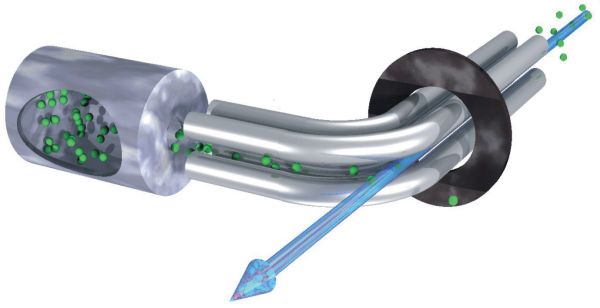

Figure 9: State-selective depletion spectroscopy. A continuous-wave laser beam collinear with the guided molecules depletes the beam from molecules in a certain internal state by optical pumping [19].

ELECTROSTATIC EXTRACTION OF MOLECULES FROM A CRYOGENIC BUFFER GAS

In order to reduce the number of populated states, we have constructed a new source in which warm molecules are injected into a cryogenic helium buffer gas, see Figure 10. By collisions with the helium, the external and the internal degrees of freedom of the molecules are cooled. Through an exit hole, the cooled molecules as well as the helium atoms escape from the cell. Here, the polar molecules are picked up by

the electrostatic guide. The source is operational and produces a flux comparable with the previous setup but with a much higher state purity. In fact, with depletion spectroscopy we estimate that the contribution of the highest populated state can exceed 80%, whereas the population of that state at 300 K is only 2%.

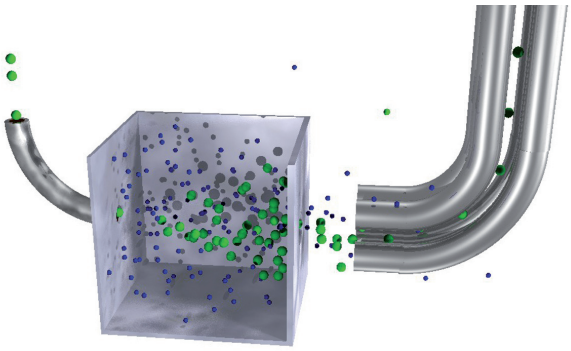

Figure 10: Warm molecules (green) are introduced into a cryogenic cell via a heated capillary. In the cell, they are cooled by collisions with the cold helium gas (blue). Both gases exit the cell through an aperture, but only the polar molecules are guided out of the cryostat by the electric guide.

ELECTRODYNAMIC TRAPPING OF LASER-COOLED ATOMS

Further cooling of cold molecules might be possible by sympathetic cooling with laser-cooled ultracold atoms. To explore the possibility of trapping atoms and molecules in the same spatial region, we set up an electric trap for atoms. In contrast to polar molecules, atoms in low-lying states cannot be trapped with static electric fields. Hence, alternating electric fields are required. However, the small polarizability of atoms makes the atomic traps extremely shallow, with trap depths of the order of a few 10 μK. Nevertheless we have been able to store laser-cooled atoms in an all-electric trap with the configuration outlined in Figure 11 [20]. Apart from offering the perspective of studying collisions between cold molecules and ultracold atoms, our technique might also find applications in metrology.

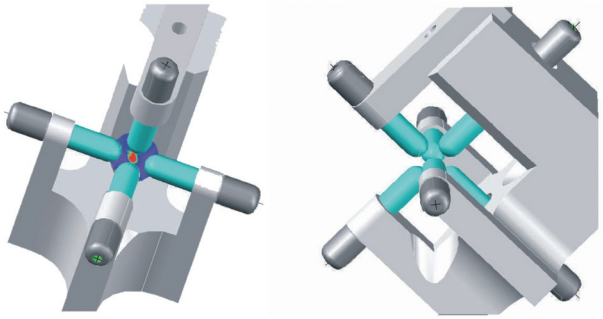

Figure 11: The alternating electric field trap seen at two different angles. On the left, a small picture of the atomic cloud is shown in red [20].

SIMULATION OF CAVITY COOLING OF MOLECULES

An alternative approach to laser cool molecules is cavity cooling. Here, particles are coupled to a high-finesse cavity with a slightly higher frequency than the laser. The cavity decay offers a channel of dissipation not relying on spontaneous emission of the molecules. In principle, any particle can be cooled. We showed that this method of cooling the molecular motion can be extended to include cooling of the internal degrees of freedom such as rotation and vibration. We have simulated this method for OH [21] and NO [22] and showed that with enough laser power and in a sufficiently good cavity, the molecules can be cooled down to one or two internal states.

REFERENCES

[1] T. Volz et al.; *Nature Physics* **2**, 692 (2006).
[2] S. Dürr et al.; *Atomic Physics* ICAP **20**, 278 (2006).
[3] N. Syassen et al.; *Phys. Rev. Lett.* **99**, 033201 (2007).
[4] N. Syassen et al.; *Science* **320**, 1329 (2008).
[5] N. Syassen et al.; *Phys. Rev. A* **74**, 062706 (2006).
[6] K. Murr et al.; *Phys. Rev. A* **74**, 043412 (2006).
[7] T. Puppe et al.; *J. Mod. Opt.* **54**, 1927 (2007).
[8] T. Puppe et al.; *Phys. Rev. Lett.* **99**, 013002 (2007).
[9] I. Schuster et al.; *Nature Physics* **4**, 382 (2008).
[10] A. Kuhn et al.; *Phys. Rev. Lett.* **89**, 067901 (2002).
[11] T. Wilk et al.; *Phys. Rev. Lett.* **98**, 063601 (2007).
[12] T. Wilk et al.; *Science* **317**, 488 (2007).
[13] S. Nussmann et al.; *Nature Physics* **1**,122 (2005); *Phys. Rev. Lett.* **95**, 173602 (2005).
[14] M. Hijlkema et al.; *Nature Physics* **3**, 253 (2007).
[15] S.A. Rangwala et al.; *Phys. Rev. A* **67**, 043406 (2003).
[16] T. Junglen et al.; *Eur. Phys. J. D* **31**, 365 (2004).
[17] M. Motsch et al.; arXiv:0804.0207.
[18] M. Zeppenfeld et al.; *Appl. Phys. B* **89**, 475 (2007).
[19] M. Motsch et al.; *Phys. Rev. A* **76**, 061402(R) (2007).
[20] T. Rieger et al.; *Phys. Rev. Lett.* **99**, 063001 (2007).
[21] G. Morigi et al.; *Phys. Rev. Lett.* **99**, 073001 (2007).
[22] M. Kowalewski et al.; *Appl. Phys. B* **89**, 459 (2007).

JUNIOR RESEARCH GROUP (DFG / MPQ)

1.1.1.5 "QUANTUM SIMULATIONS WITH TRAPPED IONS"

Leader: Dr. T. Schätz

We can not translate quantum behaviour arising with superposition states or entanglement efficiently into the classical language of conventional computers [1]. A universal quantum computer could describe and help to understand complex quantum systems. But it is envisioned to become functional only within the next decade(s).
A shortcut was proposed via simulating the quantum behaviour of interest in another quantum system, where all relevant parameters and interactions can be controlled and observables of interest detected sufficiently well [1].
Instead of translating quantum dynamics into an algorithm of stroboscopic quantum gate operations to run them on a universal quantum computer, we want to continuously control and manipulate the spins, equivalent to the way nature evolves the system of our interest.
Already a comparably small amount of simulation-spins, of the order of 30-50, are supposed to be sufficient to outperform classical computers [2]. In addition, the fidelities of the proposed operations are predicted to be sufficiently high in state of the art experiments and do not have to be performed within very demanding fault tolerant limits for universal quantum computation [3].

THE ION TRAP QUANTUM SIMULATOR

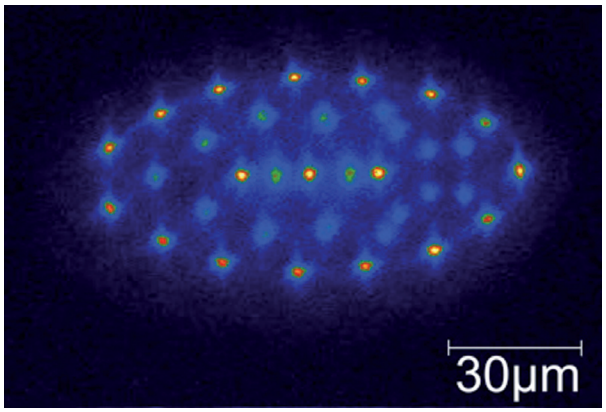

Figure 1: Fluorescence light of a 3D Coulomb crystal - 35 laser cooled $^{25}Mg^{+}$ ions in the experimental zone of our segmented linear Paul-trap, depicted in Figure 2. In our first experiments we are dealing with linear chains of ions only. To realize 2D grids of ions (spins) for 2D quantum simulations we will investigate new trap designs – e.g. trap arrays on surfaces displayed in Figure 3.

Our system comprises magnesium ions, confined in a linear Paul trap [4]. It can simulate Quantum spin Hamiltonians, describing many solid-state systems like magnets, high-Tc superconductors, quantum Hall ferromagnets, ferroelectrics, et cetera. For our feasibility study we aim for the simulation of the Quantum Ising Hamiltonian realizing the proposal of Porras and Cirac [3].
Two electronic levels of each ion span a two-level system that can be interpreted (simulates) as a spin ½ particle. Those are very well isolated from external disturbances. To provide controlled interaction with and between the simulated spins we apply rf- and laser-fields respectively.

TECHNICAL PROGRESS

In January 2006 we had trapped our first ions and Doppler cooled them via our two times frequency doubled fibre-laser system [5]. Subsequently, we setup two additional fibre laser systems for coherent control of $^{25}Mg^{+}$ spins and realized the detection of the ions with a spatial resolution $< 1\ \mu$m.
We set up a real time coherent experimental control and data acquisition. In December 2006 we achieved state-sensitive detection (fidelity $>$ 99%), coherent transitions in $^{25}Mg^{+}$ (fidelity $>$ 99%) and motional ground state cooling of the axial motion ($<n>\sim$ 0,01) [4]. We could verify sufficiently low motional heating rate (axial motion: dn/dt~0.01 quanta/ms), optimized our operational fidelities and reduced decoherence until June 2007 to the results given in brackets. In the following we implemented a state-dependant optical dipole force (to allow for the simulation of spin-spin interaction or the implementation of phase-gates.

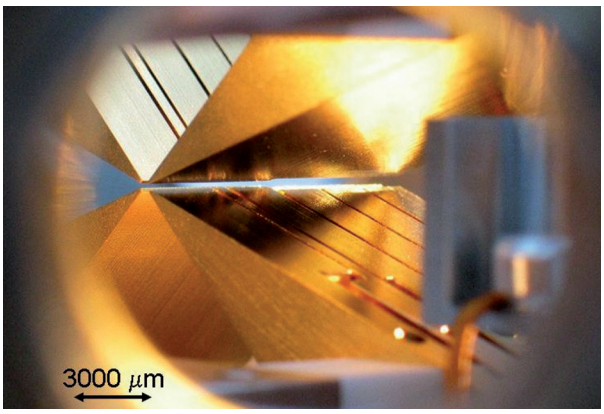

Figure 2: View through a laser port on our segmented ion trap. Two wedge-shaped radio-frequency (RF) electrodes and two segmented DC-electrodes provide the radial and axial confinement respectively.

EXPERIMENTAL RESULTS ON THE SIMULATION OF A QUANTUM MAGNET

To calibrate our operational fidelities, we implemented a geometric phase gate [6] and prepared an entangled Bell state of two ions with a fidelity exceeding 95% in November 2007.
Subsequently, we experimentally simulated the adiabatic evolution of the smallest non-trivial spin system from the paramagnetic into the (anti-)ferromagnetic order with a quantum magnetisation for two spins of 98% [7]. We proved that the observed transition is not driven by thermal-fluctuations but of quantum mechanical origin, the source of quantum-fluctuations in quantum phase transitions. We observed a final superposition state of the two degenerate spin configurations for the ferromagnetic ($|\uparrow\uparrow\rangle+|\downarrow\downarrow\rangle$) and the anti-ferromagnetic ($|\downarrow\uparrow\rangle+|\uparrow\downarrow\rangle$) order, respectively. These correspond to deterministically entangled states achieved with a fidelity up to 88%.
Our work demonstrates the building blocks for simulating quantum spin-Hamiltonians with trapped ions.

OUTLOOK

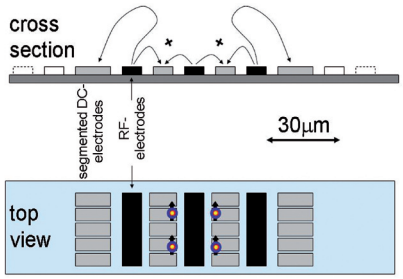

Figure 3: Schematic view of an ion trap with the RF- (black bars) and segmented DC-electrodes projected on a surface. We plan to position segmented linear ion traps at a distance that allows for stiff single ion confinement and a Coulomb interaction between ions being similar in two dimensions. If we were able to master the technical challenges we could construct a two-dimensional trap array and test the scalability for two-dimensional quantum simulations.

We will explore the limits of our one dimensional approach by investigating the dynamics for an increased amount of spins, simulating larger spins and altering the duration of the simulation.
Our experimental setup provides us with the necessary tools to approach a set of additional simulation problems we will try to access, like the strong correlation between bosons [8], the quantum-random-walk [9], the particle production in our early universe [10,11] or relativistic effects described by the Dirac equation [12].

Based on new ion-trap technology it seems to become feasible to scale the ion simulator to a larger amount of spins and into two dimensions in surface trap arrays. Here we could investigate quantum simulations on two dimensional spin-grids, e.g. spin-frustration.
Experts in the field allow us to hope, starting from arrays spanned by 10x10 ions, to provide new insight into quantum dynamics. We aim to observe effects that represent Quantum-Phase Transitions for many-particle systems.
The possibility to control all the parameters of the system individually by switching laser beams and/or trap voltages and to address each single spin on each single lattice site turn it into a versatile system offering tools for analysis overcoming the access in experiments on solid-state systems

TRAPPED IONS AND MOLECULES

In close collaboration with the group of Prof. Rempe we founded an additional group to investigate in a separate experimental setup, depicted schematically in Figure 4, whether laser cooled atomic ions and cold neutral molecules can be guided and even trapped in the same apparatus to study their mutual interaction.
In collaboration with the Attosecond and High-Field Phsics Division and the MAP-collaboration [14] the group is planning to use an equivalent apparatus for loading, trapping and sympathetic laser cooling of (internally cold) orientated molecular ions to study fast dynamical changes triggered by femtosecond laser pulses via electron/X-ray scattering.
The investigation of the dynamics within a molecule during a structural change on the relevant timescale ($<$10 fs) gets into reach due to the development of new generation MAP-light sources that might provide pulses containing more than 10^{11} photons at wavelengths promising a resolution on atomic length scales. We should become enabled to record a diffraction pattern from a single molecule without the need of crystalline periodicity. The three-dimensional time-resolved structure could be retrieved from the diffraction patterns, if the destroyed molecule can be replaced by identically prepared copies being pounded one after the other.
But besides the brilliant work necessary to supply the photons or further on produced electrons at the required intensities we have to provide reproducible and precise methods at sufficient repetition rates to prepare and handle the molecular target of interest.

TECHNICAL PROGRESS

Until June 2006, we investigated the feasibility of the sympathetic cooling and the separation of single molecular ions from a larger Coulomb crystal in the trap

of the quantum simulation experiment described above. We realized separation cycles of close to 100% fidelity.
Starting in June 2006, the group designed and built the experimental apparatus, consisting of a bent linear rf-guide traversing two differential pumping stages to reach the final UHV-chamber where the experimental trap is located (see Figure 4). The setup was finished in January 2008. In parallel, we completed the laser setup and frequency doubling cavities to provide the necessary cooling and photo-ionization wavelengths.
Being aware of the fact that we will investigate charged molecules we will take advantage of elaborate schemes to append additional atoms to be ionized, not to disturb the dynamics of the molecule under investigation or to protonate, simulating in some cases a natural surrounding. From January to May 2008, we installed a refurbished electro spray ionization source to provide molecular ions in an up to now separate setup.

OUTLOOK

Until the end of 2008 we are planning to load ions in both ancilla-traps (see chamber C1 and C3 in Figure 4)

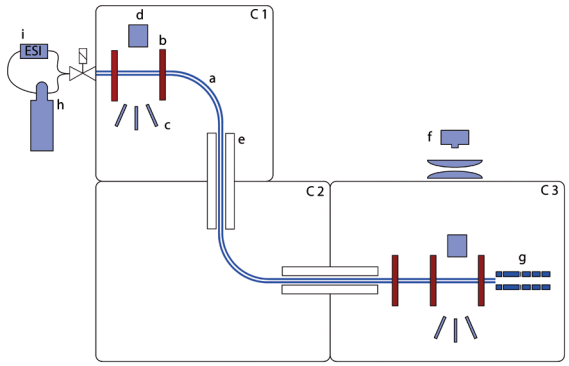

Figure 4: Schematic view of the (ion) guide – total length ~500mm. Four RF-rods (a) and perforated discs (b) as DC electrodes provide the radial and axial confinement for the (molecular) ions. Mg or Ba atomic ovens (c) steam atoms into the guide where they get photo ionized to provide Coulomb crystals in chamber C3 (or C1). We will try to guide the cold fraction of a beam of neutral molecules out of a reservoir (h) via differential pumping stages (e) through chambers C1 and C2 into the experimental chamber C3 to interact with stored ions. On the other hand we could either ionize the neutral molecules via electron bombardment (d) or use the ESI-source (i) to inject molecular ions of interest into the guide. The molecular ions will be guided into chamber C3 sympathetically cooled (detected (f)), transferred in the not jet installed segmented trap (g) to get separated from the ion crystal and positioned for further pump and probe experiments.

of the new setup, laser cool and detect their crystalline order. Sympathetically cooling "simple" molecular ions and transferring them along the guide will be the necessary requisite to combine the system, starting in 2009, with the ESI-source to provide the molecular ions and to append the segmented linear trap at the end of the guide.
Ultimately, we want to realize diffraction pump-and-probe-experiments, e.g. photo triggered isomerization recorded by X-ray pulses provided by the MAP-collaboration, on single molecular ions to elucidate the structural changes during chemical reactions. We will collaborate, on single molecular ions to elucidate the structural changes during chemical reactions. We will try to handle undisturbed single molecular ions ($m < 10^4$ u) by sympathetically laser cooling the external degrees of freedom in a Coulomb crystal confined in a Paul trap, cooling the internal rot-vibrational degrees of freedom by buffer gas cooling close to their ground states, separate single molecular ions into a diffraction zone by controlling electrical fields on electrodes and light pressure and 3D-orient them in space by additional light pulses.

REFERENCES

[1] R.P Feynman *Int. J. Theo. Phys.*, **21** (1982).
[2] S. Lloyd, *Science* **273**, 1073 (1996).
[3] D. Porras and J.I. Cirac, *Phys. Rev. Lett.* **92**, 207901 (2004).
[4] T. Schaetz, A. Friedenauer, H. Schmitz, L. Petersen, and S. Kahra, *J. Mod. Opt.* **54**, 2317 (2007).
[5] A. Friedenauer, F. Markert, H. Schmitz, S. Kahra, M. Herrmann, Th. Udem, T. W. Haensch, and T. Schaetz, *App. Phys. B* **84**, 371 (2006).
[6] D. Leibfried, B. DeMarco, V. Meyer, D. Lucas, M. Barrett, J. Britton, W. Itano, B. Jelenkovic, C. Langer, and T. Rosenband, *Nature* **422**, 412 (2003).
[7] A. Friedenauer, H. Schmitz, J. Glueckert, D. Porras and T. Schaetz, *Nature Phys.,* (accepted 29.05.2008) arXiv:0802.4072v1.
[8] D. Porras and J.I. Cirac, *Phys. Rev. Lett.* **93**, 263602 (2004).
[9] B. C. Travaglione and G. J. Milburn, *Phys. Rev. A* **65**, 032310 (2002).
[10] P. M. Alsing, J. P. Dowling and G. J. Milburn, *Phys. Rev. Lett.* **94**, 220401 (2005).
[11] R. Schuetzhold, M. Uhlmann, L. Petersen, A. Friedenauer, H. Schmitz, and T. Schaetz, *Phys. Rev. Lett.* **99**, 201301 (2007).
[12] Lamata, J. Leon, T. Schaetz, and E. Solano, *Phys. Rev. Lett.* **98**, 253005 (2007).
[13] http://www.map.uni-muenchen.de/map.en.html

1.1.2 SURVEY OF THE RESEARCH ACTIVITIES

Bose-Einstein Condensation

Project	Objective	Team
Mott-like state of molecules	Preparation of a quantum state with exactly one molecule at each site of an optical lattice.	D.M. Bauer S. Dürr E. Hansis N. Syassen T. Volz
Atom-molecule oscillations	Observation of large-amplitude oscillations between an atomic and a molecular state in an optical lattice.	D.M. Bauer D. Dietze S. Dürr M. Lettner N. Syassen T. Volz
Dissipative Tonks gas of molecules	Driving a system into a strongly-correlated state using inelastic interactions.	D.M. Bauer D. Dietze S. Dürr M. Lettner N. Syassen T. Volz

Cavity Quantum Electrodynamics

Project	Objective	Team
Blue trap	Development of an improved intracavity dipole trap with blue-detuned light fields.	A. Kubanek K. Murr P.W.H. Pinkse T. Puppe I. Schuster
Non-linear cavity QED	Theory, simulation and experiments on the quantum nonlinear regime of cavity QED.	A. Fuhrmanek A. Kubanek K. Murr A. Ourjoumtsev P.W.H. Pinkse T. Puppe I. Schuster
Apparatus II	Development of a next generation strong-coupling cavity QED apparatus.	B. Hagemann M. Koch A. Kubanek K. Murr A. Ourjoumtsev P.W.H. Pinkse C. Sames I. Schuster

Cavity Quantum Electrodynamics (continued)

Project	Objective	Team
Higher-order cavity modes	Theory and experiments on higher-order cavity modes beyond the paraxial approximation.	B. Hagemann M. Koch M. Motsch P.W.H. Pinkse M. Zeppenfeld

Quantum Information Processing

Project	Objective	Team
Single-photon server	Emission of a bit stream of single photons from one-and-only-one intracavity atom.	M. Hijlkema H. Specht B. Weber S.C. Webster
Single-photon characterisation	Characterisation and optimization of single-photon pulses using two-photon interference phenomena.	H. Specht S.C. Webster T. Wilk
Atom-photon quantum interface	Deterministic atom-photon and photon-photon entanglement generation.	S.C. Webster T. Wilk
Scalability	Investigation of scalable quantum information processing with cavity QED systems.	J. Bochmann C. Erbel G. Langfahl-Klabes D.L. Moehring M. Mücke H. Specht B. Weber
Single-atom imaging	Spatially resolved observation of an array of single atoms trapped in a high-finesse cavity.	M. Hijlkema D.L. Moehring T. Müller H. Specht B. Weber

Cold Polar Molecules

Project	Objective	Team
Electrodynamic trapping	Investigation of electrodynamic trapping of atoms.	P.W.H. Pinkse T. Rieger
Cryogenic source	Development of a cryogenic source of molecules with buffer-gas cooling and guided extraction.	L.D. van Buuren M. Motsch P.W.H. Pinkse S. Pohle C. Sommer
Ultraviolet laser spectroscopy	Spectroscopic study of molecules at room temperature and of guided slow molecules.	L.D. van Buuren M. Motsch P.W.H. Pinkse M. Schenk M. Zeppenfeld
Visible Rayleigh scattering	Investigation of the cavity enhancement of light scattering from molecules in the Rayleigh regime.	M. Motsch P.W.H. Pinkse M. Zeppenfeld
Infrared laser spectroscopy	Development of new traps for spectroscopy and cooling of molecules.	P.W.H. Pinkse M. Zeppenfeld

JUNIOR RESEARCH GROUP

Quantum Simulations with Trapped Ions

Project	Objective	Team
Quantum Simulations with trapped atomic ions	Demonstration of feasibility for simulating a "quantum phase transition" in a segmented linear Paul-trap using atomic ions as qubits.	A. Friedenauer J. Glückert R. Matjeschk L. Petersen T. Schätz H. Schmitz C. Schneider
Dynamical trapping of neutral molecules and ions	Experiment to test the possibility of guiding and trapping neutral polar molecules and atomic (laser cooled) ions in the same apparatus to investigate their mutual interaction.	S. Kahra G. Leschhorn (P.W.H. Pinkse) T. Schätz
Single molecule imaging	Loading, trapping and sympathetic laser cooling of (internally cold) orientated molecular ions to study fast dynamical changes triggered by femto-second laser pulses via electron/X-ray scattering.	S. Kahra, G. Leschhorn (E. Fill) (W. Fuß) (W. Schmid) T. Schätz

1.1.3 SELECTED REPRINTS

1) Preparation of a quantum state with one molecule at each site of an optical lattice.
T. Volz, N. Syassen, D.M. Bauer, S. Dürr, and G. Rempe
Nature Physics **2**, *692-695 (2006).*
MPQ Progress Report: page 24

2) Polarization-Controlled Single Photons.
T. Wilk, S.C. Webster, H.P. Specht, G. Rempe, and A. Kuhn
Physical Review Letters **98**, *063601 (2007).*
MPQ Progress Report: page 28

3) A single-photon server with just one atom.
M. Hijlkema, B. Weber, H.P. Specht, S.C. Webster, A. Kuhn, and G. Rempe
Nature Physics **3**, *253-255 (2007).*
MPQ Progress Report: page 32

4) Trapping and Observing Single Atoms in a Blue-Detuned Intracavity Dipole Trap.
T. Puppe, I. Schuster, A. Grothe, A. Kubanek, K. Murr, P.W.H. Pinkse, and G. Rempe
Physical Review Letters **99**, *013002 (2007).*
MPQ Progress Report: page 35

5) Atom-molecule Rabi Oscillations in a Mott Insulator.
N. Syassen, D.M. Bauer, M. Lettner, D. Dietze, T. Volz, S. Dürr, and G. Rempe
Physical Review Letters **99**, *033201 (2007).*
MPQ Progress Report: page 39

6) Single-Atom Single-Photon Quantum Interface.
T. Wilk, S.C. Webster, A. Kuhn, and G. Rempe
Science **317**, *488-490 (2007).*
MPQ Progress Report: page 43

7) Trapping of Neutral Rubidium with a Macroscopic Three-Phase Electric Trap.
T. Rieger, P. Windpassinger, S.A. Rangwala, G. Rempe, and P.W.H. Pinkse
Physical Review Letters **99**, *063001 (2007).*
MPQ Progress Report: page 46

8) Cavity Cooling of Internal Molecular Motion.
G. Morigi, P.W.H. Pinkse, M. Kowalewski, and R. de Vivie-Riedle
Physical Review Letters **99**, *073001 (2007)*.
MPQ Progress Report: page 50

9) Nonlinear spectroscopy of photons bound to one atom.
I. Schuster, A. Kubanek, A. Fuhrmanek, T. Puppe, P.W.H. Pinkse, K. Murr, and G. Rempe
Nature Physics **4**, *382-385 (2008).*
MPQ Progress Report: page 54

10) Strong Dissipation Inhibits Losses and Induces Correlations in Cold Molecular Gases.
N. Syassen, D.M. Bauer, M. Lettner, T. Volz, D. Dietze, J.J. García-Ripoll, J.I. Cirac, G. Rempe, and S. Dürr
Science **320**, *1329-1331 (2008).*
MPQ Progress Report: page 58

JUNIOR RESEARCH GROUP

Dr. T. Schätz

1) Analogue of Cosmological Particle Creation in an Ion Trap
Ralf Schützhold and Michael Uhlmann, Lutz Petersen, Hector Schmitz, Axel Friedenauer, and Tobias Schätz
Physical Review Letters **99**, *201301 (2007).*
MPQ Progress Report: page 61

2) Simulating the Quantum Magnet with Trapped Ions
Axel Friedenauer, Hector Schmitz, Jan Glückert, Diego Porras, and Tobias Schätz
Dated: 02.06.2008, accepted for publication in Nature Physics, arXiv:quant-ph/0802.4072v1.
MPQ Progress Report: page 65

LETTERS

Preparation of a quantum state with one molecule at each site of an optical lattice

T. VOLZ, N. SYASSEN, D. M. BAUER, E. HANSIS, S. DÜRR* AND G. REMPE*
Max-Planck-Institut für Quantenoptik, Hans-Kopfermann-Straße 1, 85748 Garching, Germany
*e-mail: stephan.duerr@mpq.mpg.de; gerhard.rempe@mpq.mpg.de

Published online: 24 September 2006; doi:10.1038/nphys415

Ultracold gases in optical lattices are of great interest, because these systems bear great potential for applications in quantum simulations and quantum information processing, in particular when using particles with a long-range dipole–dipole interaction, such as polar molecules[1–5]. Here we show the preparation of a quantum state with exactly one molecule at each site of an optical lattice. The molecules are produced from an atomic Mott insulator[6] with a density profile chosen such that the central region of the gas contains two atoms per lattice site. A Feshbach resonance is used to associate the atom pairs to molecules[7–14]. The remaining atoms can be removed with blast light[13,15]. The technique does not rely on the molecule–molecule interaction properties and is therefore applicable to many systems.

A variety of interesting proposals for quantum information processing and quantum simulations[1–5] require as a prerequisite a quantum state of ultracold polar molecules in an optical lattice, where each lattice site is occupied by exactly one molecule. A promising strategy for the creation of such molecules is based on the association of ultracold atoms using a Feshbach resonance, or photoassociation and subsequent transfer to a much lower rovibrational level using Raman transitions[16]. If the molecule–molecule interactions are predominantly elastic and effectively repulsive, then a state with one molecule per lattice site can finally be obtained using a quantum phase transition from a superfluid to a Mott insulator by ramping up the depth of an optical lattice[6]. However, many molecular species do not have such convenient interaction properties, so alternative strategies are needed. Here, we demonstrate a technique that is independent of the molecule–molecule interaction properties. The technique relies on first forming an atomic Mott insulator and then associating molecules. Several previous experiments[15,17–20] associated molecules in an optical lattice, but none of them demonstrated the production of a quantum state with exactly one molecule per lattice site. Another interesting perspective of the state prepared here is that after Raman transitions to the rovibrational ground state, the lattice potential can be lowered to obtain a Bose–Einstein condensate (BEC) of molecules in the rovibrational ground state[21,22].

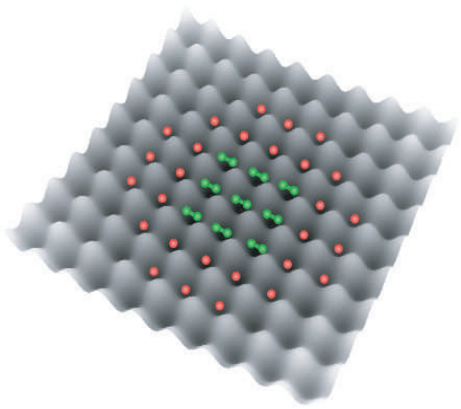

Figure 1 Schematic diagram of the molecular $n = 1$ state. In the core of the cloud, each lattice site is occupied by exactly $n = 1$ molecule (shown in green). In the surrounding shell, each site is occupied by exactly one atom (shown in red). The atoms can be removed with a blast laser. In the experiment, the number of occupied lattice sites is much larger than shown here.

The behaviour of bosons in an optical lattice is described by the Bose–Hubbard hamiltonian[23]. The relevant parameters are the amplitude J for tunnelling between neighbouring lattice sites and the on-site interaction matrix element U. We create a Mott insulator[6] of atomic ^{87}Rb starting from an atomic BEC in an optical dipole trap by slowly ramping up the depth of the optical lattice (see the Methods section). The typical lattice depth[6] seen by an atom is $V_0 = 24E_r$, where $E_r = \hbar^2k^2/(2m)$ is the recoil energy, where m is the mass of one atom, $\hbar$ is the reduced Planck constant and $2\pi/k = 830$ nm is the wavelength of the lattice light. At this lattice depth, the atomic tunnelling amplitude is $J = 2\pi\hbar \times 4$ Hz.

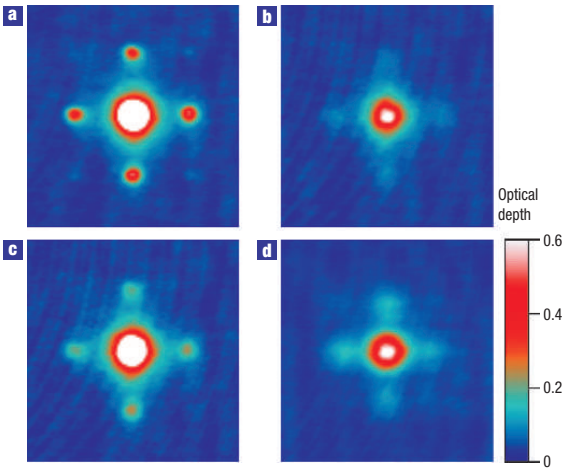

Figure 2 Atomic Mott insulator and molecular $n = 1$ state. a, An atomic Mott insulator is melted by reducing the lattice depth slowly. The system returns to the superfluid phase and phase coherence is restored. This phase coherence is probed by quickly switching off the lattice and observing an atomic interference pattern in time-of-flight. **b**, After association of molecules, only lattice sites occupied by $n = 1$ atoms contribute to the signal. **c**, After association and dissociation of molecules, the satellite peaks are much stronger than in **b**, thus proving that the molecular part of the cloud was in a molecular $n = 1$ state. **d**, Pure molecular $n = 1$ state. Same as **c** but between association and dissociation, the remaining atoms were removed with blast light. The visibilities in **a**–**d** are 0.93(2), 0.80(5), 0.86(1) and 0.61(2), calculated from squares with areas corresponding to atomic momenta of $0.22\hbar k \times 0.22\hbar k$ (see the inset in Fig. 3 and ref. 25).

Owing to the external harmonic confinement (see the Methods section), the atomic Mott insulator is inhomogeneous. It consists of shells of constant lattice filling with exactly n particles per lattice site. Neighbouring shells are connected by narrow superfluid regions. For a deep lattice, J becomes small. With the approximation $J = 0$, the ground state of the system including the harmonic confinement can be calculated analytically. This model predicts that the fraction of atoms occupying sites with $n = 2$ atoms has a maximum of 53%. This value should be reached, when operating close to the point where a core with $n = 3$ atoms per site starts to form. To operate at this point, we load the lattice with $N = 10^5$ atoms. For larger numbers of atoms, an $n = 3$ core forms, which is seen in the experiment as loss when associating molecules (see below).

After preparing the atomic Mott insulator at a magnetic field of $B = 1{,}008.8$ G, molecules are associated as described in ref. 9. To this end, the magnetic field is slowly (at $2\,\mathrm{G\,ms^{-1}}$) ramped across the Feshbach resonance at 1,007.4 G (ref. 24) to a final value of $B = 1{,}006.6$ G. At lattice sites with a filling of $n = 1$, this has no effect. At sites with $n > 1$, atom pairs are associated to molecules. If the site contained $n > 2$ atoms, then the molecule can collide with other atoms or molecules at the same lattice site. As the molecules are associated in a highly excited rovibrational state, the collisions are likely to be inelastic. This leads to fast loss of the molecule and its collision partner from the trap. The association ramp lasts long enough to essentially empty all sites with $n > 2$ atoms. For lattice sites with $n = 2$ atoms, the association efficiency is above 80%, similar to ref. 15. The resulting molecular $n = 1$ state is sketched in Fig. 1. The maximum fraction of the population that can be converted into molecules (measured as the atom number reappearing after dissociation) is found to be 47(3)% (that is, 47 ± 3%), which is close to the theoretical limit of 53% discussed above.

At a lattice depth of $V_0 = 24E_r$ for atoms, the tunnelling amplitude for molecules is calculated to be $J_m = 2\pi\hbar \times 0.3$ mHz. This is negligible compared with the hold time between association and dissociation, so that the positions of the molecules are frozen. This conclusion is further supported by the experimental observation of a long lifetime of the molecules (see below).

To show that the molecular part of the sample really is in the $n = 1$ state, the molecules are first dissociated back into atom pairs by slowly (at $1.5\,\mathrm{G\,ms^{-1}}$) ramping the magnetic field back across the Feshbach resonance. This brings the system back into the atomic Mott insulator state with shells with $n = 1$ and $n = 2$. Then, the atomic Mott insulator is melted by slowly (within 10 ms) ramping down the lattice from $V_0 = 24E_r$ to $V_0 = 4E_r$. Finally, the lattice is quickly switched off and after some time-of-flight an absorption image is taken.

Such images are shown in Fig. 2. Figure 2a shows the result if the magnetic-field ramp for association and dissociation of molecules is omitted. This matter–wave interference pattern shows that phase coherence is restored when ramping down the lattice, thus demonstrating that an atomic Mott insulator is realized at 1,008.8 G. Figure 2b shows the pattern obtained if molecules are associated but not dissociated, so that they remain invisible in the detection. This signal comes only from sites with $n = 1$ atoms. Figure 2c shows the result obtained for the full sequence with association and dissociation of molecules. Obviously, the satellite peaks regain considerable population compared with Fig. 2b, which proves that after dissociation, we recover an atomic Mott insulator. This shows that association and dissociation must have been coherent and adiabatic. Combined with the freezing of the positions of the molecules and the fact that the association starts from an atomic Mott insulator with an $n = 2$ core, this implies that the molecular part of the cloud must have been in a quantum state with one molecule per lattice site.

After associating the molecules, the remaining atoms can be removed from the trap using microwave radiation and a blast laser as in ref. 15. This produces a pure molecular sample. The molecule numbers before and after the blast are identical within an experimental uncertainty of 5%. To show that the pure molecular sample is in the $n = 1$ state, the molecules are dissociated, the lattice is ramped down to $V_0 = 1.2E_r$ within 30 ms, ramped back up (see the Methods section) to $V_0 = 6E_r$ within 5 ms, and finally switched off. The result is shown in Fig. 2d. Again, an interference pattern is visible. The time-of-flight was 12 ms in Fig. 2a–c and 11 ms in Fig. 2d.

The height of the satellite peaks can be quantified using the visibility defined in ref. 25. Figure 3 shows the decay of the visibility as a function of the hold time between molecule association and dissociation. These data were obtained from measurements as in Fig. 2d except that after dissociation the lattice was ramped down to $V_0 = 2.8E_r$ within 10 ms and ramped back up to $V_0 = 5.5E_r$ within 4 ms. The observed lifetime of the visibility is sufficient for many applications. For comparison, the measured lifetime of the molecule number is 160(20) ms, which is probably due to scattering of lattice photons[15]. This molecule loss sets an upper limit on the lifetime of the visibility, because the sites at which molecules are lost are randomly distributed across the lattice, thus gradually destroying the molecular $n = 1$ state. According to the fit, the visibility settles to an offset value of 15%. This might be partly due to the fact that the Wannier function[25] for small lattice depth is not spherically symmetric and partly due to a small contribution of non-removed atoms because of imperfections of the blast laser (15% of the total signal at zero hold time).

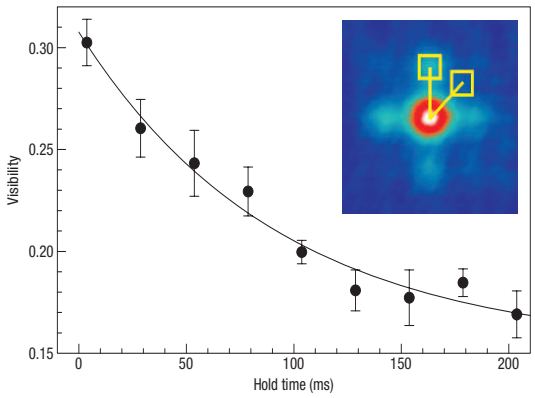

Figure 3 Lifetime of the molecular $n = 1$ state after removing the atoms. The visibility of the satellite peaks in measurements similar to Fig. 2d decays as a function of the hold time between molecule association and dissociation. The visibility was calculated from squares (as shown in the inset) with areas corresponding to atomic momenta of $1.0\hbar k \times 1.0\hbar k$. The line shows an exponential fit that yields a $1/e$-lifetime of 93(22) ms. The error bars are statistical (one standard deviation).

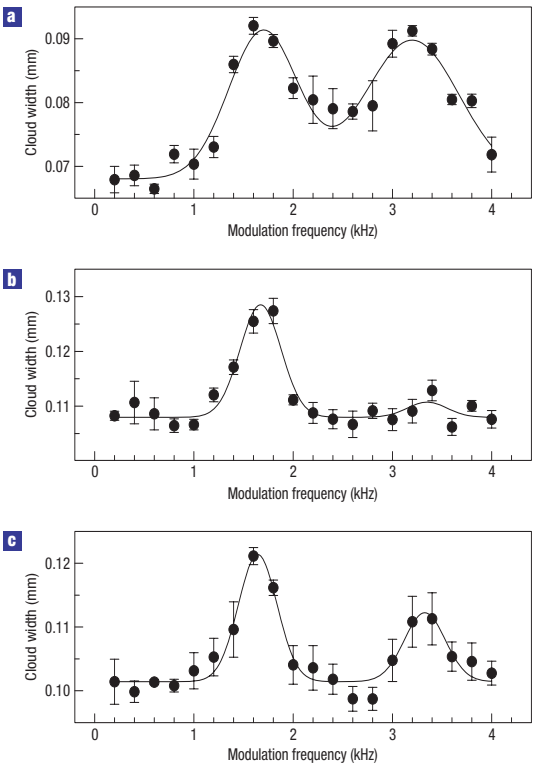

Figure 4 Excitation spectrum of the atomic Mott insulator. The full-width at half-maximum of the central interference peak is shown as a function of the frequency at which the lattice depth is modulated. **a–c**, The results correspond to the conditions of Fig. 2a–c. First, the usual lattice ramp-down starting at $V_0 = 24E_r$ is interrupted at $V_0 = 15E_r$. Next, the power of one lattice beam is modulated for 11 ms with a peak-to-peak amplitude of 50%. Finally, the lattice ramp-down continues as usual. Resonances are visible at 1.6 and 3.2 kHz. The lines are a guide to the eye. The error bars are statistical (one standard deviation).

Figure 4 shows the excitation spectrum of the atomic Mott insulator at $V_0 = 15E_r$ ($J = 2\pi\hbar \times 21$ Hz, $J_m = 2\pi\hbar \times 14$ mHz) as measured by amplitude modulation of one lattice beam[26]. The spectrum in Fig. 4a shows clear resonances at energies U and $2U$. Below the first resonance, no noticeable excitations are created, showing that the excitation spectrum has a gap. This again shows that the system before molecule association is an atomic Mott insulator. In Fig. 4b, the signal at $2U$ essentially disappeared, because the signal at $2U$ is created by processes that require lattice sites with $n \geq 2$ atoms[6], which are absent without the modulation. The spectrum in Fig. 4c is similar to that in Fig. 4a. Resonances at U and $2U$ are clearly visible in Fig. 4c. This gives further experimental support for the above conclusion that the system after the association–dissociation ramp is still an atomic Mott insulator.

We also measured the excitation spectrum at various lattice depths for the molecular $n = 1$ state after removing the atoms, corresponding to Fig. 2d. This spectrum does not show any resonances related to U. We only observe resonances at much higher frequencies due to band excitation. The absence of resonances related to U is probably due to the short lifetime of two molecules at one lattice site (see the Methods section), which leads to an estimated resonance width of $\Gamma = 2\pi\hbar \times 10$ kHz. This is too broad and consequently too shallow to be observed. Furthermore, the real part of the molecule–molecule scattering length is unknown. Hence, it is also unknown whether the molecular $n = 1$ state created here has a gap, and if so, at what energy the first resonance should be expected.

In the experiment $\Gamma \gg J_m$, so that the effective tunnelling rate between neighbouring lattice sites is $4J_m^2/(\hbar\Gamma)$ (ref. 27). Interestingly, fast on-site decay Γ suppresses the mobility in the many-body system. This might lead to an insulator-like behaviour without a gap.

In conclusion, we prepared a quantum state with exactly one molecule at each site of an optical lattice. It is an interesting question, whether gapless systems can have insulating properties due to fast on-site losses. The quantum state prepared here is exactly the state that a molecular Mott insulator has in the limit of negligible tunnelling. Unlike the creation of a molecular Mott state by a quantum phase transition from a molecular BEC, our method works independently of the molecule–molecule interaction properties.

METHODS

DIPOLE TRAP SETUP

The experiment begins with the creation of a BEC of ^{87}Rb atoms in a magnetic trap[24]. Once created, the BEC is transferred into an optical dipole trap that is created by crossing two light beams at right angles. One beam has a wavelength of 1,064 nm, a power of 170 mW and a waist ($1/e^2$ radius of intensity) of 140 μm. The other beam has a wavelength of 1,050 nm, a power of 2.1 W and an elliptically shaped focus with waists of 60 and 700 μm. The crossed-beam dipole trap creates an approximately harmonic confinement with measured trap frequencies of 20, 20 and 110 Hz. The strongest confinement supports the atoms against gravity. After loading the dipole trap, a magnetic field of approximately 1,000 G is applied. The atoms are transferred[28] to the absolute ground state $|F = 1, m_F = 1\rangle$ where F and m_F are the hyperfine quantum numbers, which has a Feshbach resonance at 1,007.4 G with a width of 0.2 G (refs 28,29). The dipole-trap light at 1,050 nm comes from a multifrequency

fibre laser with a linewidth of ~1 nm. The experiment shows that this causes fast loss of the molecules, presumably due to photodissociation. Therefore, the power of the dipole-trap light is slowly reduced to zero just before associating the molecules and slowly ramped back up to its original value just after dissociating them. Finally, the dipole trap and the optical lattice are switched off simultaneously.

LATTICE SETUP

A simple-cubic optical lattice is created by illuminating the BEC with three retro-reflected light beams with a waist of 140 μm. The finite waists of the lattice beams give rise to an additional overall confinement. For $V_0 = 15E_r$, this corresponds to an estimated trap frequency of 50 Hz. This harmonic potential adds to the potential of the dipole trap. Note that the polarizability of a Feshbach molecule is approximately twice as large as that for one atom. Hence, the molecules experience a lattice depth of $2V_0$.

RAMPING FOR CONDITIONS USED IN FIG. 2D

To understand why a special ramping procedure is needed for Fig. 2d, consider the atomic Mott insulator obtained after dissociating the molecules. This Mott insulator has only the $n = 2$ core, whereas the surrounding $n = 1$ shell is missing. Now consider two atoms at an $n = 2$ site. If one of the atoms tunnelled to an empty neighbouring lattice site, then this would release an energy U. But there is no reservoir that could absorb this energy so that the tunnelling is suppressed[19]. Hence, a strong reduction of U is required to melt the pure $n = 2$ Mott insulator. This can be achieved by ramping the lattice down to a point much below $V_0 = 4E_r$ (or by reducing the scattering length). At this low lattice depth, the sudden switch-off of the lattice does not produce noticeable satellite peaks. To observe such peaks, the lattice therefore must be ramped back up before switching it off.

INELASTIC COLLISIONS

If only lattice sites that are occupied by exactly two molecules are considered, and if tunnelling is negligible, then the sites will decay independently of each other. Hence, the total population of these sites will decay exponentially. We measured the rate coefficient for inelastic molecule–molecule collisions. At $V_0 = 15\,E_r$, this leads to an estimated lifetime of 16 μs.

Received 16 June 2006; accepted 24 August 2006; published 24 September 2006.

References

1. DeMille, D. Quantum computation with trapped polar molecules. *Phys. Rev. Lett.* **88,** 067901 (2002).
2. Góral, K., Santos, L. & Lewenstein, M. Quantum phases of dipolar bosons in optical lattices. *Phys. Rev. Lett.* **88,** 170406 (2002).
3. Lee, C. & Ostrovskaya, E. A. Quantum computation with diatomic bits in optical lattices. *Phys. Rev. A* **72,** 062321 (2005).
4. Micheli, A., Brennen, G. K. & Zoller, P. A toolbox for lattice-spin models with polar molecules. *Nature Phys.* **2,** 341–347 (2006).
5. Barnett, R., Petrov, D., Lukin, M. & Demler, E. Quantum magnetism with multicomponent dipolar molecules in an optical lattice. *Phys. Rev. Lett.* **96,** 190401 (2006).
6. Greiner, M., Mandel, O., Esslinger, T., Hänsch, T. W. & Bloch, I. Quantum phase transition from a superfluid to a Mott insulator in a gas of ultracold atoms. *Nature* **415,** 39–44 (2002).
7. Regal, C. A., Ticknor, C., Bohn, J. L. & Jin, D. S. Creation of ultracold molecules from a Fermi gas of atoms. *Nature* **424,** 47–50 (2003).
8. Herbig, J. *et al*. Preparation of a pure molecular quantum gas. *Science* **301,** 1510–1513 (2003).
9. Dürr, S., Volz, T., Marte, A. & Rempe, G. Observation of molecules produced from a Bose-Einstein condensate. *Phys. Rev. Lett.* **92,** 020406 (2004).
10. Strecker, K. E., Partridge, G. B. & Hulet, R. G. Conversion of an atomic Fermi gas to a long-lived molecular Bose gas. *Phys. Rev. Lett.* **91,** 080406 (2003).
11. Cubizolles, J., Bourdel, T., Kokkelmans, S. J., Shlyapnikov, G. V. & Salomon, C. Production of long-lived ultracold Li_2 molecules from a Fermi gas. *Phys. Rev. Lett.* **91,** 240401 (2003).
12. Jochim, S. *et al*. Pure gas of optically trapped molecules created from fermionic atoms. *Phys. Rev. Lett.* **91,** 240402 (2003).
13. Xu, K. *et al*. Formation of quantum-degenerate sodium molecules. *Phys. Rev. Lett.* **91,** 210402 (2003).
14. Köhler, T., Góral, K. & Julienne, P. S. Production of cold molecules via magnetically tunable Feshbach resonances. Preprint at <http://arxiv.org/abs/cond-mat/0601420> (2006).
15. Thalhammer, G. *et al*. Long-lived Feshbach molecules in a three-dimensional optical lattice. *Phys. Rev. Lett.* **96,** 050402 (2006).
16. Sage, J. M., Sainis, S., Bergeman, T. & DeMille, D. Optical production of ultracold polar molecules. *Phys. Rev. Lett.* **94,** 203001 (2005).
17. Rom, T. *et al*. State selective production of molecules in optical lattices. *Phys. Rev. Lett.* **93,** 073002 (2004).
18. Stöferle, T., Moritz, H., Günter, K., Köhl, M. & Esslinger, T. Molecules of fermionic atoms in an optical lattice. *Phys. Rev. Lett.* **96,** 030401 (2006).
19. Winkler, K. *et al*. Repulsively bound atom pairs in an optical lattice. *Nature* **441,** 853–856 (2006).
20. Ryu, C. *et al*. Raman-induced oscillation between an atomic and a molecular quantum gas. Preprint at <http://arxiv.org/abs/cond-mat/0508201> (2005).
21. Jaksch, D., Venturi, V., Cirac, J. I., Williams, C. J. & Zoller, P. Creation of a molecular condensate by dynamically melting a Mott insulator. *Phys. Rev. Lett.* **89,** 040402 (2002).
22. Damski, B. *et al*. Creation of a dipolar superfluid in optical lattices. *Phys. Rev. Lett.* **90,** 110401 (2003).
23. Jaksch, D., Bruder, C., Cirac, J. I., Gardiner, C. W. & Zoller, P. Cold bosonic atoms in optical lattices. *Phys. Rev. Lett.* **81,** 3108–3111 (1998).
24. Marte, A. *et al*. Feshbach resonances in rubidium 87: Precision measurement and analysis. *Phys. Rev. Lett.* **89,** 283202 (2002).
25. Gerbier, F. *et al*. Phase coherence of an atomic Mott insulator. *Phys. Rev. Lett.* **95,** 050404 (2005).
26. Stöferle, T., Moritz, H., Schori, C., Köhl, M. & Esslinger, T. Transition from a strongly interacting 1D superfluid to a Mott insulator. *Phys. Rev. Lett.* **92,** 130403 (2004).
27. Cohen-Tannoudji, C., Dupont-Roc, J. & Grynberg, G. *Atom-Photon Interactions* 49–59 (Wiley, New York, 1992).
28. Volz, T., Dürr, S., Ernst, S., Marte, A. & Rempe, G. Characterization of elastic scattering near a Feshbach resonance in ^{87}Rb. *Phys. Rev. A* **68,** 010702(R) (2003).
29. Dürr, S., Volz, T. & Rempe, G. Dissociation of ultracold molecules with Feshbach resonances. *Phys. Rev. A* **70,** 031601(R) (2004).

Acknowledgements

We thank J. I. Cirac, T. Esslinger and W. Zwerger for fruitful discussions.
Correspondence and requests for materials should be addressed to S.D. or G.R.

Competing financial interests

The authors declare that they have no competing financial interests.

PRL 98, 063601 (2007) PHYSICAL REVIEW LETTERS week ending 9 FEBRUARY 2007

Polarization-Controlled Single Photons

T. Wilk,[1] S. C. Webster,[1] H. P. Specht,[1] G. Rempe,[1] and A. Kuhn[2]

[1]*Max-Planck-Institut für Quantenoptik, Hans-Kopfermann-Straße 1, 85748 Garching, Germany*

[2]*Department of Physics, Clarendon Laboratory, University of Oxford, Parks Road, Oxford, OX1 3PU, United Kingdom*

(Received 25 October 2006; published 5 February 2007)

Vacuum-stimulated Raman transitions are driven between two magnetic substates of a ^{87}Rb atom strongly coupled to an optical cavity. A magnetic field lifts the degeneracy of these states, and the atom is alternately exposed to laser pulses of two different frequencies. This produces a stream of single photons with alternating circular polarization in a predetermined spatiotemporal mode. MHz repetition rates are possible as no recycling of the atom between photon generations is required. Photon indistinguishability is tested by time-resolved two-photon interference.

DOI: 10.1103/PhysRevLett.98.063601 PACS numbers: 42.50.Dv, 03.67.Hk, 42.50.Pq, 42.65.Dr

A major issue in quantum information processing (QIP) is to boost the scale of current experimental implementations so that many quantum bits (qubits) can be handled. One way to get there is to establish a network of stationary quantum systems and to interconnect them by flying qubits such as single photons. In principle, this can be achieved with single atoms coupled to single photons in optical cavities. Most proposals [1–4] require these photons to be indistinguishable, that is in the same spatiotemporal mode of known frequency and polarization. Previous atom-cavity photon sources [5–7] have met these requirements except for the polarization control, whereas the latter has only been achieved with probabilistic single-photon emitters [8–10]. Here we describe the realization of a deterministic single-photon source based on an atom-cavity system which produces photons of known polarization. A Raman transition between the $m_F = \pm 1$ Zeeman sublevels of the $5S_{1/2}$, $F = 1$ ground state of a ^{87}Rb atom is driven by the combination of a pump laser and the cavity vacuum field stimulating the emission of a single photon [11]. Such a scheme could also be used to generate a stream of single-photon time-bin qubits in an entangled state. By combining partial photon production with internal rotations of the atom, photon states such as the GHZ and W states could be constructed [12].

Figures 1(a) and 1(b) show the relevant levels involved in our scheme, the $5S_{1/2}$, $F = 1$ ground states, labeled by magnetic sublevel $|-1\rangle$, $|0\rangle$, and $|+1\rangle$, and the $5P_{3/2}$, $F' = 1$, $m_F = 0$ excited state, $|e\rangle$. A magnetic field along the cavity axis defines the quantization axis and lifts the degeneracy of the ground states, producing an energy shift of the $m_F = \pm 1$ states of $\mp\hbar\Delta_B$. For geometrical reasons the cavity supports only σ^+ and σ^- photons along its axis. The cavity resonance frequency ω_c is chosen to be ω_{0e}, the frequency of the $|0\rangle \leftrightarrow |e\rangle$ transition, and is fixed during the experiment. The pump laser is linearly polarized perpendicular to the quantization axis, decomposing into σ^+ and σ^- components, and has a frequency ω_p.

Consider an atom, coupled to the cavity, in the $|+1\rangle$ state. If the pump-cavity detuning $\Delta_{pc} \equiv \omega_p - \omega_c = 2\Delta_B$ then the combination of a pump pulse with the cavity vacuum field resonantly drives a Raman transition and transfers the atom to the $|-1\rangle$ state, depositing a σ^+ photon into the cavity. If the cavity field decay rate κ is similar to the Rabi frequency of the Raman transition, then the photon escapes from the cavity as the population transfer from $|+1\rangle$ to $|-1\rangle$ takes place. Once the atom is in $|-1\rangle$ and the photon has escaped, no transition to any other state is resonantly driven, ensuring that only a single photon is generated. To produce another photon with the next pump pulse, a pump-cavity detuning $\Delta_{pc} = -2\Delta_B$ is chosen to fulfil the Raman resonance for the transition from $|-1\rangle$ to $|+1\rangle$. Then laser and cavity change their roles, resulting in the production of a single σ^- photon. In contrast to previous experiments [5–7] this back and forth process requires no repumping laser pulse to return the atom to its initial state after a photon generation.

Figure 1(c) shows a schematic of the experiment. ^{87}Rb atoms are dropped from a magneto-optical trap (MOT) through the TEM_{00} mode of an optical cavity. The flux of atoms through the cavity mode is ~ 2/ms. The cavity is 1 mm long, has a finesse of 60 000, and the mode has a waist of 35 μm. One mirror has a 25 times larger transmission coefficient than the other. The relevant parameters for the system are $(g_{\max}, \kappa, \gamma)/2\pi = (3.1, 1.25, 3.0)$ MHz, where $g_{\max}$ is the atom-cavity coupling constant on the transition relevant for photon generation for an atom maximally coupled to the mode, κ is the field decay rate of the cavity, and γ the dipole decay rate for the atom (half the natural linewidth).

A magnetic field of 20 G along the cavity axis produces a Zeeman splitting of $\Delta_B/2\pi = 14$ MHz. To generate a stream of photons, a sequence of pump laser pulses with alternating frequency is continuously repeated as the atoms fall through the cavity. The Rabi frequency of the pump pulses goes as $\Omega_0 \sin^2(\pi t/t_p)$, Ω_0 being the peak Rabi

PRL 98, 063601 (2007) PHYSICAL REVIEW LETTERS week ending 9 FEBRUARY 2007

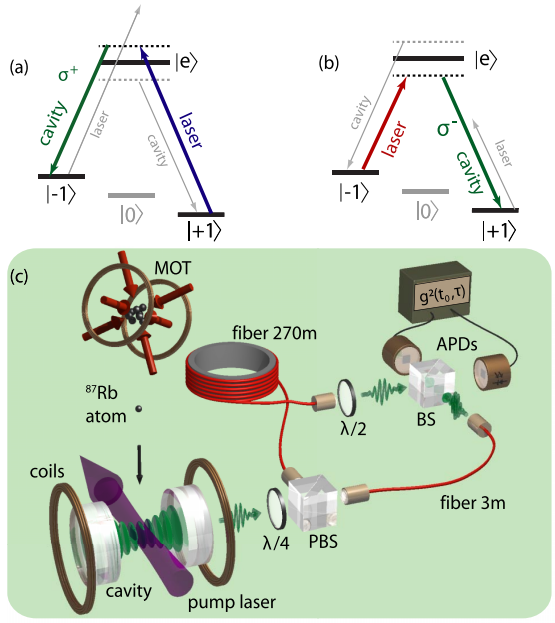

FIG. 1 (color online). Scheme and setup: (a) and (b) Relevant energy levels in ^{87}Rb for photon production. (a) The σ^- polarized component of the pump laser combines with the cavity to drive a resonant Raman transition which takes the atom from $|+1\rangle$ to $|-1\rangle$, producing a σ^+ photon. Although the σ^+ component of the pump laser (shown in gray) is present as well, this transition (which would produce an additional σ^- photon) is far off-resonant and thus unlikely. (b) A second pump pulse of different frequency returns the atom to $|+1\rangle$, while producing a σ^- photon. Again, the off-resonant return transition is unlikely. (c) As atoms fall from a MOT through the cavity we shine in the pump laser from the side to generate photons. The photons are directed through one of two fibers by a PBS, the long 270 m fiber acting as a delay line. Photons emerging from the fibers can interfere at a BS, and are detected by a pair of avalanche photodiodes (APDs).

frequency and t_p the length of the pulse. These pulses propagate perpendicular to both the motion of atoms and the cavity axis (and thus the magnetic field).

Photons produced within the cavity decay with a probability of 93% through the mirror of higher transmittance. The photons have a well-defined polarization so we can use a wave plate and polarizing beam splitter (PBS) to direct them into one of two polarization maintaining single-mode optical fibers, one long (270 m), the other short (3 m). The output modes of the fibers are recombined at a 50:50 nonpolarizing beam splitter (BS), and photons are then detected at each output port by avalanche photodiodes. This detection setup allows us to characterize our source. First, the single-photon nature is investigated when a fraction of photons is sent through only one fiber, while the other fiber is closed. In this case, we have a Hanbury Brown and Twiss setup allowing measurement of the intensity correlation as well as the detection-time distribution of the emitted photons. Second, the mutual coherence of pairs of σ^+ and σ^- photons is characterized in a time-resolved two-photon interference experiment [13,14], where both fibers are used. The long fiber is used as a delay line for a first photon and the subsequently generated second photon is sent through the short fiber so the two photons arrive at the beam splitter simultaneously, and can interfere.

We first focus on characterizing individual photons. In the measurements shown in Fig. 2 the long fiber is closed, and we only detect photons which pass through the short fiber. Figure 2(a) shows the repeating sequence of pump pulses used, with parameters $(\Omega_0/2\pi, t_p) = (24\ \text{MHz}, 1.42\ \mu\text{s})$ and detunings $\Delta_{pc} = \pm 2\Delta_B$. The pulses are labeled ω_+ and ω_- indicating that the laser frequency is such that a σ^+ or σ^- photon, respectively, should be emitted. To show that the frequency of the pump laser pulse determines the direction of the Raman process, and therefore the polarization of photons, we look at the detection-time distributions of photons of the two circular polarizations separately. In Fig. 2(b) the wave plate is oriented such that only σ^+ photons are detected, in Fig. 2(c) only σ^-. It can be clearly seen that the number of σ^+ photons generated during the ω_+ pulse is much larger (~20 times) than during the ω_- pulse. Similarly for σ^- photons, the number of detected photons during the ω_+ pulse is ~30 times smaller than during the ω_- pulse. In both cases approximately the same number of atoms pass through the cavity and similar total numbers of σ^+ and σ^- photons are detected.

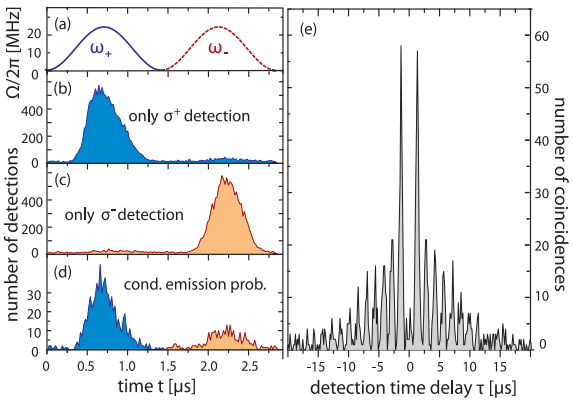

FIG. 2 (color online). Photon characteristics observed with only one path to the beam splitter open. (a) Pump pulse sequence. The first pulse, labeled ω_+, has a detuning of $\Delta_{pc}/2\pi = 28$ MHz, the second (ω_-) $\Delta_{pc}/2\pi = -28$ MHz. (b),(c) Photon detection-time distribution for σ^+/σ^- photons, showing they are overwhelmingly detected during the ω_+/ω_- pulses. (d) Detection-time distributions for photons conditioned on a detection during the previous pulse. The probability of detecting a σ^+ photon after a σ^- photon, is much larger than the probability of the opposite case. (e) Measurement of the intensity correlation between the two detectors (both polarizations are detected). The missing peak at $\tau = 0$ results from the single-photon nature of the source. Data are binned in 150 ns intervals.

PRL 98, 063601 (2007) PHYSICAL REVIEW LETTERS week ending 9 FEBRUARY 2007

A measure of the efficiency of our photon-generation process can be obtained by considering the probability for a photon emission given that a photon was detected during the previous pump pulse. This condition ensures that an atom is coupled to the cavity and that it is in the correct internal state to emit a photon in the subsequent pulse. For this measurement photons of both polarizations need to be detected, so the wave plate after the cavity is oriented such that the PBS acts as a 50:50 beam splitter for each polarization.

Shown in Fig. 2(d) are the detection-time distributions of photons detected during the ω_+ pump pulse, given that a photon was detected during the previous ω_- pulse ($t < 1.42\ \mu$s), and the arrival time distributions of photons detected during the ω_- pulse, given that a photon was detected during the previous ω_+ pulse ($t > 1.42\ \mu$s). Immediately obvious is the large difference in the number of these conditioned σ^+ and σ^- photons. Taking into account the dark count rate and the overall photon detection efficiency, we obtain two conditional probabilities for generating a photon inside the cavity: $p(\sigma^+|\sigma^-) = 41\%$ for generating a σ^+ photon after a σ^- photon, and $p(\sigma^-|\sigma^+) = 13\%$ for generating a σ^- photon after a σ^+ photon.

In addition to the large difference between these conditional probabilities for the two polarizations, it can be seen in Figs. 2(b)–2(d) that the envelopes of the single-photon wave packets depend on the polarization. The peak of the σ^+ envelope occurs earlier in the pump laser pulse than the peak of the σ^- envelope. These differences between the two polarizations occur even though the scheme shown in Figs. 1(a) and 1(b) looks symmetric; however, only the directly relevant levels are shown there. Additional levels present in the atom (principally the $F' = 0$ excited state) break this symmetry. To understand the origin of the large difference in the conditional efficiencies, we performed a simulation following the recipe of [11]. Although the simulation assumes a fixed atom rather than averaging over all possible atomic trajectories, it should be a good approximation of the experiment. The simulation gives $p(\sigma^+|\sigma^-)/p(\sigma^-|\sigma^+) \sim 0.7$ for reasonably large couplings compared with $g_{\max}$ and Ω_0, in contrast to the experimental result $p(\sigma^+|\sigma^-)/p(\sigma^-|\sigma^+) \sim 3$. The simulation can therefore not explain the observed difference.

To prove that only single photons are generated, an intensity correlation measurement is performed. As in the measurement of conditional probabilities, we send photons of both polarizations through the short fiber. After the fiber the 50:50 beam splitter randomly sends each photon to one of two avalanche photodiodes. Figure 2(e) shows the number of coincidences in the two detectors recorded as a function of the time delay τ between the detections. The comblike structure reflects the periodicity of the driving pulses, where the width of the comb is a consequence of the limited interaction time a falling atom has with the cavity mode. The feature we are most interested in is that the peak at time $\tau = 0$ is missing, meaning that we have a single-photon source. The probability of obtaining multiple photons is 2.5% that of single photons. Note that the peaks at $\tau = \pm 1.42\ \mu$s are at least 2.5 times higher than all the others since a pair of subsequent photons is more likely to be obtained than three or more photons in a row.

Many QIP applications of a single-photon source require indistinguishable photons [1–4,15]. Here, the envelopes of the σ^+ and σ^- photons are seen to be similar in Figs. 2(b) and 2(c) but this tells us nothing about the spectral properties. We test for indistinguishability by performing a time-resolved two-photon interference experiment [13,14,16]. Two photons that simultaneously enter different entrance ports of a 50:50 beam splitter will always leave through the same output port if they are indistinguishable. The degree of indistinguishability is measured by comparing the number of coincidences obtained when the pair of photons have parallel polarization with the case when they are perpendicularly polarized and thus completely distinguishable.

We superpose pairs of subsequently generated photons at a beam splitter. Both fibers are open, and since the photons have a well-defined polarization, they can be directed into either the long or the short fiber. A wave plate at the exit of the long fiber is used to set the relative polarization of the two photons. To maximize the number of events where two photons reach the beam splitter at the same time, σ^- photons are delayed while σ^+ photons, which have the higher conditional emission probability, are sent directly to the beam splitter. The time between the pump pulses is set such that there is maximum overlap of the pulse areas of the two interfering photons; this is what we denote a simultaneous arrival. As in previous experiments [14] we count the number of coincidences as a function of the detection-time difference, τ.

A typical result is shown in the inset of Fig. 3. The curves give the number of coincidences versus τ where the two photons have either parallel or perpendicular polarization at the beam splitter. The dip in the number of coincidences for parallel polarizations around $\tau = 0$ shows that the spatial mode matching of the two interfering photons is good, with the magnitude of the dip consistent with the measured single-photon interferometer visibility of 98%. This means that most of the coincidences for parallel polarization reflect the distinguishability of the photons.

We calculate the integrated two-photon interference visibility $V = 1 - (C_{\text{par}}/C_{\text{perp}})$ where $C_{\text{par}}(C_{\text{perp}})$ is the total number of coincidences for $|\tau| < t_p$ when the photons hit the beam splitter with parallel (perpendicular) polarization. It is the same information one would get in a standard Hong-Ou-Mandel (HOM) measurement [17] without detection-time resolution at the bottom of the "HOM dip". This visibility was measured for photons generated with a range of different peak Rabi frequencies Ω_0, and pulse lengths t_p, the results of which are shown in Fig. 3. The visibility increases with reduced Ω_0 and shorter pulse

PRL 98, 063601 (2007) PHYSICAL REVIEW LETTERS week ending 9 FEBRUARY 2007

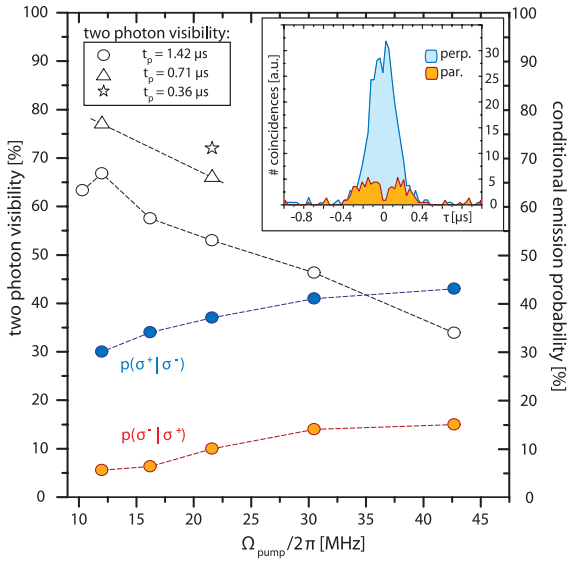

FIG. 3 (color online). Two-photon interference. Inset: coincidences as a function of the time difference between detections for photons with parallel and perpendicular polarizations. For perfect spatial mode matching, the dip around $\tau = 0$ for parallel polarizations would reach zero coincidences. The observed dip is consistent with an interferometer visibility of 98%. $(\Omega_0/2\pi, t_p) = (12\ \text{MHz}, 0.72\ \mu\text{s})$. An integrated visibility $V = 77\%$ is observed. Main figure: visibility and photon-generation efficiency as a function of pump laser peak Rabi frequency Ω_0 and various pulse durations t_p. The open symbols refer to the integrated visibility V of the two-photon interference, with different shapes for different pulse durations. V increases with lower Ω_0 and shorter t_p. The filled symbols show the conditional probabilities $p(\sigma^+|\sigma^-)$ and $p(\sigma^-|\sigma^+)$ for generating photons with a pulse duration $t_p = 1.42\ \mu\text{s}$.

durations t_p, with a maximum measured visibility of 77% for $\Omega_0/2\pi = 12$ MHz and $t_p = 0.71\ \mu$s. The visibility is influenced by both the indistinguishability of the two photons and the spatial mode matching at the beam splitter. The combination of the interferometer visibility and slightly nonidentical photon envelopes give a maximum possible visibility $V = 94\%$, which would be obtained for interfering single-photon wave packets with identical temporal evolution, higher than the maximum we obtained.

There are several processes that might affect the photon generation in a way that would make the photons more distinguishable. As discussed before, the atom is more complex than a three-level system, with additional levels in both the excited and ground states. Off-resonant transitions to these levels lead to frequency broadening with increasing Rabi frequency. In contrast to that, shorter photons show a better visibility as they have less time to dephase [16]. As expected and shown in Fig. 3, the conditional probabilities of generating a photon also change with Ω_0 and t_p. Unfortunately, conditions which lead to higher visibilities result in lower probabilities of generating photon pairs. This reduces the rate at which the source could be used in QIP applications. Of course, it is always possible to increase the visibility by postselecting only those pairs of coincidences that occur within the dip around $\tau = 0$.

In conclusion, we now have a way to generate single photons of known polarization in a well-defined spatial mode from a coupled atom-cavity system. The next step will be to use an atom trapped within a cavity [18] to produce long streams of photons, with the same coupling to the cavity for each pulse.

We thank F. Verstraete for useful discussions. This work was supported by the Deutsche Forschungsgemeinschaft (SFB 631, Research Unit 635) and the European Union [IST (QGATES, SCALA) and IHP (CONQUEST) programs].

[1] J. I. Cirac, P. Zoller, H. J. Kimble, and H. Mabuchi, Phys. Rev. Lett. **78**, 3221 (1997).
[2] C. Cabrillo, J. I. Cirac, P. García-Fernández, and P. Zoller, Phys. Rev. A **59**, 1025 (1999).
[3] D. E. Browne, M. B. Plenio, and S. F. Huelga, Phys. Rev. Lett. **91**, 067901 (2003).
[4] L.-M. Duan and H. J. Kimble, Phys. Rev. Lett. **90**, 253601 (2003).
[5] A. Kuhn, M. Hennrich, and G. Rempe, Phys. Rev. Lett. **89**, 067901 (2002).
[6] M. Keller, B. Lange, K. Hayasaka, W. Lange, and H. Walther, Nature (London) **431**, 1075 (2004).
[7] J. McKeever, A. Boca, A. D. Boozer, R. Miller, J. R. Buck, A. Kuzmich, and H. J. Kimble, Science **303**, 1992 (2004).
[8] C. K. Hong and L. Mandel, Phys. Rev. Lett. **56**, 58 (1986).
[9] B. Darquié, M. P. A. Jones, J. Dingjan, J. Beugnon, S. Bergamini, Y. Sortais, G. Messin, A. Browaeys, and P. Grangier, Science **309**, 454 (2005).
[10] Light emitted by a two-level atom into free space and partially collected by a high NA lens is no longer in an angular-momentum eigenstate. This makes it difficult to control the polarization in such a single-photon source.
[11] T. Wilk, H. P. Specht, S. C. Webster, and G. Rempe, quant-ph/0603083 [J. Mod. Opt. (to be published)].
[12] C. Schön, E. Solano, F. Verstraete, J. I. Cirac, and M. M. Wolf, Phys. Rev. Lett. **95**, 110503 (2005).
[13] T. Legero, T. Wilk, A. Kuhn, and G. Rempe, Appl. Phys. B **77**, 797 (2003).
[14] T. Legero, T. Wilk, M. Hennrich, G. Rempe, and A. Kuhn, Phys. Rev. Lett. **93**, 070503 (2004).
[15] E. Knill, R. Laflamme, and G. J. Milburn, Nature (London) **409**, 46 (2001).
[16] T. Legero, T. Wilk, A. Kuhn, and G. Rempe, Adv. At. Mol. Opt. Phys. **53**, 253 (2006).
[17] C. K. Hong, Z. Y. Ou, and L. Mandel, Phys. Rev. Lett. **59**, 2044 (1987).
[18] S. Nußmann, K. Murr, M. Hijlkema, B. Weber, A. Kuhn, and G. Rempe, Nature Phys. **1**, 122 (2005).

LETTERS

A single-photon server with just one atom

MARKUS HIJLKEMA[1], BERNHARD WEBER[1], HOLGER P. SPECHT[1], SIMON C. WEBSTER[1], AXEL KUHN[2] AND GERHARD REMPE[1]*

[1]Max-Planck-Institut für Quantenoptik, Hans-Kopfermann-Str. 1, D-85748 Garching, Germany
[2]Department of Physics, University of Oxford, Clarendon Laboratory, Parks Road, Oxford OX1 3PU, UK
*e-mail: gerhard.rempe@mpq.mpg.de

Published online: 11 March 2007; doi:10.1038/nphys569

Neutral atoms are ideal objects for the deterministic processing of quantum information. Entanglement operations have been carried out by photon exchange[1] or controlled collisions[2], and atom–photon interfaces have been realized with single atoms in free space[3,4] or strongly coupled to an optical cavity[5,6]. A long-standing challenge with neutral atoms, however, is to overcome the limited observation time. Without exception, quantum effects appeared only after ensemble averaging. Here, we report on a single-photon source with one, and only one, atom quasi-permanently coupled to a high-finesse cavity. 'Quasi-permanent' refers to our ability to keep the atom long enough to, first, quantify the photon-emission statistics and, second, guarantee the subsequent performance as a single-photon server delivering up to 300,000 photons for up to 30 s. This is achieved by a unique combination of single-photon generation and atom cooling[7–9]. Our scheme brings deterministic protocols of quantum information science with light and matter[10–16] closer to realization.

Deterministic single-photon sources are of prime importance in quantum information science[17]. Such sources have been realized with neutral atoms, embedded molecules, trapped ions, quantum dots and defect centres[18]. All of these sources are suitable for applications where the indivisibility of the emitted light pulses is essential. For quantum computing or quantum networking, the emitted photons must also be indistinguishable. Such photons have so far only been produced with quantum dots[19] and atoms[20,21]. Another requirement is a high efficiency. This is hard to obtain in free space, as the light-collecting lens covers only a fraction of the full 4π solid angle. The efficiency can be boosted by strongly coupling the radiating object to an optical microcavity, as has been achieved with atoms[5,6] and quantum dots[22]. An additional advantage of the cavity is that a vacuum-stimulated Raman adiabatic passage can be driven in a multilevel atom[6,23,24]. In this way, the amplitude[5,24], frequency[20] and polarization[25] of the photon can be controlled. It should also be possible to combine partial photon production with internal atomic rotations for the construction of entangled photon states such as W and GHZ states[15].

All of these demands together have so far only been achieved with atoms in high-finesse microcavities. One reason is that neutral atoms are largely immune to perturbations, such as electric patch fields close to dielectric mirrors. However, atomic systems have always suffered from a fast atom loss. We have now implemented a cavity-based scheme, see Fig. 1, with a dipole laser for trapping, a trigger laser for photon generation and a recycling laser for repumping, monitoring and cooling the atom[8,9]. The scheme combines high photon-generation efficiency and long trapping times. The most remarkable features are, first, that the single-photon stream is specified by its intensity correlation function evaluated in real-time during a short time interval after system preparation and, second, that its subsequent performance is guaranteed by monitoring the atom without perturbing the single-photon stream. This makes our single-photon source a useful quantum device operating with just one atom.

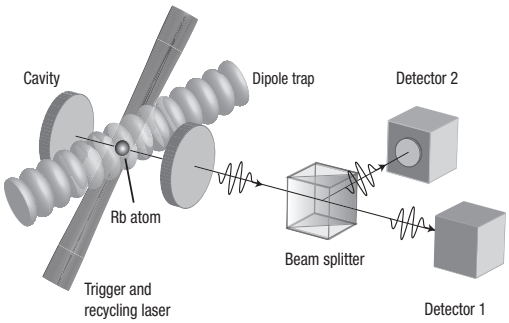

Figure 1 Schematic diagram of the apparatus. A single ^{85}Rb atom is trapped in a high-finesse optical microcavity by means of a two-dimensional optical lattice. Confinement along the cavity axis and a direction perpendicular to it is achieved with a weak cavity-stabilization laser and a strong retroreflected dipole laser, respectively. Confinement along the third direction results mainly from the small beam waist of the dipole laser. The atom–cavity system is excited by a sequence of laser pulses incident under an angle of 45° to the dipole laser and perpendicular to the cavity axis. Single photons emitted from the system are detected by two avalanche photodiodes in the Hanbury Brown and Twiss configuration. For simplicity, details of the set-up such as the set of prisms and interference filters in front of the detectors are not shown.

The main parts of the apparatus are described elsewhere[8,26], but changes were made to allow for single-photon generation and detection in combination with atom cooling. In short, ^{85}Rb atoms are collected from a background vapour in a magneto-optical trap, loaded into a running-wave dipole trap (wavelength 1,032 nm) and transferred into the optical high-finesse cavity. On arrival, a few atoms are captured by switching the geometry of the dipole trap to a standing wave and turning on 780-nm lasers perpendicular

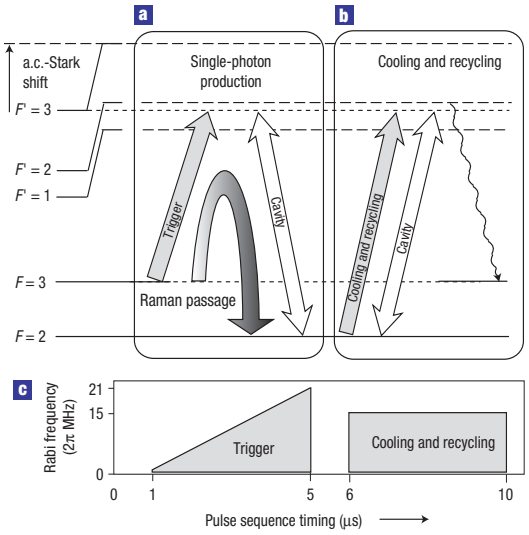

Figure 2 Simplified energy-level diagram. a,**b**, During single-photon production (**a**), the ^{85}Rb atom is excited by a 4-μs-long pulse of a trigger laser resonant with the $F=3 \rightarrow F'=3$ transition between the $5S_{1/2}$ ground and $5P_{3/2}$ excited state. With the cavity resonant with the $F=2 \rightarrow F'=3$ transition, this drives a vacuum-stimulated Raman adiabatic passage from $F=3$ to $F=2$, leading to the emission of a photon from the cavity (**b**). One microsecond later, a 4-μs-long laser pulse is used to recycle the atom back into the $F=3$ state. This laser is resonant with the cavity and the $F=2 \rightarrow F'=3$ transition. As the presence of the trapping potential leads to a dynamic energy-level shift (the a.c.-Stark shift) of $\Delta_S \approx 2\pi \times 70$ MHz, 7 MHz larger than the atomic hyperfine splitting between the $F'=2$ and $F'=3$ states, all lasers and the cavity are red-detuned from the atomic transitions from the ground states to the $F'=2$ excited state by a few MHz. This results in a situation where the atom can cycle a few times, scattering photons into the cavity, before falling back into the $F=3$ state. This cycling cools the atom. **c**, The timing sequence of the laser pulses with their pulse shapes.

to the cavity axis for three-dimensional cavity cooling[8]. The cavity has a length of 0.5 mm, a mode waist of 29 μm and a finesse of 3×10^4. The relevant parameters are $(g, \kappa, \gamma) = 2\pi \times (5, 5, 3)$ MHz, where g is the maximum atom–cavity coupling constant on the $F=2 \rightarrow F'=3$ transition between the atomic $5S_{1/2}$ ground and $5P_{3/2}$ excited state, κ is the cavity-field decay rate and γ is the atomic dipole decay rate. One of the cavity mirrors has a 50 times higher transmittance than the other. Photons scattered into the cavity by the trapped atom and emitted through this output mirror are spectrally and spatially filtered from the light of a cavity-stabilization laser at 785 nm and stray light, respectively, by means of cascaded glass prisms in combination with interference filters and pinholes. Finally, the photons are counted by two avalanche photodiodes. The combined background count rate due to stray light and dark counts is 84 Hz.

Figure 2 shows the three-level system that enables single-photon production and atom cooling. Starting with a single atom in the $F=3$ ground state, a trigger pulse together with the cavity drives a vacuum-stimulated Raman adiabatic passage[23,27] into the $F=2$ ground state (see Fig. 2a). This generates a single photon that is emitted from the cavity. Next, the atom is pumped back to the initial $F=3$ state with a recycling laser resonant with the cavity (see Fig. 2b). During this recycling process, the atom can scatter many photons into the cavity. To understand the scattering process in more detail, the $k_B \times 1.5$ mK deep dipole trap has to be taken into account (k_B is Boltzmann's constant). The trap shifts the atomic resonances by $\Delta_S \approx 2\pi \times 70$ MHz, the dynamic Stark shift. As shown in Fig. 2a,b, all of the lasers and the cavity are not resonant with the atom. This has little consequence for the photon production in the Raman process as both ground states experience the same shift. For the recycling laser, however, it creates a situation similar to one described earlier, with a strong Sisyphus-like cooling force[8,9]. This occurs even though the atomic transition used is not closed so that cooling takes place only as long as the atom cycles between the ground and excited state. Note that full three-dimensional cavity cooling is used only for the initial trapping of the atom. Here, both the trigger laser (now acting as a repumper) and the recycling laser are turned on continuously. This can keep the atom in the cavity for up to 1 min.

While applying the photon-production and recycling pulses, atoms stay in the cavity for 10.3(1) s on average, as determined from 526 experimental runs. This is about twice as long as in the dark dipole-force trap. Taking into account that initially several atoms are trapped and that we have to wait until all but one of the atoms have escaped the cavity, this gives 4,379 s of single-atom data with 4.23×10^6 detection events during trigger pulses, of which 0.15×10^6 are background detections. Single atoms are available for single-photon production for 8.3(2) s on average. For a trigger rate of 100 kHz, the overall photon generation, propagation and detection probability then amounts to 0.93%. This includes 50% cavity absorption loss mainly due to a mirror defect, 52% propagation loss from the cavity to the detectors and 44% quantum efficiency of the detectors. The photon-generation probability is therefore 9%. The finite efficiency is attributed to the large number of Zeeman states, some of them exhibiting a small (for example, $g = 2\pi \times 1.4$ MHz) atom–cavity coupling constant. In addition, because the coupling constant and the dynamic Stark shift are position dependent, the residual motion of the atom in the trap may play a role.

We calculate the cross-correlation of the recorded photon stream binned over 4-μs-long intervals corresponding to the trigger pulses (discarding detection events outside the trigger pulse). Summed over the 526 runs, this gives 1.2×10^4 correlations on average for each time bin. This gives 22 correlations per atom per bin. For a pulsed light source, correlations appear periodic with the repetition rate. For single photons equal-time coincidences do not occur. This absence of correlations at $\Delta\tau = 0$ is referred to as antibunching. The measured antibunching visibility averaged over the 526 runs is 94.0%.

The large number of correlations observed per atom and the large visibility of the antibunching suggests the following measurement protocol for single-atom operation, see Fig. 3. First, the system is initialized by trapping a few atoms and monitoring the light level emitted from the cavity during recycling pulses. When this level reaches a value expected for one atom (4 photons ms^{-1} on average), the photons emitted during trigger pulses within the next 1.5 s are recorded and the cross-correlation of the (binned) photon stream is calculated, see Fig. 3a, left inset. Next, the data are tested against the selection rule that the average number of correlations for non-zero time differences must exceed 1.5 (to make sure that at least one atom is trapped, leading to four correlations on average) and that correlations at zero time difference must not exceed 30% of this average. The latter condition makes sure that not more than one atom is trapped, a conclusion that in our experiment cannot be obtained from the scattering rate alone, as two (or more) weakly coupled atoms could produce the same fluorescence signal as one strongly coupled atom. We find that 86% of all 526 runs pass such a test. This leaves 454 runs with 3,774 s of true single-photon data with on average 1.0×10^4 correlations at non-zero time difference

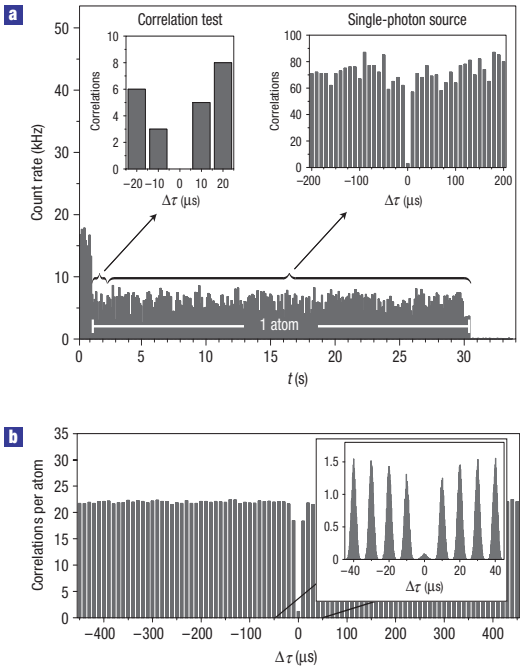

Figure 3 Photon statistics of our single-photon server. a, Performance for just one atom. The light emitted from the cavity during single-photon production and recycling is plotted versus time for one experimental run. Initially, a few atoms are trapped in the cavity. After 1 s, the average count rate drops to the single-atom level. To verify that exactly one atom is trapped, we calculate the cross-correlation of the photons recorded by the two detectors during trigger pulses for the next 1.5 s. A single atom manifests itself by the absence of coincidences for zero detection-time difference, $\Delta\tau = 0$, in the correlation function, as shown in the upper left inset. The upper right inset shows the correlation function obtained from the remaining 28-s-long single-photon stream, containing $\sim 2.8 \times 10^5$ single photons, of which we detect 11%. For this specific experimental run, antibunching has a visibility of 95.8%. **b**, Average behaviour. Correlation function averaged over those 454 single-atom runs that passed the qualification procedure described in the text. Antibunching has a visibility of 94.6%, limited only by background counts. The similarity of the single-atom trace shown in **a** compared to the average behaviour demonstrates the deterministic character of our source. The inset shows the averaged correlation function with a time resolution of 200 ns. The comb structure is due to the pulsed nature of the experiment.

and 534 coincidences at zero time difference. From our background count rate, we would expect 587(24) coincidences of a photon click with a background click. The measured antibunching with its visibility of 94.6% is therefore entirely limited by dark counts and stray light.

A single-atom source that passed the described selection procedure therefore emits a high-quality stream of single photons. A user of the photons can be notified and the photons redirected as needed. While this is done, the presence of the atom is monitored by detecting the light emitted during the recycling pulses. A loss of the atom manifests itself by the absence of scattered photons that can be detected within ~30 ms with 98% probability. In the right inset of Fig. 3a, the photon correlation function is plotted for those photons that would have been sent to the user. For comparison, the correlation function for all 454 runs is shown in Fig. 3b. The correlation signal obtained for one-and-the-same atom clearly shows the antibunching that is otherwise observed only after averaging over an ensemble of single atoms. Note that in contrast to all previous single-atom experiments, the single-atom nature of our system is obtained from a non-classical correlation signal, not a classical average of the emitted photon stream. This unambiguously discriminates a single atom from several atoms.

In summary, our atom–cavity system has progressed from a proof-of-principle single-photon source to a useful device whose performance is specified during operation. The quasi-permanent availability of exactly one atom, the high efficiency of photon production in a well-defined light mode and the large duty cycle of the whole measurement sequence paves the way for deterministic atom–photon and atom–atom entanglement experiments such as a test of Bell's inequality with distant atoms.

Received 22 December 2006; accepted 8 February 2007; published 11 March 2007.

References

1. Raimond, J. M., Brune, M. & Haroche, S. Colloquium: Manipulating quantum entanglement with atoms and photons in a cavity. *Rev. Mod. Phys.* **73**, 565–582 (2001).
2. Mandel, O. *et al.* Controlled collisions for multi-particle entanglement of optically trapped atoms. *Nature* **425**, 937–940 (2003).
3. Darquié, B. *et al.* Controlled single-photon emission from a single trapped two-level atom. *Science* **309**, 454–456 (2005).
4. Volz, J. *et al.* Observation of entanglement of a single photon with a trapped atom. *Phys. Rev. Lett.* **96**, 030404 (2006).
5. Kuhn, A., Hennrich, M. & Rempe, G. Deterministic single-photon source for distributed quantum networking. *Phys. Rev. Lett.* **89**, 067901 (2002).
6. McKeever, J. *et al.* Deterministic generation of single photons from one atom trapped in a cavity. *Science* **303**, 1992–1994 (2004).
7. Maunz, P. *et al.* Cavity cooling of a single atom. *Nature* **428**, 50–52 (2004).
8. Nußmann, S. *et al.* Vacuum-stimulated cooling of single atoms in three dimensions. *Nature Phys.* **1**, 122–126 (2005).
9. Murr, K. *et al.* Three-dimensional cavity cooling and trapping in an optical lattice. *Phys. Rev. A* **73**, 063415 (2006).
10. Cirac, J. I., Zoller, P., Kimble, H. J. & Mabuchi, H. Quantum state transfer and entanglement distribution among distant nodes in a quantum network. *Phys. Rev. Lett.* **78**, 3221–3224 (1997).
11. Pellizzari, T. Quantum networking with optical fibres. *Phys. Rev. Lett.* **79**, 5242–5245 (1997).
12. Browne, D. E., Plenio, M. B. & Huelga, S. F. Robust creation of entanglement between ions in spatially separate cavities. *Phys. Rev. Lett.* **91**, 067901 (2003).
13. Clark, S., Peng, A., Gu, M. & Parkins, S. Unconditional preparation of entanglement between atoms in cascaded optical cavities. *Phys. Rev. Lett.* **91**, 177901 (2003).
14. Duan, L.-M. & Kimble, H. J. Scalable photonic quantum computation through cavity-assisted interactions. *Phys. Rev. Lett.* **92**, 127902 (2004).
15. Schön, C., Solano, E., Verstraete, F., Cirac, J. I. & Wolf, M. M. Sequential generation of entangled multiqubit states. *Phys. Rev. Lett.* **95**, 110503 (2005).
16. Serafini, A., Mancini, S. & Bose, S. Distributed quantum computation via optical fibres. *Phys. Rev. Lett.* **96**, 010503 (2006).
17. Monroe, C. Quantum information processing with atoms and photons. *Nature* **416**, 238–246 (2002).
18. Grangier, P., Sanders, B. & Vuckovic, J. (eds) Focus issue on single photons on demand *New J. Phys.* **6**, 85–100; 129; 163 (2004).
19. Santori, C., Fattal, D., Vučković, J., Solomon, G. S. & Yamamoto, Y. Indistinguishable photons from a single-photon device. *Nature* **419**, 594–597 (2002).
20. Legero, T., Wilk, T., Hennrich, M., Rempe, G. & Kuhn, A. Quantum beat of two single photons. *Phys. Rev. Lett.* **93**, 070503 (2004).
21. Beugnon, J. *et al.* Quantum interference between two single photons emitted by independently trapped atoms. *Nature* **440**, 779–782 (2006).
22. Press, D. *et al.* Photon antibunching from a single quantum dot-microcavity system in the strong coupling regime. Preprint at <http://www.arxiv.org/quant-ph/0609193> (2006).
23. Hennrich, M., Legero, T., Kuhn, A. & Rempe, G. Vacuum-stimulated Raman scattering based on adiabatic passage in a high-finesse optical cavity. *Phys. Rev. Lett.* **85**, 4872–4875 (2000).
24. Keller, M., Lange, B., Hayasaka, K., Lange, W. & Walther, H. Continuous generation of single photons with controlled waveform in an ion-trap cavity system. *Nature* **431**, 1075–1078 (2004).
25. Wilk, T., Webster, S. C., Specht, H. P., Rempe, G. & Kuhn, A. Polarization-controlled single photons. *Phys. Rev. Lett.* **98**, 063601 (2007).
26. Nußmann, S. *et al.* Submicron positioning of single atoms in a microcavity. *Phys. Rev. Lett.* **95**, 173602 (2005).
27. Kuhn, A., Hennrich, M., Bondo, T. & Rempe, G. Controlled generation of single photons from a strongly coupled atom-cavity system. *Appl. Phys. B* **69**, 373–377 (1999).

Acknowledgements

This work was supported by the Deutsche Forschungsgemeinschaft (SFB 631 and Research Unit 635) and the European Union (IST (SCALA) and IHP (CONQUEST) programs).
Correspondence and requests for materials should be addressed to G.R.

Competing financial interests

The authors declare no competing financial interests.

PRL 99, 013002 (2007) PHYSICAL REVIEW LETTERS week ending 6 JULY 2007

Trapping and Observing Single Atoms in a Blue-Detuned Intracavity Dipole Trap

T. Puppe, I. Schuster, A. Grothe, A. Kubanek, K. Murr, P. W. H. Pinkse, and G. Rempe*

Max-Planck-Institut für Quantenoptik, Hans-Kopfermann-Str. 1, D-85748 Garching, Germany

(Received 15 February 2007; published 6 July 2007)

A single atom strongly coupled to a cavity mode is stored by three-dimensional confinement in blue-detuned cavity modes of different longitudinal and transverse order. The vanishing light intensity at the trap center reduces the light shift of all atomic energy levels. This is exploited to detect a single atom by means of a dispersive measurement with 95% confidence in 10 μs, limited by the photon-detection efficiency. As the atom switches resonant cavity transmission into cavity reflection, the atom can be detected while scattering about one photon.

DOI: 10.1103/PhysRevLett.99.013002 PACS numbers: 32.80.Pj, 42.50.Pq

A single atom coupled to a single mode of a high-finesse optical cavity constitutes an ideal system for the investigation of matter-light interaction at the level of individual quanta. Any application of this system, e.g., in quantum information science [1], relies on the ability to precisely localize the atom within the cavity mode at regions of strong atom-cavity coupling. An established tool to reach this goal is an optical dipole-force trap [2]. So far, only traps with lasers red detuned from the atom have been demonstrated in cavity quantum electrodynamics (QED) [3–6]. In such a red-detuned dipole trap, the atom is attracted towards intensity maxima. While this has the advantage that a single light mode is sufficient, it has the disadvantage that the high laser intensity perturbs the atom. As a consequence, the dynamic Stark effect shifts the atomic energy levels and, hence, the transition frequency. Moreover, increasing the trap depth for better localization of the atom will increase the Stark shift. For some atoms, like cesium, the Stark shift of a particular transition *between* certain energy levels vanishes in a red dipole trap at a magic wavelength [7]. An alternative approach is to use a blue-detuned light field for trapping. Here, the atom is repelled from the high-intensity region and, hence, trapped close to an intensity minimum. Such a trap has the advantage that the Stark shift of *all* states can be very small so that the free-space properties of the atom are largely retained. Superposition states, for example, will be less affected by the trapping potential.

In this Letter, we report on trapping single rubidium atoms in a blue-detuned intracavity dipole trap. We show that the Stark shift of the atomic transition vanishes while the atom is strongly coupled to a cavity mode. The blue trap allows us to explore the regime of dispersive single-atom observation. As a proof of principle, we demonstrate that the atom is efficiently detected while scattering only a few spontaneous photons.

The idea of the blue trap is to use far-detuned cavity modes to shape a potential landscape which realizes three-dimensional confinement around a dark trap center (Fig. 1). The standing wave of the high-finesse cavity guarantees maximum contrast of the interference pattern. The trap center is therefore accurately dark. Such a blue trap has a number of advantages for experiments in cavity QED: (1) Since the trap height does not contribute to the atomic detuning, it can be made large for good confinement. (2) An atom inside the trap is well isolated by the surrounding potential barrier; outside atoms are repelled. (3) The blue trap can be loaded by creating a dark funnel to guide a slow atom to the trap center. As the atom is repelled from the blue light, the kinetic energy does not increase during the capture process. Moreover, weakly coupled atoms that are not collected by the funnel are rejected. (4) The funnel can be closed upon detection of the strongly-coupled atom in the trap center. Because the energy gain due to guiding and switching is kept small,

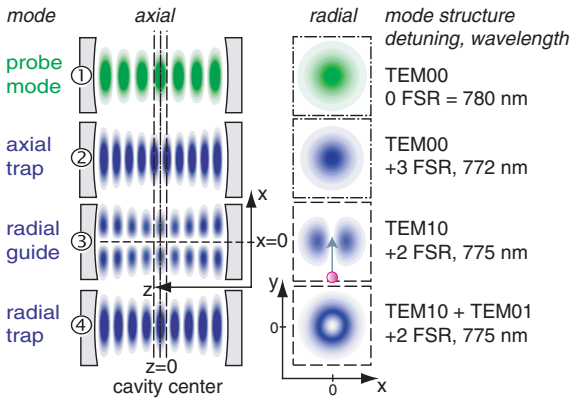

FIG. 1 (color online). The blue intracavity dipole trap from the perspective of an entering atom. The slow atom is restricted to the field minima of the blue light fields that coincide with the antinodes of the near-resonant probe mode no. 1 at the cavity center. Persistent *axial* confinement is provided by a TEM_{00} mode no. 2, "pancakes." Combined with the *transverse* nodal line of a TEM_{10} mode no. 3, funnels are formed to guide the atom to a strong-coupling region. Full three-dimensional confinement is achieved by adding a TEM_{01} mode to complete a transverse "doughnut" mode no. 4.

PRL 99, 013002 (2007) PHYSICAL REVIEW LETTERS week ending 6 JULY 2007

the requirement to cool the atom after the capture process is relaxed. (5) Since during the whole loading sequence the atomic detuning is preserved, parameter regimes of large cavity-enhanced heating [8,9] can be avoided.

The experimental setup presented in Fig. 2 is an extension of the one described in detail elsewhere [10,11]. The intracavity dipole potential is created by a combination of standing-wave cavity modes of different longitudinal and transverse mode order (Fig. 1), all blue detuned with respect to the near-resonant cavity QED probe field: persistent axial confinement along the cavity axis is provided by a TEM_{00} mode no. 2 detuned by an odd number of free-spectral ranges (FSR). The oblate antinodes (''pancakes'') of this mode confine the atom to the nodal planes that overlap with the antinodes of the probe mode no. 1 halfway between the mirrors. Radial confinement is provided by a doughnut mode no. 4 formed by a combination of TEM_{10} and TEM_{01} modes detuned by an even number of FSR. To load an atom into the trap, the radial confinement is relaxed by using the TEM_{10} mode only. Slow atoms from an atomic fountain are injected from below along the y-direction. They are guided towards the cavity center at $x = 0$ along the nodal line of this TEM_{10} mode no. 3. The combination of axial confinement and transverse guiding creates funnels that direct the atom to the antinodes of the probe mode no. 1. Note that the axial confinement need not be switched to close the trap. Since the axial and radial characteristics of the trap are defined by independent modes at different frequencies, they can be controlled individually.

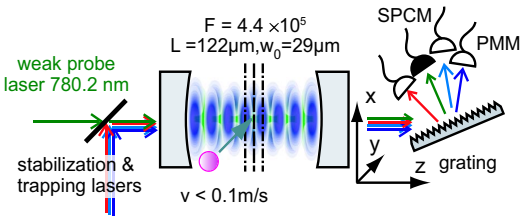

FIG. 2 (color online). Experimental setup. Slow ^{85}Rb atoms are injected from below into a high-finesse cavity. The cavity is excited by a weak near-resonant probe field at 780.2 nm and strong blue-detuned dipole fields. Behind the cavity, a grating directs the probe light onto single-photon counting modules (SPCM) whereas all dipole beams are detected by photomultiplier modules (PMM). The cavity length $L = 0.122$ mm is independently stabilized by a weak laser at 785.2 nm. Midway between the mirrors, the trap center coincides with an antinode of the probe field. The mode profiles in the dash-dotted and the dashed central plane are discussed in Fig. 1. The waist of the 780.2 nm fundamental transverse mode is $w_0 = 29\ \mu$m, and $F = 4.4 \times 10^5$ is the cavity finesse. The maximum atom-cavity coupling constant and the decay rates of the atomic polarization and the cavity field are $(g_0, \gamma, \kappa)/2\pi = (16, 3, 1.4)$ MHz, respectively.

A sample trace of a trapping event is presented in Fig. 3. Shown is the cavity transmission of the near-resonant probe laser at 780.2 nm and of the blue-detuned dipole laser providing the radial confinement. The persistent *axial* confinement at 772 nm (3 FSR detuned from the atom) , mode no. 2, amounts to a maximum potential height of $U_a = h \times 346$ MHz, with Planck constant h. The guiding field at 775 nm (2 FSR detuned from the atom), mode no. 3, produces a potential with height $U_g = 2h \times 10.3$ MHz [12]. The probe laser is on resonance with the bare cavity, $\Delta_c = \omega_l - \omega_c = 0$. Thus, the presence of an atom detunes the cavity from resonance and causes a decrease in the transmission. Slow atoms are guided to regions of strong coupling and cause sharp transmission drops, indicator 5. The trigger is armed $t = 205$ ms after launch of the atoms from the atomic fountain to select late atoms arriving with velocities below 0.1 $\mathrm{m/s}^{-1}$. Upon detection of a strongly-coupled atom in the cavity center (A), the atom is trapped by converting the transverse guiding mode to a confining doughnut mode no. 4 with a maximum potential height of $h \times 30$ MHz. Simultaneously, the probe intensity is reduced. When the atom leaves the mode, the cavity transmission increases to the bare cavity value for the reduced observation power (B). After each trapping event, the

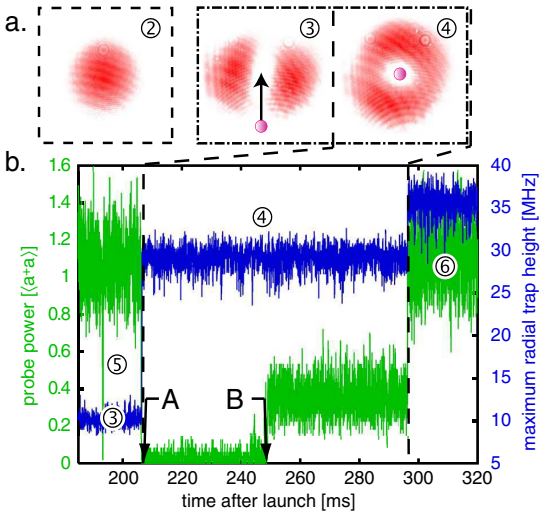

FIG. 3 (color online). A blue-trapping event. (a) Experimental intensity patterns of the different modes (cp. Figure 1). (b) Sample trace: Transmitted probe power in units of intracavity photon number, $\langle a^\dagger a \rangle$, and the maximum radial trap height. Upon detection of an atom (A), the probe intensity is decreased, and the trap is closed. When the atom leaves (B), the empty cavity transmission is observed. Experimentally, the doughnut mode no. 4 is a controlled superposition of two nondegenerate eigenmodes defined by our cavity. The trace is taken for detunings of continuous axial cavity cooling $(\Delta_{ac}, \Delta_c)/(2\pi) = (-35, 0)$ MHz, where the average storage time for single trapped atoms is about 30 ms.

PRL 99, 013002 (2007) PHYSICAL REVIEW LETTERS week ending 6 JULY 2007

stabilization of all lasers and the cavity is checked, region 6.

Spectroscopy of the combined atom-cavity system allows us to determine the main characteristics of the blue trap. The experimental protocol consists of a sequence of alternating 0.5 ms long cooling and 0.1 ms short probing intervals. The probe detuning in the probe intervals is scanned with respect to the bare cavity frequency, which is 35(1) MHz blue detuned from the atomic frequency. During the cooling intervals, the probe is on resonance with the bare cavity ($\Delta_c = 0$) which allows for cavity cooling in the axial direction as well as independent qualification of the atom-cavity coupling [5]. A probe interval is qualified for having a strong atom-cavity coupling when the cavity transmission in the neighboring cooling intervals is below 10% of the bare cavity transmission. The expectation value of the photon number in the cavity mode is calculated from the measured photon-detection rate and the known detection efficiency including propagation losses from the cavity to the detectors. Experimental results are displayed in Fig. 4. We purposely chose a large atom-cavity detuning, $\Delta_c > 2g_0$, with $g_0/2\pi = 16$ MHz the maximum atom-cavity coupling constant, to show that the blue trap preserves this detuning and allows to enter the regime of dispersive detection, as discussed below. Analytical results for an atom with fixed coupling (solid curve) fit the data (points) well. Comparison between theory and experiment gives an atom-cavity coupling constant of 83(12)% of g_0, much larger than the atomic and

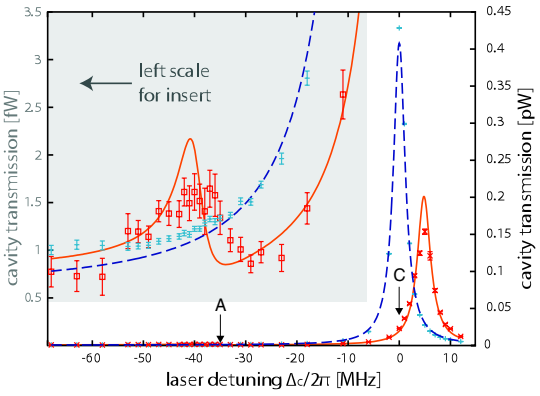

FIG. 4 (color online). Normal-mode spectrum: transmission as a function of detuning for a well-coupled system (squares and crosses). The bare atom (A) is detuned from the bare cavity resonance (C) by $\Delta_{ac}/2\pi = -35$ MHz. A transmission of 1 pW corresponds to 1.2 intracavity photons. Intervals contribute to the spectrum if the transmission in the neighboring cooling intervals is <10% of the bare cavity value $\langle n_0 \rangle$. An analytical fit (solid line) for a fixed coupling g at low excitation results in $g = 0.83(12) \times g_0$ and a residual Stark shift of $\Delta_s/2\pi = 0.7(1.3)$ MHz. The empty cavity transmission (pluses, dashed line) is shown for reference.

cavity decay rates. This proves that a strongly-coupled atom-cavity system has been prepared.

In Fig. 4, the measured Lorentzian transmission peak of the bare cavity at $\Delta_c = 0$ MHz is shown for reference. The bare atom is at $\Delta_{ac}/2\pi = -35(1)$ MHz, with the uncertainty due to some residual magnetic field. The bare detunings are the same as those of the normal-mode experiment performed previously in a red dipole trap [11]. The obvious difference in the normal-mode spectra lies in the fact that in a red trap, the atomic resonance is shifted by approximately twice the ground-state trap depth, effectively bringing the atomic transition frequency close to resonance with the cavity at the trap center (see Fig. 2 in [11]). In contrast, the normal-mode spectrum of an atom stored in the blue-detuned trap does not show any shift of the atomic frequency, as expected for an atom trapped at the node of the blue field. Since the large atom-cavity detuning is preserved, the character of the normal modes emerging from the bare states remain largely "atomlike" and "cavitylike." The strong asymmetry of the peak heights arises from the fact that the system is excited via the cavity and observed in transmission. Therefore, the atomlike resonance is much weaker than the cavitylike resonance. The plots on shaded background are an enlargement of the spectrum ($\sim 130\times$) to present the atomlike peak located at approximately $\Delta_c/2\pi = -40$ MHz. This peak is slightly broadened by the spatial distribution of the atoms in the mode. A residual Stark shift $\Delta_s/2\pi = 0.7(1.3)$ MHz can be derived from the analytical fit [13]. This shift is much smaller than the axial and radial trap heights, $U_a = h \times 265(6)$ MHz and $U_r = h \times 30(1)$ MHz, respectively. The Stark shift due to the red-detuned stabilization laser at 785.2 nm is $\Delta_{stab}/2\pi = 2.2(1)$ MHz. The shift of the atomic transition frequency due to the blue trap is therefore smaller than the atomic linewidth.

The preservation of the large atom-cavity detuning facilitates dispersive measurements [10,14,15] while the blue trap provides confinement. This is exemplified by the detection of an atom in the cavity via the induced shift of the cavitylike normal mode. Such a measurement scheme keeps the atomic excitation low. To estimate the average number of spontaneously scattered photons during a certain observation time interval, we consider probing the system on resonance with the bare cavity. In the presence of a strongly-coupled atom, the cavity transmission of the probe is reduced by a factor of ~ 20. The transmission is a direct measure of the excitation of the mode corresponding to $\langle a^\dagger a \rangle$ photons. In the limit of weak excitation, the excitation probability of the atom is proportional to the photon number times the atomic Lorentzian: $\langle \sigma^+ \sigma^- \rangle = \langle a^\dagger a \rangle g^2/(\Delta_{ac}^2 + \gamma^2)$ where $a^\dagger(a)$ is the creation (annihilation) operator for cavity photons, and $\sigma^+(\sigma^-)$ is the atomic raising (lowering) operator. The atomic excitation $\langle \sigma^+ \sigma^- \rangle$ is therefore given by the cavity excitation $\langle a^\dagger a \rangle = 0.022$ [cp. (C) in Fig. 4] times a constant which depends on

PRL 99, 013002 (2007) PHYSICAL REVIEW LETTERS week ending 6 JULY 2007

the effective coupling, g, the atom-cavity detuning, Δ_{ac}, and the atomic linewidth, γ. The effective coupling was obtained from the experimental data in Fig. 4, and γ and Δ_{ac} are well known. The deduced average atomic excitation of $\langle\sigma^+\sigma^-\rangle = 3.1 \times 10^{-3}$ leads to a scattering rate into free-space given by $2\gamma\langle\sigma^+\sigma^-\rangle \approx 117$ kHz. Thus, during a time interval of 10 μs, the atom scatters 1.2(3) photons. This includes an overall experimental detection efficiency of 5% for photons lost from the cavity mode. A detailed analysis which assumes a 50% *a priori* probability of the presence of the atom in the cavity, i.e., maximum possible ignorance, and which takes into account the Poissonian statistics of the detected photons and all experimental imperfections, results in a 95% correct decision concerning the presence of the atom in this 10 μs long time interval. The required observation time interval scales inversely with the photon-detection efficiency which can be improved considerably.

While trapped, the atom heats up due to spontaneous emission and dipole-force fluctuations [8,9]. The latter heating process is largely compensated by cavity cooling [5]. For the parameters of Fig. 3, the average storage time is about 30 ms. For a different trap height, we also measured the storage time without the probe light to be about 20 ms. Moreover, we see the same dependence on the probe power as reported in Ref. [5], namely, a trapping time decreasing inversely with increasing probe power. The observed trapping times are comparable to those found in a red trap [11] mainly because radial heating is not compensated for. An increase of the storage time by several orders of magnitude can be achieved for cavity cooling in three dimensions, which requires illuminating the system from the side [16]. In this scheme, all probe lasers would be red detuned from both normal modes, such that light scattering increases the photon energy and, hence, cools the atom. Since in cavity cooling photons should predominantly be emitted via the cavity mode, this requires the lower dressed state to be "cavitylike." An advantage of this cooling scheme would be that it is efficient for a strongly-coupled atom at the trap center. Note that for a cooling laser resonant with the bare cavity ($\Delta_c = 0$), as is the case in the experiment underlying Fig. 4, cooling is achieved only for an atom close to a node. As a first step in this direction, we have successfully captured and stored single atoms in the blue trap for the appropriate parameters for 3D cavity cooling.

In conclusion, we have realized a blue intracavity dipole trap which now allows measurements in cavity QED while largely preserving the free-space level structure of the confined atom. Well controlled detunings and coupling are important for the investigation of genuine quantum effects, where a reliable coherent evolution is essential. For applications in quantum information science, the absence of differential energy shifts reduces dephasing of superposition states. Further perspectives for the blue trap include the possibility to control the atomic motion by means of feedback [17]. Such experiments would benefit from the possibility to independently address the radial and axial confinement. Moreover, in experiments where optical cavities are investigated as single-atom detectors [18–22], the blue "funnels" demonstrated in this Letter could efficiently guide atoms to regions of large atom-cavity coupling, thereby enhancing the detection efficiency.

*gerhard.rempe@mpq.mpg.de

[1] C. Monroe, Nature (London) **416**, 238 (2002).
[2] R. Grimm, M. Weidemüller, and Y. B. Ovchinnikov, Adv. At. Mol. Opt. Phys. **42**, 95 (2000).
[3] J. Ye, D. W. Vernooy, and H. J. Kimble, Phys. Rev. Lett. **83**, 4987 (1999).
[4] J. A. Sauer *et al.*, Phys. Rev. A **69**, 051804(R) (2004).
[5] P. Maunz *et al.*, Nature (London) **428**, 50 (2004).
[6] S. Nußmann *et al.*, Phys. Rev. Lett. **95**, 173602 (2005).
[7] J. McKeever *et al.*, Phys. Rev. Lett. **90**, 133602 (2003).
[8] G. Hechenblaikner, M. Gangl, P. Horak, and H. Ritsch, Phys. Rev. A **58**, 3030 (1998).
[9] K. Murr *et al.*, Phys. Rev. A **74**, 043412 (2006).
[10] P. Münstermann, T. Fischer, P. W. H. Pinkse, and G. Rempe, Opt. Commun. **159**, 63 (1999).
[11] P. Maunz *et al.*, Phys. Rev. Lett. **94**, 033002 (2005).
[12] The maximum radial trap height in Fig. 3 is given for the doughnut mode. Since it scales with the ratio of the maximum intensity to the integrated intensity, the trap height for the TEM_{01} guiding mode is a factor 2 larger.
[13] A conservative upper bound for the Stark shift of $\Delta_s/2\pi < 4$ MHz can be extracted from fitting only the slopes of the atomlike peak.
[14] R. Quadt, M. Collett, and D. Walls, Phys. Rev. Lett. **74**, 351 (1995).
[15] C. J. Hood, M. S. Chapman, T. W. Lynn, and H. J. Kimble, Phys. Rev. Lett. **80**, 4157 (1998).
[16] S. Nußmann *et al.*, Nature Phys. **1**, 122 (2005).
[17] T. Fischer *et al.*, Phys. Rev. Lett. **88**, 163002 (2002).
[18] P. Horak *et al.*, Phys. Rev. A **67**, 043806 (2003).
[19] M. Trupke *et al.*, Appl. Phys. Lett. **87**, 211106 (2005).
[20] A. Öttl, S. Ritter, M. Köhl, and T. Esslinger, Phys. Rev. Lett. **95**, 090404 (2005).
[21] T. Steinmetz *et al.*, Appl. Phys. Lett. **89**, 111110 (2006).
[22] I. Teper, Y.-J. Lin, and V. Vuletić, Phys. Rev. Lett. **97**, 023002 (2006).

PRL 99, 033201 (2007) PHYSICAL REVIEW LETTERS week ending 20 JULY 2007

Atom-Molecule Rabi Oscillations in a Mott Insulator

N. Syassen, D. M. Bauer, M. Lettner, D. Dietze, T. Volz, S. Dürr, and G. Rempe

Max-Planck-Institut für Quantenoptik, Hans-Kopfermann-Straße 1, 85748 Garching, Germany

(Received 17 April 2007; published 19 July 2007)

We observe large-amplitude Rabi oscillations between an atomic and a molecular state near a Feshbach resonance. The experiment uses ^{87}Rb in an optical lattice and a Feshbach resonance near 414 G. The frequency and amplitude of the oscillations depend on the magnetic field in a way that is well described by a two-level model. The observed density dependence of the oscillation frequency agrees with theoretical expectations. We confirmed that the state produced after a half-cycle contains exactly one molecule at each lattice site. In addition, we show that, for energies in a gap of the lattice band structure, the molecules cannot dissociate.

DOI: 10.1103/PhysRevLett.99.033201 PACS numbers: 34.50.−s, 03.75.Nt

In recent years, the field of ultracold molecular gases has undergone rapid progress. These systems have the potential for a variety of interesting applications, e.g., in precision measurements or in quantum simulations. As precision measurements are usually best performed in terms of frequency measurements, atom-molecule Rabi oscillations open up promising opportunities in this direction. Specifically, it was proposed recently that measurements of atomic scattering properties with moderate accuracy might be used to perform sensitive tests for drifts of fundamental constants [1]. Most of the work on molecule association so far has been based on adiabatically ramping a magnetic field across a Feshbach resonance [2–8]. Unlike adiabatic ramps, time-resolved Rabi oscillations allow for full control over the final superposition state produced. The pioneering experiment on molecule association recorded Ramsey oscillations between the atomic and the molecular state, but this experiment observed Rabi oscillations only ''over a very limited range'' of the magnetic field [9]. In a subsequent experiment, atom-molecule Rabi oscillations with 6% amplitude were induced using a radio-frequency field [10]. Atom-molecule Rabi oscillations were also reported in a photoassociation experiment [11]. In addition, oscillations between two bound molecular states were observed [12].

Here we report the experimental observation of time-resolved Rabi oscillations between the atomic and the molecular state with a large amplitude. The oscillations are weakly damped and the data show oscillations up to the 29th cycle. The observation of Rabi oscillations requires a pulse shape that is rectangular, or at least strongly diabatic. In free space, such pulses populate [9] the continuum of above-threshold entrance-channel states, thus leading to oscillations between many levels, typically with a small molecular amplitude. We avoid this by working in a deep three-dimensional optical lattice, where the entrance-channel states are discrete. For weak enough coupling, the coupling of the molecular state to only one entrance-channel state is noticeable. In addition, the lattice isolates the molecules from each other, thus suppressing loss due to inelastic collisions [13]. Our experiment starts from an atomic Mott insulator [14] prepared such that the central region of the cloud contains exactly two atoms at each lattice site. The quantum state reached after a half-cycle of the atom-molecule Rabi oscillation therefore contains exactly one molecule at each lattice site in this central region. We previously prepared the same state using an adiabatic ramp of the magnetic field [15,16]. In addition, we show that confinement-induced molecules exist not only below the lowest band of the lattice [17], but also in band gaps.

We use an optical lattice that is deep enough that tunneling is negligible. Here, each lattice site represents a simple harmonic trap with angular frequency $\omega_{\mathrm{ho}} = k\sqrt{2V_0/m}$, where $2\pi/k = 830.44$ nm is the wavelength of the lattice light, m the mass of an atom, and V_0 the lattice depth seen by an atom [15]. In contrast to the free-space case, the closed-channel molecular state $|\psi_m\rangle$ is coupled to only one discrete state, namely, the motional ground state $|\psi_a\rangle$ of two entrance-channel atoms at one lattice site. The matrix element $H_{am} = \langle\psi_a|H|\psi_m\rangle$ of the Hamiltonian H is [18,19]

$$H_{am} = \left[\frac{4\pi\hbar^2 a_{\mathrm{bg}}\Delta\mu\Delta B}{m(\sqrt{2\pi}a_{\mathrm{ho}})^3}\left(1 + 0.490\frac{a_{\mathrm{bg}}}{a_{\mathrm{ho}}}\right)\right]^{1/2}, \quad (1)$$

where $a_{\mathrm{ho}} = \sqrt{\hbar/m\omega_{\mathrm{ho}}}$ is the harmonic oscillator length, a_{bg} the background scattering length, ΔB the width of the Feshbach resonance, and $\Delta\mu$ the difference between the magnetic moments of an entrance-channel atom pair and a closed-channel molecule. At resonance, Rabi oscillations between the two states are expected to occur with angular frequency $\Omega_{\mathrm{res}} = 2H_{am}/\hbar$.

In addition to the coupling in Eq. (1), $|\psi_m\rangle$ can couple to excited s-wave trap states of the relative motion of two entrance-channel atoms [8]. This coupling between many states can lead to quite complex dynamics. In order to avoid this, we need a Feshbach resonance with $\Omega_{\mathrm{res}} \ll \omega_{\mathrm{ho}}$. For very small Ω_{res}, the magnetic-field noise δB_{rms} [21] becomes an issue, resulting in the condition $\delta B_{\mathrm{rms}}\Delta\mu/\hbar \ll \Omega_{\mathrm{res}} \ll \omega_{\mathrm{ho}}$. In the experiment, we choose

PRL 99, 033201 (2007) PHYSICAL REVIEW LETTERS week ending 20 JULY 2007

a Feshbach resonance in ^{87}Rb near 414 G with both incoming atoms in the hyperfine state $|F = 1, m_F = 0\rangle$ [22]. A coupled-channels calculation [23] predicts $a_{bg} = 100.8$ Bohr radii and $\Delta B = 18$ mG. The Breit-Rabi formula predicts $\Delta\mu = 2\pi\hbar \times 111$ kHz/G. This is an unusually small value that helps reducing Ω_{res} as well as the sensitivity to magnetic-field noise.

Our experiment starts with the preparation of an ultracold gas of ^{87}Rb atoms in the hyperfine state $|1, -1\rangle$ in a magnetic trap. When the gas is just above the critical temperature for Bose-Einstein condensation (BEC), it is transferred into an optical dipole trap, where a magnetic field of $\sim$1 G is applied to preserve the spin polarization of the atoms. Next, a magnetic field of $\sim$412 G is switched on rapidly. We deliberately create an angle between the two fields, so that the sudden turn-on populates all $F = 1$ Zeeman states. We then drive evaporative cooling by lowering the dipole trap potential. Because of the presence of a slight magnetic-field gradient, this preferentially removes atoms in states $|1, -1\rangle$ and $|1, 1\rangle$. We obtain an almost pure BEC with more than 90% of the population in the state $|1, 0\rangle$. Next, an optical lattice is slowly ramped up. The experimental parameters are chosen in such a way that the central region of the resulting Mott insulator contains exactly two atoms at each lattice site [15]. Unless otherwise noted, the lattice depth seen by an atom is $V_0 = 15E_r$, where $E_r = \hbar^2k^2/2m$ is the atomic recoil energy.

Subsequently, the magnetic field is jumped to a value very close to the 414-G Feshbach resonance. In response to the step in the externally applied field, eddy currents build up. We therefore use two subsequent steps of the magnetic field. The first step begins 2.4 G below the Feshbach resonance and ends typically 50 mG away from the Feshbach resonance, where mixing between states $|\psi_a\rangle$ and $|\psi_m\rangle$ is negligible. 250 μs later the eddy currents have fully settled and the second step is applied. The height of the second step is small enough that eddy currents have negligible effect. After this step, we hold the magnetic field for a variable time. Finally, magnetic field, lattice, and dipole trap are abruptly switched off and after 4 ms of free flight an absorption image is taken. The imaging light is resonant with an atomic transition so that molecules remain invisible.

The number of atoms as a function of hold time right at the Feshbach resonance B_{res} is shown in Fig. 1. The experimental data clearly show atom-molecule Rabi oscillations up to the 29th cycle. The data show damping in a way that the minimum atom number is essentially unchanged. This suggests that the decay is due to loss of population, as opposed to dephasing which would lead to damping towards the mean atom number. We therefore fit [24]

$$N(t) = N_1 + N_2 e^{-t/\tau} \frac{1 - \cos(\Omega_{Rabi} t)}{2} \qquad (2)$$

to the data. Both $|\psi_a\rangle$ and $|\psi_m\rangle$ can decay into lower-lying open two-atom channels. We measured the decay of population in state $|\psi_a\rangle$ 2.4 G below the Feshbach resonance and obtained a decay rate of less than 1 Hz. We therefore attribute the decay observed in Fig. 1 fully to the state $|\psi_m\rangle$. During a Rabi cycle, half of the time on average is spent in this state. Hence, the decay rate Γ of population in $|\psi_m\rangle$ can be extracted from the fit of Eq. (2) yielding $\Gamma = 2/\tau = 0.34(2)$ kHz.

The fraction of the population that participates in the oscillation at short time is $N_2/(N_1 + N_2) = 0.46(1)$. This value reflects the fraction of lattice sites that are initially occupied by two atoms [15]. The conversion efficiency at these sites is nearly 100%. We repeated the measurements of Ref. [15] in order to verify that the state produced here really is a quantum state in which the central region of the cloud contains exactly one molecule at each lattice site.

The frequency and amplitude of the Rabi oscillations depend on the magnetic-field value during the hold time after the second step. This dependence is shown in Fig. 2. As in any two-level system, the Rabi frequency is expected to follow a hyperbola

$$\Omega_{Rabi}(B) = \sqrt{\Omega_{res}^2 + [(B - B_{res})\Delta\mu/\hbar]^2}, \qquad (3)$$

where B_{res} is the resonance position which depends on the lattice depth V_0, as discussed further below. A fit to the data is shown in Fig. 2(a). The best-fit values are $\Omega_{res} = 2\pi \times 3.2(1)$ kHz and $\Delta\mu = 2\pi\hbar \times 112(2)$ kHz/G, in good agreement with the result of Fig. 1 and the theoretical prediction, respectively.

The amplitude of the Rabi oscillation is shown in Fig. 2(b) as a function of magnetic field. This amplitude

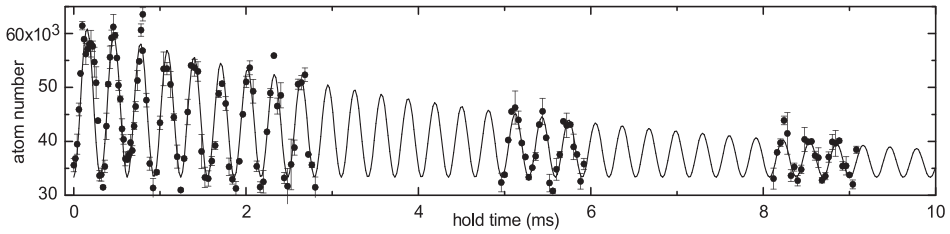

FIG. 1. Time-resolved Rabi oscillations between the atomic and the molecular state. The experimental data (●) show the number of entrance-channel atoms. The line shows a fit of Eq. (2) that yields $\Omega_{Rabi} = 2\pi \times 3.221(2)$ kHz and $\tau = 5.9(4)$ ms.

PRL 99, 033201 (2007) PHYSICAL REVIEW LETTERS week ending 20 JULY 2007

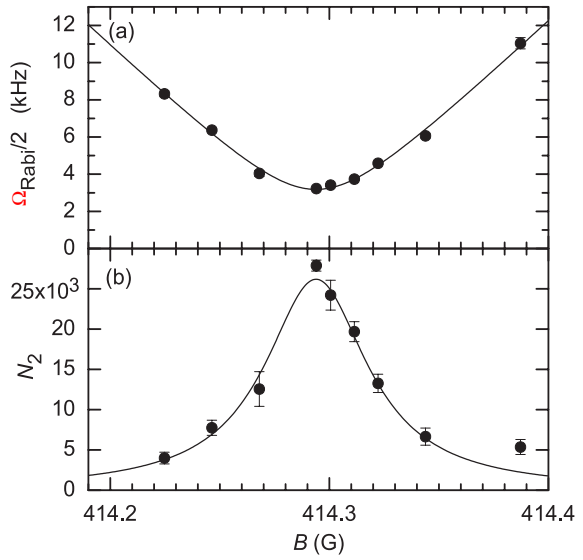

FIG. 2. Magnetic-field dependence of (a) the frequency and (b) the amplitude of the Rabi oscillations. The lines show fits to the experimental data (●).

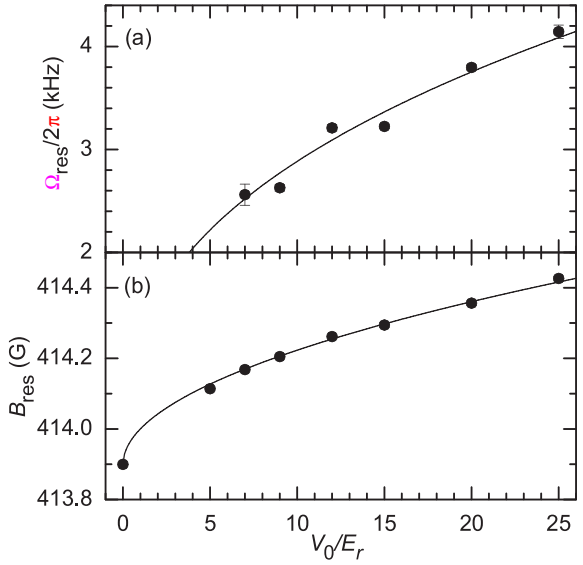

FIG. 3. Dependence of (a) the on-resonance Rabi frequency and (b) the Feshbach resonance position on lattice depth. The lines show fits to the data (●).

follows a Lorentzian $N_2(B) = N_{res}\Omega_{res}^2/\Omega_{Rabi}^2(B)$ which is shown in Fig. 2(b). We use only N_{res} as a free fit parameter and copy the values of the other parameters from the fit to Fig. 2(a).

Ω_{res} depends on the atomic density in the entrance-channel state. In Eq. (1) the corresponding effective volume is $(\sqrt{2\pi}a_{ho})^3/(1 + 0.49a_{bg}/a_{ho})$. We varied the lattice depth V_0 in order to verify this density dependence. Results are shown in Fig. 3(a). The line shows a fit of Eq. (1) to the data, where the only free fit parameter is the overall amplitude. As $\Delta\mu$ and a_{bg} can typically be predicted much more accurately than ΔB, we use this fit to determine $\Delta B = 15(1)$ mG, which agrees fairly well with theory. The dominant contribution to the error in ΔB comes from the calibration of V_0, which we perform in terms of a frequency measurement [16]. We estimate the relative error in V_0 to be 10%. This determination of ΔB is independent of the atom-number calibration, because only lattice sites with exactly two atoms contribute to the oscillation.

The measurements of Ω_{res} in Fig. 3(a) rely on a measurement of B_{res} as a function of lattice depth V_0. Results of this measurement are shown in Fig. 3(b). Based on the zero-point energy of the three-dimensional harmonic oscillator for the relative motion of the two atoms, one expects [17] $B_{res} = B_0 + 3\hbar\omega_{ho}/2\Delta\mu$, where B_0 is the value at $V_0 = 0$. The background scattering length a_{bg} causes a correction [26] yielding

$$B_{res} = B_0 + \frac{\hbar\omega_{ho}}{\Delta\mu}\left(\frac{3}{2} + \sqrt{\frac{2}{\pi}}\frac{a_{bg}}{a_{ho}}\right). \quad (4)$$

For magnetic fields between B_0 and B_{res}, the confinement thus stabilizes the molecules against dissociation that would occur in free space [17].

We measure $B_0 = 413.90$ G [27] and fit Eq. (4) to the data in Fig. 3(b) where we use V_0 as the only free fit parameter, entering the equation in $\omega_{ho}(V_0)$ and $a_{ho}(V_0)$. The fit yields a value of V_0 that is a factor of 1.20(2) larger than our independent calibration. This might mean that our independent calibration of V_0 is worse than we think it is, or else it means that other mechanisms have a significant effect. For example, the harmonic approximation used to derive Eq. (4) might be too inaccurate or the observed deviation might be explained as a differential ac-Stark shift between states $|\psi_a\rangle$ and $|\psi_m\rangle$ induced by the lattice light. The size of the differential ac-Stark shift would have to equal 2% of the total ac-Stark shift.

In a final measurement, we study the dissociation of $|\psi_m\rangle$ into excited trap states of the entrance channel. To this end, we induce Rabi oscillations as in Fig. 1 and then stop the oscillations at a point where the molecule fraction is large, by jumping the magnetic field to a different value, typically far above the lowest oscillator state. We hold the field there for 250 μs and then switch it off.

The observed number of entrance-channel atoms is shown in Fig. 4. The peak near 414.5 G corresponds to the lowest oscillator state. The signal at this peak is fairly small because the dissociation pulse duration of 250 μs happens to be close to a minimum of the Rabi oscillations, where only few molecules are dissociated. The peaks are approximately equidistant with a separation of $\sim$0.57 G, corresponding to an energy difference of $\sim 2\pi\hbar \times 63$ kHz

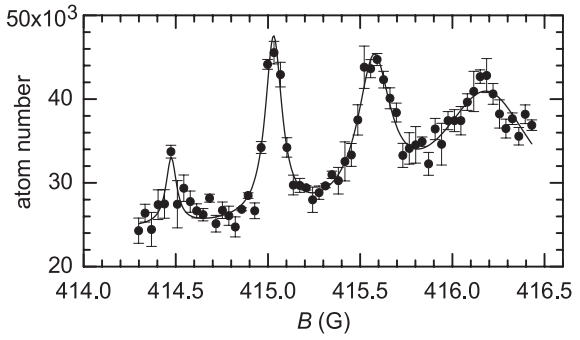

FIG. 4. Mapping the band structure using molecule dissociation. The separation of the peaks corresponds to $\sim 2\hbar\omega_{\mathrm{ho}}$; i.e., the molecules dissociate into even bands. Dissociation is suppressed in the band gaps, showing the existence of confinement-induced band-gap molecules. The data were obtained at $V_0 = 25E_r$. The line is a guide to the eye.

which is close to $2\hbar\omega_{\mathrm{ho}} = 2\pi\hbar \times 66$ kHz. Figure 4 shows a suppression of dissociation into odd bands of the lattice as well as into band gaps. The suppression in the gaps demonstrates that confinement-induced molecules can be created not only below the lowest band [17] but also in three-dimensional band gaps. We attribute the suppression of dissociation into odd bands to the fact that these bands have odd parity at quasi momentum zero. Hence, the s-wave state $|\psi_m\rangle$ cannot dissociate at quasimomentum zero. This measurement also profits from the reduced sensitivity to magnetic-field noise due to the small value of $\Delta\mu$.

Even when avoiding eddy currents as above, we see no Rabi oscillations for dissociation into the second band near 415.0 G. We attribute this to single-atom tunneling, which has an amplitude of $J = 2\pi\hbar \times 3.8$ kHz in the second band and leads to decoherence.

In conclusion, we observed large-amplitude atom-molecule Rabi oscillations in an optical lattice using a Feshbach resonance. The dependence of the oscillations on magnetic-field and lattice depth agrees well with a theoretical model. In addition, we observed confinement-induced band-gap molecules.

The oscillations observed here can be used for precision measurements of atomic scattering properties that could be employed in sensitive tests for drifts of fundamental constants. In addition, confinement-induced molecules offer more general perspectives to manipulate the stability of molecules by structured environments. Finally, the production of a coherent atom-molecule superposition state with controllable amplitude and phase opens up new possibilities for quantum simulations.

We thank S. Kokkelmans for providing predictions for the parameters of the Feshbach resonance. We acknowledge financial support of the German Excellence Initiative via the program Nanosystems Initiative Munich and of the Deutsche Forschungsgemeinschaft via SFB 631.

[1] C. Chin and V. V. Flambaum, Phys. Rev. Lett. **96**, 230801 (2006).
[2] C. A. Regal, C. Ticknor, J. L. Bohn, and D. S. Jin, Nature (London) **424**, 47 (2003).
[3] J. Herbig *et al.*, Science **301**, 1510 (2003).
[4] S. Dürr, T. Volz, A. Marte, and G. Rempe, Phys. Rev. Lett. **92**, 020406 (2004).
[5] K. E. Strecker, G. B. Partridge, and R. G. Hulet, Phys. Rev. Lett. **91**, 080406 (2003).
[6] J. Cubizolles *et al.*, Phys. Rev. Lett. **91**, 240401 (2003).
[7] K. Xu *et al.*, Phys. Rev. Lett. **91**, 210402 (2003).
[8] T. Köhler, K. Góral, and P. S. Julienne, Rev. Mod. Phys. **78**, 1311 (2006).
[9] E. A. Donley, N. R. Claussen, S. T. Thompson, and C. E. Wieman, Nature (London) **417**, 529 (2002).
[10] S. T. Thompson, E. Hodby, and C. E. Wieman, Phys. Rev. Lett. **95**, 190404 (2005).
[11] C. Ryu *et al.*, arXiv:cond-mat/0508201.
[12] M. Mark *et al.*, arXiv:0704.0653.
[13] G. Thalhammer *et al.*, Phys. Rev. Lett. **96**, 050402 (2006).
[14] M. Greiner *et al.*, Nature (London) **415**, 39 (2002).
[15] T. Volz *et al.*, Nature Phys. **2**, 692 (2006).
[16] S. Dürr *et al.*, in *Atomic Physics 20: XXth International Conference on Atomic Physics*, edited by Christian Roos, Hartmut Häffner, and Rainer Blatt, AIP Conf. Proc. No. 869 (AIP, New York, 2006), pp. 278–283.
[17] H. Moritz *et al.*, Phys. Rev. Lett. **94**, 210401 (2005).
[18] See EPAPS Document No. E-PRLTAO-99-011730 for a derivation of Eq. (1). For more information on EPAPS, see http://www.aip.org/pubservs/epaps.html.
[19] Equation (22) in Ref. [20] is a factor of $(3/\pi)^{1/4} \sim 0.99$ smaller and neglects the term $a_{\mathrm{bg}}/a_{\mathrm{ho}}$.
[20] P. S. Julienne, E. Tiesinga, and T. Köhler, J. Mod. Opt. **51**, 1787 (2004).
[21] S. Dürr, T. Volz, and G. Rempe, Phys. Rev. A **70**, 031601(R) (2004).
[22] A. Marte *et al.*, Phys. Rev. Lett. **89**, 283202 (2002).
[23] Servaas Kokkelmans (private communication).
[24] The signal in Fig. 1 has a minimum at $t = 0$ because for this data set, the first magnetic-field step ends 50 mG above the Feshbach resonance. Hence, the eddy currents effectively lead to an adiabatic ramp across the Feshbach resonance and associate molecules, as in Ref. [25].
[25] M. Mark *et al.*, Europhys. Lett. **69**, 706 (2005).
[26] T. Busch, B.-G. Englert, K. Rzążewski, and M. Wilkens, Found. Phys. **28**, 549 (1998).
[27] This value is 0.44 G smaller than in Ref. [22]. We attribute this to the fact that the loss feature observed in Ref. [22] at this particular resonance was extraordinarily broad, making an accurate determination of the resonance position in Ref. [22] very difficult.

REPORTS

Single-Atom Single-Photon Quantum Interface

Tatjana Wilk,[1] Simon C. Webster,[1] Axel Kuhn,[2] Gerhard Rempe[1]*

A major challenge for a scalable quantum computing architecture is the faithful transfer of information from one node to another. We report on the realization of an atom-photon quantum interface based on an optical cavity, using it to entangle a single atom with a single photon and then to map the quantum state of the atom onto a second single photon. The latter step disentangles the atom from the light and produces an entangled photon pair. Our scheme is intrinsically deterministic and establishes the basic element required to realize a distributed quantum network with individual atoms at rest as quantum memories and single flying photons as quantum messengers.

Cavity quantum electrodynamics with individually addressable atoms emitting single photons on demand is expected to provide an ideal toolbox for quantum networking and linear optical quantum computing (*1*). First, using a single atom makes it possible to produce single photons (*2*–*5*) with controlled waveform and polarization (*6*). Such light fields with zero multi-photon contribution are a key ingredient of scalable quantum networks (*7*) and quantum repeaters (*8*). Second, the strong atom-cavity coupling achievable in a high-finesse cavity allows the channeling of quantum information stored in atomic states into photons emitted in a well-defined direction. Compared with free-space schemes (*9*–*11*), this boosts the success probability by several orders of magnitude. It allows realizing deterministic protocols in quantum information science, in particular to entangle an atom with a photon, map quantum states between different information carriers such as an atom and a photon, and generate multi-photon entanglement (*12*). Related schemes have been demonstrated with Rydberg atoms passing through a lossless microwave resonator (*13*). Their implementation in a dissipative optical cavity generates the flying photons required for the above-mentioned applications.

We have realized the essential ingredient of an optical quantum network—namely, an atom-photon interface—using a high-finesse optical cavity containing a single ^{87}Rb atom. Strong atom-cavity coupling is achieved and allows for intrinsically deterministic photon emission. The triggered emission of a first photon entangles the internal state of the atom and the polarization state of the photon. In contrast to probabilistic experiments (*9*, *11*), the atomic state is not examined by using a shelving technique and detecting fluorescence photons. Instead, our scheme maps the atomic state onto the state of a second single photon. Such a state mapping is feasible because the atom-cavity system generates single photons very efficiently in a well-defined mode, which can easily be observed. As a result of the state mapping a pair of entangled photons is produced, one emitted after the other into the same mode. The polarization state of the two photons is analyzed by tomography, which also probes the prior entanglement between the atom and the first photon. As a first step toward local control of the memory qubit, we also show rotation of the atomic state between entanglement creation and state mapping. An extension of our scheme should allow stepwise engineering of entangled states with even higher photon number (*12*).

Our scheme (Fig. 1) shows a single ^{87}Rb atom coupled to an optical cavity and prepared in the $|F = 2, m_F = 0\rangle$ state of the $5S_{1/2}$ ground level. With the cavity axis as quantization direction, the cavity supports left- and right-handed circularly polarized σ^+ and σ^- modes. A π-polarized laser (resonant with the transition from $F = 2$ to $F' = 1$ of the excited $5P_{3/2}$ level) together with the cavity (coupling levels $F = 1$ and $F' = 1$) drives a vacuum-stimulated Raman adiabatic passage (*2*, *14*) to the $|F = 1\rangle$ state of the ground level. Two different paths to states $|\pm1\rangle \equiv |F = 1, m_F = \pm1\rangle$ are possible, resulting in the generation of a σ^- or a σ^+ photon, respectively. After photon emission the system is in the entangled state

$$|\Psi_{\text{atom,photon 1}}\rangle = \frac{1}{\sqrt{2}}(|+1,\sigma^-\rangle - |-1,\sigma^+\rangle) \quad (1)$$

where the phase of the superposition is defined by the transition amplitudes from the $|F = 2, m_F = 0\rangle$ state to the $|+1\rangle$ and $|-1\rangle$ states.

To map the atomic state onto a second photon, a π-polarized laser resonant with the transition from $F = 1$ to $F' = 1$, again together with the cavity, drives a second Raman adiabatic passage (Fig. 1B). The population in state $|+1\rangle$ is transferred to $|0\rangle \equiv |F = 1, m_F = 0\rangle$ and a σ^+ photon is emitted, whereas the population in $|-1\rangle$ is also transferred to $|0\rangle$, but a σ^- photon is emitted. The atom-photon entanglement is therefore converted into a polarization entanglement between two photons,

$$|\Psi_{\text{photon 2, photon 1}}\rangle = \frac{1}{\sqrt{2}}(|\sigma^+,\sigma^-\rangle - |\sigma^-,\sigma^+\rangle) \quad (2)$$

while the atom is disentangled from the light.

In the experiment (Fig. 2A), a dilute cloud of laser-cooled ^{87}Rb atoms falls through an optical high-finesse cavity (*6*). The maximum atom-cavity coupling constant for the relevant transitions has a magnitude $g/2\pi = 3.1$ MHz, and the cavity-field decay rate κ and dipole decay rate of the atom γ are $(\kappa, \gamma)/2\pi = (1.25, 3.0)$ MHz. The atom flux through the cavity is so low (about two atoms per millisecond) that the probability of having two atoms during the transit time of 35 μs is negligible. Atoms are illuminated by laser pulses from the side, all polarized linearly along the cavity axis. Preparation of the initial state is achieved by optical pumping with two lasers, one resonant with the transition from $F = 2$ to $F' = 2$, the other coupling levels $F = 1$ and $F' = 2$. Both lasers, applied simultaneously for 2.8 μs, have constant Rabi frequencies of $\Omega/2\pi = 35$ MHz. Failure of the optical pumping does not reduce the measured entanglement fidelity, because an atom in a wrong initial state can only emit a photon in either the first or the second pulse, but not in both. Entangling and mapping laser pulses have a $\sin^2(\pi t/t_P)$ time dependence, with $t_P = 1.1$ μs. The peak Rabi frequency of the entangling pulse is $\Omega/2\pi = 24$ MHz. Because the mapping laser is resonant with the cavity, its peak Rabi frequency is chosen to be lower ($\Omega/2\pi = 9$ MHz) to avoid off-resonant (via $F' = 0$) repeated excitation of the atom. As a result, after detecting a first photon we observe a second photon in the

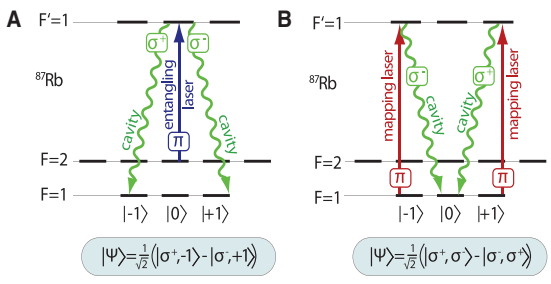

Fig. 1. Entanglement and state mapping. Together with the cavity, laser pulses drive vacuum-stimulated Raman adiabatic passages, first (**A**) creating an entanglement between the atom and the emitted photon, and then (**B**) mapping the atomic state onto the polarization state of a second photon. Entanglement is then shared between two flying photons, with the atom disentangled.

[1]Max-Planck-Institut für Quantenoptik, Hans-Kopfermann-Strasse 1, D-85748 Garching, Germany. [2]Clarendon Laboratory, University of Oxford, Parks Road, Oxford OX1 3PU, UK.

*To whom correspondence should be addressed. E-mail: gerhard.rempe@mpq.mpg.de

same pulse with a probability of only 0.6%. Entangling and mapping pulses are separated from each other by an adjustable time interval, t_S, so detected photons can clearly be assigned to the first or the second laser pulse. Figure 2B displays the pulse sequence and the measured photon arrival-time distribution. From a Hanbury Brown and Twiss measurement, we infer that the efficiency for generating a photon during the entangling (mapping) pulse conditioned on the detection of a photon during the previous entangling pulse is 14.8% (8.8%) (*15*), resulting in a 1.3% success probability for generating an entangled photon pair. This includes the random position of the atom and, hence, the random atom-cavity coupling constant, as well as imperfect state preparation.

Photons emitted from the cavity are circularly polarized, but for technical reasons we rotate them into the linear horizontal/vertical (H/V) basis before sending them through a single-mode optical fiber to the detection area. The detection efficiency for a photon emitted from the cavity is 31%. To perform a full quantum state tomography, the photons are measured in several different bases, selected by using different settings of half- and quarter-wave plates (*16*, *17*). Because the photons are created in the same spatial mode, a nonpolarizing beam splitter (NPBS) is used to direct the photons randomly to one of two measurement setups. This allows each photon to be detected in either the H/V, circular right/left (R/L), or linear diagonal/antidiagonal (D/A) basis.

Photons are produced and detected one after the other. This allows probing of the coherence of the atomic superposition state after the creation of entanglement. Applying a constant magnetic field, B, along the cavity axis shifts the atomic states $|+1\rangle$ and $|-1\rangle$ by an amount $-\Delta$ and $+\Delta$, respectively, with $\Delta = 2\pi \times 0.7$ MHz/G. Our scheme then generates photons with frequencies linked to their polarizations. Specifically, σ^- photons have higher frequencies than σ^+ photons. This has no consequence for the time evolution of the entangled state, Eq. 1, because both parts of the superposition state have the same energy. A frequency-insensitive detection of the first photon with, e.g., right circular polarization $|R\rangle \equiv \frac{1}{\sqrt{2}}(|H\rangle + i|V\rangle)$ after the fiber, however, projects the atomic state into a superposition of $|+1\rangle$ and $|-1\rangle$ with equal amplitudes. The energy difference between the atomic levels then leads to a different time evolution of the two states, resulting in

$$|\psi_{\text{atom}}(t)\rangle = \frac{1}{\sqrt{2}}(e^{i\Delta t}|+1\rangle - ie^{-i\Delta t}|-1\rangle) \quad (3)$$

Subsequent state mapping transfers this state into the photonic state

$$|\psi_{\text{photon 2}}(t)\rangle = \frac{1}{\sqrt{2}}(e^{i\Delta t}|\sigma^+\rangle - ie^{-i\Delta t}|\sigma^-\rangle) \quad (4)$$

which continues rotating until the second photon is detected. The total rotation angle, given by the time difference between the two photon detections, depends on the separation, t_S, between entangling and mapping pulses and the duration of the photon wave packet. Alternatively, for a given time separation, t_S, the time evolution can be controlled by the magnetic-field strength. This state rotation could be suppressed by appropriately delaying the first photon and considering only simultaneous photon-detection events.

To measure the rotation of the atomic state, we observed both photons in the R/L basis, after rotating them from σ^+/σ^- to H/V. We define a contrast $V \equiv P_{|RL\rangle} - P_{|LL\rangle} - P_{|RR\rangle} + P_{|LR\rangle}$, with $P_{|LL\rangle}$ the probability of detecting both photons as left circular polarized (and analogous for $P_{|RR\rangle}$, etc.). For the state given in Eq. 4, one expects a $\cos(2\Delta t_S)$ dependence. Figure 3 shows the measured contrast as a function of the magnetic field for fixed t_S = 2.8 μs. The oscillatory behavior is a manifestation of the phase rotating at twice the Larmor frequency. For increasing field magnitude, the envelope of the oscillation decreases. This is due to the long photon wave packets produced in our scheme (Fig. 2B). As a result, the time interval between two photon detections covers a range of possible values, and thus the superposition state can evolve by differing amounts during this time.

The density matrix of the entangled state given in Eq. 2 is obtained from a full quantum state tomography for $B = 0$ and t_S = 1.3 μs. In this case, no time evolution occurs between the two photon detections. Figure 4A shows the real part of the density matrix reconstructed from the two-photon Stokes parameters, determined by measuring two-photon events in the four detec-

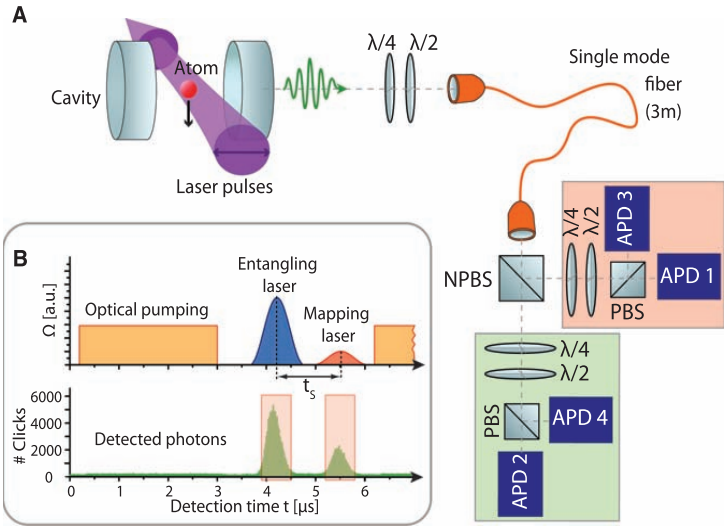

Fig. 2. Scheme of the experiment. (**A**) Laser-cooled atoms traversing the cavity are illuminated with laser pulses. Behind the cavity, the polarization of the emitted σ^+/σ^- photons is rotated to linear horizontal/vertical. Photons are then directed toward two detection setups for measurements in different polarization bases. Detection occurs with avalanche photodiodes (APDs). (**B**) Laser-pulse sequence and photon arrival-time distribution. The photon wave-packets duration is about 300 ns. The displayed time windows are used in the evaluation.

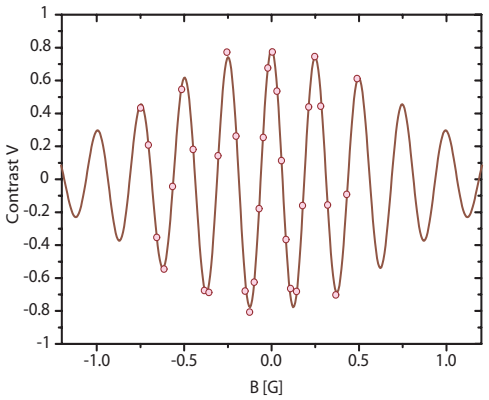

Fig. 3. Atomic state rotation. After detecting the first photon in the R/L basis (behind the fiber), the atom is projected into a superposition state that is time dependent when a magnetic field along the cavity axis is applied (here, t_S = 2.8 μs). Displayed is the contrast, V, as a function of the magnetic field, B. A cosine with a Gaussian envelope fits the data well.

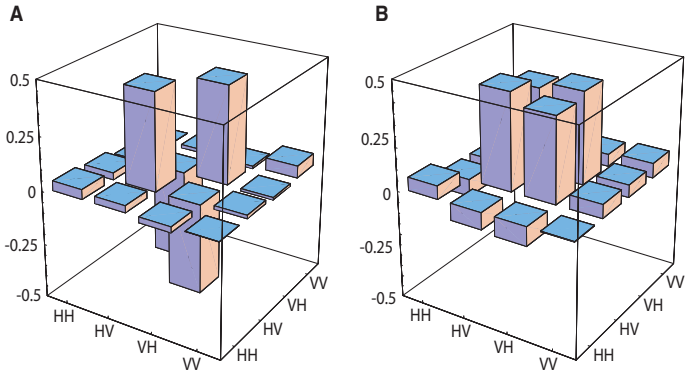

Fig. 4. Quantum state tomography. **(A)** Real part of the reconstructed density matrix for $B = 0$ and $t_S = 1.3$ μs. All imaginary parts (not shown) have a magnitude smaller than 0.03. Fidelity with the $|\Psi^-\rangle$ Bell state is 86.0(4)%. About 2200 entanglement events were collected for each of nine measurement settings. **(B)** For $B = -0.13$ G and $t_S = 2.8$ μs, the atomic superposition state rotates by π. The observed data correspond to a $|\Psi^+\rangle$ Bell state, with fidelity of 82.9(6)%. About 1800 entanglement events were obtained for each of six measurement settings. All imaginary parts (not shown) have a magnitude smaller than 0.05. In (A) and (B), equal detection efficiencies for all detectors were assumed.

tors (*17*). The resulting density matrix has only positive eigenvalues, and hence it represents a physically possible state. Its fidelity with respect to the expected Bell state, $|\Psi^-\rangle$ from Eq. 2, is $F = 86.0(4)\%$, with $0.5 < F \leq 1$ proving entanglement (*18*). From the density matrix, following (*16*), we derive a concurrence of $C = 0.73(7)$, with $0 < C \leq 1$ also proving entanglement. Because of technical imperfections, e.g., of polarizers in the detection setups, the observed fidelity/concurrence sets a lower bound for both the atom-photon and photon-photon entanglement achieved. The same measurements were done for $B = -0.13$ G and $t_S = 2.8$ μs for which the atomic superposition state accumulates a π phase shift (compare to Fig. 3). Therefore, a density matrix corresponding to the Bell state $|\Psi^+\rangle \equiv \frac{1}{\sqrt{2}}(|+1,\sigma^-\rangle + |-1,\sigma^+\rangle)$ is expected. This is indeed observed (Fig. 4B) with a fidelity of $F = 82.9(6)\%$ and a concurrence of $C = 0.72(13)$. The state evolves between the two photon detections as a result of the constant magnetic field.

Future experiments could produce a time-independent $|\Psi^+\rangle$ Bell state by applying a pulsed magnetic field to the atom between entanglement generation and state mapping. Moreover, partial driving of the Raman transition in combination with atomic state manipulation should allow production of highly entangled multiphoton states (*12*). Our technique applied to a quasi-permanently trapped intracavity atom (*3*, *19*) will push the probability of success even further, making the scheme truly deterministic. Two (or more) such systems operated in parallel are perfectly suited for teleportation and entanglement experiments in a quantum network (*20*–*22*) or quantum gate operations in a distributed and, hence, scalable quantum computer (*23*, *24*).

References and Notes

1. E. Knill, R. Laflamme, G. J. Milburn, *Nature* **409**, 46 (2001).
2. A. Kuhn, M. Hennrich, G. Rempe, *Phys. Rev. Lett.* **89**, 067901 (2002).
3. J. McKeever *et al.*, *Science* **303**, 1992 (2004).
4. M. Keller, B. Lange, K. Hayasaka, W. Lange, H. Walther, *Nature* **431**, 1075 (2004).
5. M. Hijlkema *et al.*, *Nat. Phys.* **3**, 253 (2007).
6. T. Wilk, S. C. Webster, H. P. Specht, G. Rempe, A. Kuhn, *Phys. Rev. Lett.* **98**, 063601 (2007).
7. J. I. Cirac, P. Zoller, H. J. Kimble, H. Mabuchi, *Phys. Rev. Lett.* **78**, 3221 (1997).
8. H.-J. Briegel, W. Dür, J. I. Cirac, P. Zoller, *Phys. Rev. Lett.* **81**, 5932 (1998).
9. B. B. Blinov, D. L. Moehring, L.-M. Duan, C. Monroe, *Nature* **428**, 153 (2004).
10. B. Darquié *et al.*, *Science* **309**, 454 (2005).
11. J. Volz *et al.*, *Phys. Rev. Lett.* **96**, 030404 (2006).
12. C. Schön, E. Solano, F. Verstraete, J. I. Cirac, M. M. Wolf, *Phys. Rev. Lett.* **95**, 110503 (2005).
13. J. M. Raimond, M. Brune, S. Haroche, *Rev. Mod. Phys.* **73**, 565 (2001).
14. M. Hennrich, T. Legero, A. Kuhn, G. Rempe, *Phys. Rev. Lett.* **85**, 4872 (2000).
15. M. Hennrich, T. Legero, A. Kuhn, G. Rempe, *N.J. Phys.* **6**, 86 (2004).
16. D. F. V. James, P. G. Kwiat, W. J. Munro, A. G. White, *Phys. Rev. A.* **64**, 052312 (2001).
17. J. B. Altepeter, E. R. Jeffrey, P. G. Kwiat, *Adv. At. Mol. Opt. Phys.* **52**, 105 (2005).
18. C. A. Sackett *et al.*, *Nature* **404**, 256 (2000).
19. S. Nußmann *et al.*, *Nat. Phys.* **1**, 122 (2005).
20. S. Bose, P. L. Knight, M. B. Plenio, V. Vedral, *Phys. Rev. Lett.* **83**, 5158 (1999).
21. L.-M. Duan, H. J. Kimble, *Phys. Rev. Lett.* **90**, 253601 (2003).
22. D. E. Browne, M. B. Plenio, S. F. Huelga, *Phys. Rev. Lett.* **91**, 067901 (2003).
23. Y. L. Lim, A. Beige, L. C. Kwek, *Phys. Rev. Lett.* **95**, 030505 (2005).
24. A. Serafini, S. Mancini, S. Bose, *Phys. Rev. Lett.* **96**, 010503 (2006).
25. We thank J. Bochmann and N. Kiesel for helpful discussions. This work was supported by the Deutsche Forschungsgemeinschaft [Collaborative Research Center 631, Research Unit 635, Munich Center for Advanced Photonics (MAP)] and the European Union [Information Society Technologies (SCALA) and Research Training Network (CONQUEST) programs].

16 April 2007; accepted 7 June 2007
Published online 21 June 2007;
10.1126/science.1143835
Include this information when citing this paper.

Porous Semiconducting Gels and Aerogels from Chalcogenide Clusters

Santanu Bag,[1,2] Pantelis N. Trikalitis,[2]* Peter J. Chupas,[3] Gerasimos S. Armatas,[1,2] Mercouri G. Kanatzidis[1,2,4]†

Inorganic porous materials are being developed for use as molecular sieves, ion exchangers, and catalysts, but most are oxides. We show that various sulfide and selenide clusters, when bound to metal ions, yield gels having porous frameworks. These gels are transformed to aerogels after supercritical drying with carbon dioxide. The aerogels have high internal surface area (up to 327 square meters per gram) and broad pore size distribution, depending on the precursors used. The pores of these sulfide and selenide materials preferentially absorb heavy metals. These materials have narrow energy gaps (between 0.2 and 2.0 electron volts) and low densities, and they may be useful in optoelectronics, as photocatalysts, or in the removal of heavy metals from water.

Inorganic porous materials are at the foundation of broad applications such as molecular sieves, ion exchangers, and catalysts (*1*, *2*). Zeolites and aluminosilicate mesoporous materials constitute the vast majority of this class. Aerogels are another kind of porous inorganic amorphous polymer in which nanosized blocks are interconnected to yield high internal surface area, very low densities, and large open pores (*3*, *4*). Although the sol-gel chemistry of oxide-based materials (e.g., SiO_2, Al_2O_3, TiO_2) and carbon (*5*) is well known, successful attempts to apply this approach to non–oxide-based systems are quite rare, especially for chalcogenides. Such systems would be capable of combining the electronic properties of chalco-

[1]Department of Chemistry, Northwestern University, Evanston, IL 60208, USA. [2]Department of Chemistry, Michigan State University, East Lansing, MI 48824, USA. [3]Advanced Photon Source, Argonne National Laboratory, Argonne, IL 60439, USA. [4]Materials Science Division, Argonne National Laboratory, Argonne, IL 60439, USA.

*Present address: Department of Chemistry, University of Crete, Heraklion 71409, Greece.
†To whom correspondence should be addressed. E-mail: m-kanatzidis@northwestern.edu

PRL 99, 063001 (2007) PHYSICAL REVIEW LETTERS week ending 10 AUGUST 2007

Trapping of Neutral Rubidium with a Macroscopic Three-Phase Electric Trap

T. Rieger, P. Windpassinger,* S. A. Rangwala,† G. Rempe, and P. W. H. Pinkse
Max-Planck-Institut für Quantenoptik, Hans-Kopfermann-Strasse 1, D-85748 Garching, Germany
(Received 6 March 2007; published 6 August 2007)

We trap neutral ground-state rubidium atoms in a macroscopic trap based on purely electric fields. For this, three electrostatic field configurations are alternated in a periodic manner. The rubidium is precooled in a magneto-optical trap, transferred into a magnetic trap, and then translated into the electric trap. The electric trap consists of six rod-shaped electrodes in cubic arrangement, giving ample optical access. Up to 10^5 atoms have been trapped with an initial temperature of around 20 microkelvin in the three-phase electric trap. The observations are in good agreement with detailed numerical simulations.

DOI: 10.1103/PhysRevLett.99.063001 PACS numbers: 32.80.Pj, 32.60.+i, 39.25.+k

Trapping is essential in many modern experiments in physics. A trap allows the interaction time of the trapped species with other particles or fields to be greatly extended. Trapping enabled breakthrough experiments with ions, atoms, and molecules. Each newly demonstrated trap paved the way for new classes of experiments. Thus far, electric traps for neutral polarizable particles have received relatively little attention. They have first been proposed for excited (Rydberg) atoms [1] and, later, for ground-state atoms [2,3]. Ground-state particles lower their energy in electric fields. Hence these particles are attracted by high fields ("high-field seekers"). Since Maxwell's equations do not allow the creation of an electrostatic maximum in free space, time-dependent (pseudoelectrostatic or "ac") fields are required for trapping, a principle well known from ion traps. Only recently, two-dimensional [4] and three-dimensional [5] versions of ac traps have been demonstrated with cold polar molecules having a large and linear Stark shift. For polar molecules, these traps offer the advantage of a deep trapping potential, which can trap both low- and high-field seeking states. Using laser-cooled strontium atoms, the Katori group has demonstrated a chip version of an ac electric trap with the motivation of performing precision spectroscopy for metrology [6].

In this Letter we report on an experiment where laser-cooled rubidium atoms are trapped in a macroscopic ac electric trap. This result opens the perspective of confining cold molecules and atoms in the same spatial region for the purpose of using the optically cooled atoms as a coolant for the molecules. For this, a large volume of several mm^3, ample optical access, and a relatively deep effective potential depth are essential. The geometry of our trap is in essence the one proposed in [2,3] with rectangular driving. Our trap is a three-phase trap; i.e., a full cycle of its operation can be divided in three different phases. The three-phase trap offers cubic symmetry rather than the cylindrical one of three-dimensional two-phase traps [7]. Therefore, the average restoring force is isotropic about the trap center [8].

Our trap is depicted in Fig. 1. It consists of three pairs of electrodes in a cubic arrangement. Trapping is achieved by alternating the electric field configuration in a cyclic manner with driving frequency f. The phase of the driving field is $\phi = 2\pi t/T \bmod 2\pi$, with t the time and $T = 1/f$ the period. At each point of time, only two opposing electrodes are given large voltages of opposite sign; the other four electrodes are grounded. This leads to an electric field of which the absolute value $|E|$ has the shape of a saddle, increasing towards the two charged electrodes and decreasing in the two perpendicular directions. In the following we first focus on the field near the trap center. Assuming that in the first phase of the driving cycle the electrodes in the x direction are charged, the electric field strength can here be approximated in second order in the spatial coordinates by

$$|E| = E_0 + bx^2 - \tfrac{1}{2}b(y^2 + z^2), \qquad 0 \le \phi < 2\pi/3, \quad (1)$$

where in our experiment $E_0 = 30.4$ kV/cm and $b = 19.8$ kV/cm/mm^2 are coefficients found from the full numerical field calculation [9] with the x electrodes at ± 7 kV. Atoms experience a quadratic Stark shift in this field: $W_S = -\frac{1}{2}\alpha|E|^2$, where α is the atom's static polar-

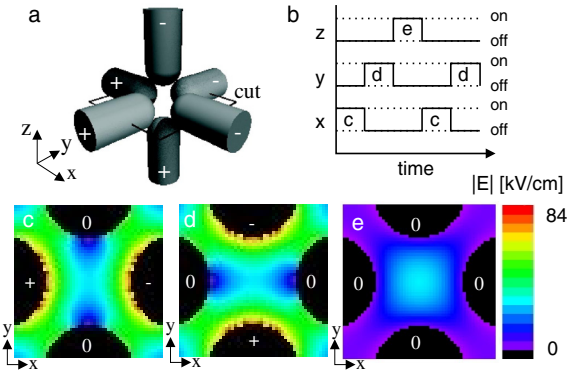

FIG. 1 (color online). The ac electric trap. (a) The 6 electrodes. (b) The switching diagram, indicating that in each full cycle each pair of electrodes is switched on for one third of the time. (c)–(e) The absolute value of the electric field in the x-y plane in the three consecutive phases of a full driving cycle with electrodes at ± 7 kV.

PRL 99, 063001 (2007) PHYSICAL REVIEW LETTERS week ending 10 AUGUST 2007

izability [10]. Because of the gradients in $|E|$, the field exerts a force $\mathbf{F} = -\nabla W_S$ on the atoms. This force pushes the atoms towards the high electric fields near the surfaces of the charged electrodes. This defocuses the atom cloud in the x direction during $0 \leq \phi < 2\pi/3$. At the same time, the atoms are focused in the y and z direction. In the second phase of the trap cycle ($2\pi/3 \leq \phi < 4\pi/3$), the pair of electrodes in the y direction is charged while simultaneously the x and z pair are grounded. Now the y direction is defocusing, whereas the x and z direction are focusing. In the third and last phase ($4\pi/3 \leq \phi < 6\pi/3$), the focusing and defocusing directions are permutated once more. With the additional approximation that $\mathbf{F} = \alpha|E|\nabla|E| \approx \alpha E_0 \nabla|E|$, the force on an atom at a given point in space averages to zero in a full cycle. However, under the influence of the periodic driving the atom moves and the average force over a full cycle is finite and directed to the trap center. Assuming the drive frequency is high enough, the motion can be divided in two parts: the cyclic motion locked to the driving field is called the micromotion; the motion under influence of the average force is called the secular motion. For large drive frequencies one can average over the micromotion to find the average restoring force yielding the secular motion. For a driving frequency below a certain cutoff value, the micromotion becomes unstable; the atoms hit the electrodes and are lost.

The equations of motion derived from $\mathbf{F} \approx \alpha E_0 \nabla|E|$ with $|E|$ from Eq. (1) can be solved analytically [2,3]. From a stability analysis, analytic expressions for the cutoff frequency are found. For atoms, which have a quadratic Stark shift, the cutoff frequency is linear in the applied voltage. For high f, the trap depth decreases with $1/f^2$, so the maximum depth is obtained for frequencies just above the cutoff, and its position, f_{peak}, is also expected to scale linear in the applied voltage.

From previous studies [4] we know that the regions away from the center, where there are no known analytic solutions of the equations of motion, play an important role. Therefore, extensive Monte Carlo simulations were performed to study the performance of the trap in detail. In these simulations, the Newtonian equations of motion are solved for typically 10^4 particles for a single parameter setting. All parameters in the simulation are fixed by the experiment. For the electric field in the simulation, the exact three-dimensional calculation was used [9].

Our experimental realization of the trap has titanium electrodes mounted on a clawlike ceramic mount. The diameter of the electrode rods is 3 mm, which is also the distance between opposing electrodes. The radius of curvature of the half-spherical endings is 1.5 mm. The electrodes can be charged to ± 7 kV in a time shorter than a microsecond. The (four) diagonals through the trap offer free sight with a diameter of 1.9 mm. The trap is oriented such as to allow for three optional orthogonal optical paths parallel and perpendicular to the horizontal plane. Along these three axes, the free view is 1.4 mm. Because of the tilted mounting, gravity is pointing in the (-0.67, -0.67, -0.33) direction of the Cartesian coordinate system coinciding with the axes of the electrodes.

The electric trap is loaded with laser-cooled ^{85}Rb atoms. The atoms are captured from a dispenser in a magneto-optical trap (MOT) placed at a horizontal distance of 2 cm from the center of the electric trap. As measured by absorption imaging, 2×10^7 atoms are captured here. Before transferring the atoms to a magnetic trap, they are cooled by optical molasses [11] to a temperature of ≈ 15 μK in 7 ms and optically pumped to the $F = 3$, $m_F = 3$ Zeeman state. The magnetic trap is generated by two water-cooled coils with 48 windings which are rated to hold 75 A for 3 seconds. The coils are mounted on a translation stage. By moving the coils, the magnetic field minimum and the atoms are translated [12]. After bringing the atoms in approximately 0.8 s into the center of the electric trap, the magnetic trap is switched off in 25 μs and the electric trap is switched on 100 μs later. To determine the initial conditions of the atoms before the start of the electric trap, we kept the atoms at the position of the MOT and measured the cloud to contain 6×10^6 atoms and to have a temperature of 62 μK. In a separate experiment, it was tested that moving the magnetic trap causes no significant heating or losses.

A number of different measurements were performed to characterize the electric trap: the dependence of the number of trapped atoms on time, drive frequency, and electrode voltage was studied and is discussed in the following. The number of particles remaining in the electric trap after 50 ms was measured by absorption imaging. The results are depicted in Fig. 2 as a function of the drive frequency. There is a sharp cutoff near 120 Hz. Just above the cutoff, the maximum number of atoms is trapped. As expected, the frequency of the maximum, f_{peak}, scales linearly in the applied voltage (see the insert of Fig. 2). In the limit of high frequencies, the micromotion becomes smaller and faster and the net force towards the trap center vanishes. Therefore, the trap depth, and hence the number of particles, falls off quickly with f. The simulation describes the position and the shape of the trapping peak very well. The absolute fraction of trapped atoms is very sensitive to temperature, size, and position of the initial atomic cloud. Nevertheless, this fraction obtained from the simulation agrees with the measurement within a factor of 2. For trapping times below 50 ms, the atom number as a function of driving frequency shows more complex structures (not shown), both in the simulation and in the experiment, which is attributed to atoms which are released from the magnetic trap into unstable orbits of the electric trap.

The number of remaining atoms as a function of time is plotted in Fig. 3. The atoms escaping the trap from unstable orbits causes the loss which is observed for times shorter than 50 ms. The simulation predicts this rapid initial loss. It

PRL 99, 063001 (2007) PHYSICAL REVIEW LETTERS week ending 10 AUGUST 2007

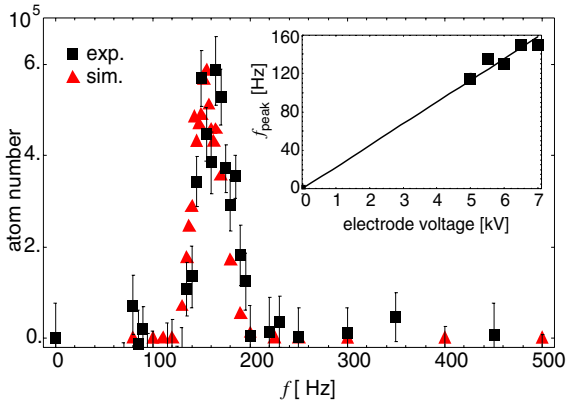

FIG. 2 (color online). The frequency dependence of the trapped number of atoms after 50 ms for electrodes at ±7 kV. The square symbols are data; the triangles are the result of a Monte Carlo simulation. Noise in the background images can lead to negative values. The simulation result is scaled to fit the height of the data. The inset shows the measured dependence of the frequency of the maximum f_{peak} as a function of the electrode voltage. The expected linear dependence is indicated by the line.

also predicts stable trapping after 50–80 ms. The observed signal, however, falls off with a time constant of 0.36 s. The pressure in the UHV chamber is in the 10^{-10} mbar range during MOT operation, which is too good to explain this loss. However, during operation of the electric trap, significant pressure rises are observed by a remote pressure gauge. Also, the lifetime in the magnetic trap just outside the electrodes is observed to go down from almost 2 s to the few 100 ms regime when high voltage is applied. From this and other observations we deduce that gas, probably Rb absorbed on the electrodes, is ejected from the electrodes once they are charged up, locally increasing the pressure and limiting the lifetime of trapped atoms. Therefore, we are confident that the observed decay is due to collisions with hot background atoms released from the electrodes.

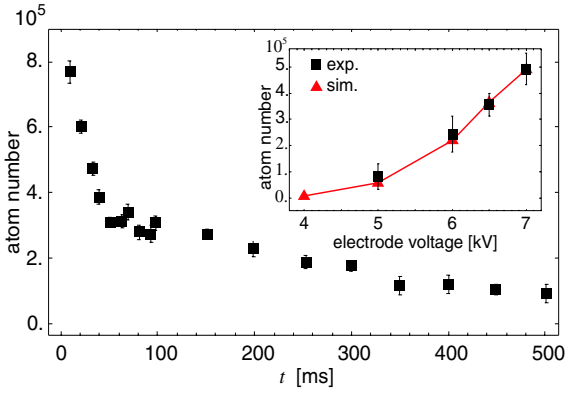

FIG. 3 (color online). Remaining number of atoms as a function of time. At $t = 0$ the magnetic trap contains 2.7×10^6 atoms. The initial rapid decay is caused by atoms which enter the electric trap on nontrapped orbits, either because they are too hot or because their motion has the wrong phase. The decay of the trapped atoms, visible as the long tail with a $1/e$ time of 0.36 s, is attributed to collisions with background gas. The inset shows, for another set of data with other starting conditions, the dependence of the maximum number of trapped atoms after 50 ms electric trapping as a function of the applied voltage. The line is a guide to the eye.

The maximum number of trapped atoms depends not only on the drive frequency and time but also on the applied voltages. In the inset in Fig. 3, the number of atoms in the maximum is plotted as a function of the applied voltages. Again, the simulation describes the results well. Below 4 kV, trapping is no longer possible due to the gravitational force exceeding the cycle-averaged electric trapping force.

Absorption imaging of the trapped cloud allows additional insight into its dynamics. Images spanning more than a full cycle of the ac trap are depicted in Fig. 4. The atom cloud is ellipsoidal, but the ellipticity varies periodically in time. This is caused by the periodic motion of the individual atoms, making the cloud pulsate. To demon-

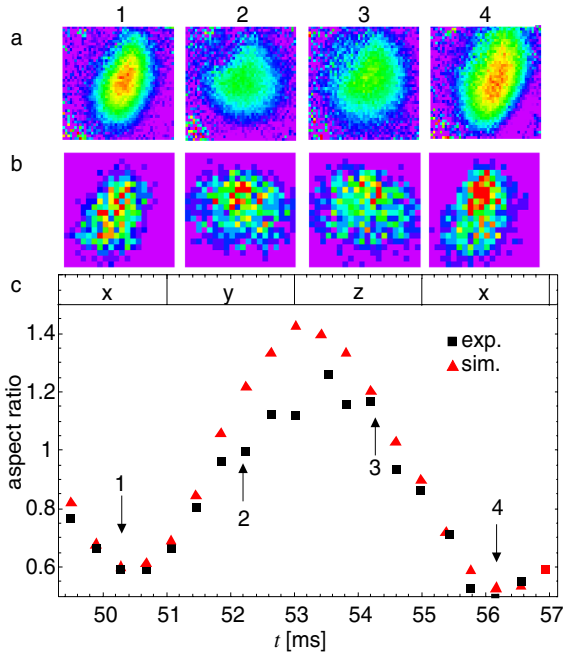

FIG. 4 (color online). (a) Measured and (b) simulated camera pictures of the trapped cloud at the times indicated 1, 2, 3, 4 in (c). Each picture in (a) is an average over 10 measurements. The 19.5° tilt with respect to the vertical corresponds to the tilt angle of the trap mounting. (c) Measured (squares) and simulated (triangles) aspect ratio of the elliptic clouds. The boxes with letters x, y, z, x indicate the charged electrodes. Note that the simulation has no free parameters.

strate the correspondence between the simulation and the measurements, we calculate the ellipticity of the measured and simulated clouds by projection onto their two major axes. From this the aspect ratio is calculated and plotted in Fig. 4(c). The agreement is very good; the remaining differences are attributed to imaging imperfections. Note the difference in the minimum ellipticity at 50.5 and 56 ms, which is predicted by the simulation and caused by a residual vertical oscillation of the cloud under the influence of gravity with a longer periodicity.

As a final characterization of the trap, its depth and the temperature of the trapped cloud should be discussed. From expansion data, temperatures of the trapped cloud can be obtained. However, the expansion of the cloud is dominated by the velocities of the micromotion, which remain constant in the falling frame of reference when the electric fields are switched off. The ellipticity observed in Fig. 4 already indicates that the expansion will be anisotropic. Indeed, different temperatures are measured depending on the phase when the trap is switched off. At a driving frequency of 170 Hz and release from the electric trap after 21 ms, temperatures of 63 μK and 122 μK were measured in two orthogonal directions. One could argue, however, that these numbers are not good measures for the trap depth. More relevant is the depth of the effective potential, which in the harmonic limit is obtained by averaging over the micromotion. Here the simulation is again of help; it allows us to extract the *initial* velocity distribution of those atoms which remain trapped in stable orbits. For a cloud of an initial size of 0.3 mm, this distribution corresponds to 20 μK. We use this number as a definition of the effective trap depth.

There are two natural ways to improve the system. The lifetime could be extended by improving the background pressure during operation of the electric trap. The MOT could be placed further away from the electric trap or even in a separate, differentially pumped, chamber. A second improvement concerns gravity. The simulations show that without gravity, the trap depth is approximately doubled. This implies that significantly more particles could be trapped by compensating for gravity. This can, in principle, be achieved by applying asymmetric voltages on the electrodes, shifting the saddle point of the electric field up, causing a net electric force to outbalance gravity. This is more straightforward when the trap is rotated such that one of the electrode pairs is oriented vertically.

In principle, simultaneous trapping of atoms and molecules in our trap is possible, enabling ultracold collision studies once sufficiently high densities and sufficiently long trapping times are achieved. Simultaneous trapping should work for molecules like H_2O or D_2O which have, firstly, a quadratic Stark shift [13] and, secondly, several thermally populated states with a similar polarizability over mass ratio as ^{85}Rb. Other alkalis and higher-order stability islands could also be exploited. Another possibility is to overlay a magnetostatic trap for atoms with a tens of mK deep electrodynamic trap for molecules with a large Stark shift. Since optimal switching frequencies for such molecules are in the kHz range [4,5], these fields will only make a very weak potential for the atoms. Hence, sympathetic cooling of cold molecules by laser-cooled atoms might be possible. Other applications of our setup are trapping of atoms or molecules in Rydberg states and the study of atom-atom interaction at ultralow temperatures by electric fields [14] or combined electric and magnetic fields [15].

We thank S. Nußmann for help with the experiment. We acknowledge financial support by the Deutsche Forschungsgemeinschaft (SPP 1116, cluster of excellence Munich Centre for Advanced Photonics).

Note added.—During the final preparation stages of this manuscript, similar results were reported elsewhere [16].

*Present address: QUANTOP, Niels Bohr Institute, DK-2100 Copenhagen, Denmark.

†Present address: Raman Research Institute, C. V. Raman Avenue, Sadashivanagar, Bangalore 560080, India.

[1] W. H. Wing, Phys. Rev. Lett. **45**, 631 (1980).

[2] F. Shimizu and M. Morinaga, Jpn. J. Appl. Phys. **31**, L1721 (1992).

[3] M. Morinaga and F. Shimizu, Laser Phys. **4**, 412 (1994).

[4] T. Junglen, T. Rieger, S. A. Rangwala, P. W. H. Pinkse, and G. Rempe, Phys. Rev. Lett. **92**, 223001 (2004).

[5] J. van Veldhoven, H. L. Bethlem, and G. Meijer, Phys. Rev. Lett. **94**, 083001 (2005); H. L. Bethlem, J. van Veldhoven, M. Schnell, and G. Meijer, Phys. Rev. A **74**, 063403 (2006).

[6] T. Kishimoto, H. Hachisu, J. Fujiki, K. Nagato, M. Yasuda, and H. Katori, Phys. Rev. Lett. **96**, 123001 (2006).

[7] E. Peik, Eur. Phys. J. D **6**, 179 (1999).

[8] R. F. Wuerker, H. M. Goldenberg, and R. V. Langmuir, J. Appl. Phys. **30**, 441 (1959).

[9] Calculated with the software package SIMION.

[10] For Rb, $\alpha = 79.4\ \mathrm{kHz}/(\mathrm{kV}/\mathrm{cm})^2$; *CRC Handbook of Chemistry*, edited by David R. Lide (CRC Press, Boca Raton, 2004–2005), 85th ed.

[11] P. D. Lett, W. D. Phillips, S. L. Rolston, C. E. Tanner, R. N. Watts, and C. I. Westbrook, J. Opt. Soc. Am. B **6**, 2084 (1989).

[12] H. J. Lewandowski, D. M. Harber, D. L. Whitaker, and E. A. Cornell, J. Low Temp. Phys. **132**, 309 (2003).

[13] T. Rieger, T. Junglen, S. A. Rangwala, G. Rempe, P. W. H. Pinkse, and J. Bulthuis, Phys. Rev. A **73**, 061402(R) (2006).

[14] M. Marinescu and L. You, Phys. Rev. Lett. **81**, 4596 (1998).

[15] R. Krems, Int. Rev. Phys. Chem. **24**, 99 (2005); B. Marcelis, B. J. Verhaar, and S. J. J. M. F. Kokkelmans (private communication).

[16] S. Schlunk, A. Marian, P. Geng, A. P. Mosk, G. Meijer, and W. Schöllkopf, Phys. Rev. Lett. **98**, 223002 (2007).

PRL 99, 073001 (2007) PHYSICAL REVIEW LETTERS week ending 17 AUGUST 2007

Cavity Cooling of Internal Molecular Motion

Giovanna Morigi,[1] Pepijn W. H. Pinkse,[2] Markus Kowalewski,[3] and Regina de Vivie-Riedle[3]

[1]*Departament de Fisica, Universitat Autonoma de Barcelona, E-08193 Bellaterra, Spain*
[2]*Max-Planck-Institut für Quantenoptik, Hans-Kopfermannstr. 1, D-85748 Garching, Germany*
[3]*Department of Chemistry, Ludwig-Maximilian-Universität München, Butenandtstr. 11, D-81377 München, Germany*

(Received 19 March 2007; published 13 August 2007)

We predict that it is possible to cool rotational, vibrational, and translational degrees of freedom of molecules by coupling a molecular dipole transition to an optical cavity. The dynamics is numerically simulated for a realistic set of experimental parameters using OH molecules. The results show that the translational motion is cooled to a few μK and the internal state is prepared in one of the two ground states of the two decoupled rotational ladders in a few seconds. Shorter cooling times are expected for molecules with larger polarizability.

DOI: 10.1103/PhysRevLett.99.073001 PACS numbers: 33.80.Ps, 32.80.Lg, 42.50.Pq

The preparation of molecular samples at ultralow temperatures offers exciting perspectives in physics and chemistry [1]. This goal is presently pursued by several groups worldwide with various approaches. Two methods for generating ultracold molecules employ photoassociation and Feshbach resonances, and are efficiently implemented on alkali dimers [1]. Another approach uses buffer gases, to which the molecules thermalize [2]. Its application is limited by the physical properties of atom-molecule collisions at low temperatures. Optical cooling of molecules is an interesting alternative, but, contrary to atoms, its efficiency is severely limited by the multiple scattering channels coupled by spontaneous emission, and may only be feasible for molecules which are confined in external traps for very long times [3]. Elegant laser-cooling proposals, based on optical pumping the rovibrational states [4,5] and excitation pulses tailored with optimal control theory [6,7], exhibit efficiencies which are indeed severely limited by spontaneous decay. In [8,9] it was argued that cooling of the molecular external motion could be achieved by using resonators, by enhancing stimulated photon emission into the cavity mode over spontaneous decay. This mechanism was successfully applied for cooling the motion of atoms [10].

In this Letter we propose a method for optically cooling external as well as the *internal* degrees of freedom of molecules. The method relies on the enhancement of the anti-Stokes Raman transitions through the resonant coupling with the modes of a high-finesse resonator, as sketched in Fig. 1. All relevant anti-Stokes transitions are driven by sequential tuning of the driving laser. At the end of the process the molecule is in the rovibrational ground state and the motion is cooled to the cavity linewidth. We demonstrate the method with *ab initio* based numerical simulations using OH radicals, of which cold ensembles are experimentally produced [11,12].

We now outline the theoretical considerations. We consider a gas of molecules of mass M, prepared in the electronic ground state X, and with dipole transitions $X \rightarrow E$. Here, E is a set of electronically excited states, including higher-lying states which may contribute significantly to the total polarizability. We denote the rovibrational states and their corresponding frequencies by $|j, \xi\rangle$ and $\omega_\xi^{(j)}$ $(j = X, A, \ldots)$, while the elements of the dipole moment $\mathbf{d}$ are $\mathcal{D}_{\xi\to\xi''} = \langle A \in E, \xi''|\mathbf{d}|X, \xi\rangle$. These transitions are driven by a far-off resonant laser and interact with an optical resonator as illustrated in Fig. 1(a). In absence of the resonator, spontaneous Raman scattering determines the relevant dynamics of molecule-photon interactions. These processes depend on the center-of-mass momentum $\mathbf{p}$ through the Doppler effect and occur at rate $\Gamma^{(\gamma)}_{\xi\to\xi'}(\mathbf{p}) = \sum_{E,\xi''}\Gamma_{\xi''\to\xi'}\gamma_{E,\xi\to\xi''}(\mathbf{p})$, where $\Gamma_{\xi''\to\xi'}$ the decay rate along the transition $|A, \xi''\rangle \rightarrow |X, \xi'\rangle$, and

$$\gamma_{E,\xi\to\xi''}(\mathbf{p}) = \frac{\Omega^2_{L,\xi\to\xi''}}{(\Delta^E_{\xi,\xi''} + \mathbf{k_L}\cdot\mathbf{p}/M)^2 + \Gamma^2_{\xi''}/4}, \quad (1)$$

with $\Gamma_{\xi''} = \sum_{\xi'}\Gamma_{\xi''\to\xi'}$. Here, $\Omega_{L,\xi\to\xi''} = \mathcal{E}_L(\mathcal{D}_{\xi\to\xi''}\cdot\epsilon_L)/\hbar$ gives the strength of coupling to the laser with electric field amplitude $\mathcal{E}_L$, polarization ϵ_L, frequency ω_L, and wave vector $\mathbf{k_L}$, and $\Delta^E_{\xi,\xi''} = \omega^{(X)}_\xi - \omega^{(E)}_{\xi''} + \omega_L$ denotes the detuning between laser and internal transition.

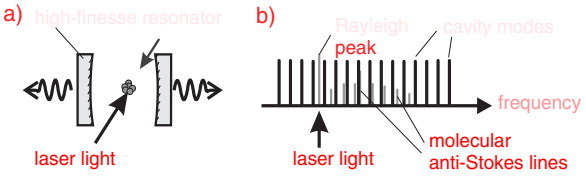

FIG. 1. (a) A molecular sample interacts with the cavity field and is driven by a laser, inducing Raman transitions cooling the internal and external degrees of freedom. (b) Comb of resonances at which photon emission into the cavity is enhanced. The gray bars symbolize the molecular lines, which in OH extend over several tens of nanometers. The laser frequency (arrow) is varied to sequentially address several anti-Stokes lines.

PRL 99, 073001 (2007) PHYSICAL REVIEW LETTERS week ending 17 AUGUST 2007

In the limit where the laser is far-off resonant from the electric dipole transitions, electronic ground states at different rovibrational quantum numbers are coupled via Raman transitions. The corresponding emission spectrum is symbolized by the gray bars in Fig. 1(b). In this regime, coupling an optical resonator to the molecule may enhance one or more scattering processes when the corresponding molecular transitions are resonant with resonator modes, symbolized by the black bars in Fig. 1(b). This enhancement requires that the rate $\Gamma^{\kappa}_{\xi\to\xi'}(\mathbf{p})$, describing scattering of a photon from the laser into the cavity mode, and its subsequent loss from the cavity, exceeds the corresponding spontaneous Raman scattering rate, $\Gamma^{\kappa}_{\xi\to\xi'}(\mathbf{p}) \gg \Gamma^{\gamma}_{\xi\to\xi'}(\mathbf{p})$. For a standing wave cavity, in the regime where the molecular kinetic energy exceeds the cavity potential, and when the cavity photon is not reabsorbed but lost via cavity decay [9], we have $\Gamma^{\kappa}_{\xi\to\xi'}(\mathbf{p}) = \Gamma^{\kappa,+}_{\xi\to\xi'}(\mathbf{p}) + \Gamma^{\kappa,-}_{\xi\to\xi'}(\mathbf{p})$, where the sign $\pm$ gives the direction of emission along the cavity axis and

$$\Gamma^{\kappa,\pm}_{\xi\to\xi'}(\mathbf{p}) = 2\kappa \sum_{c,E,\xi''} \frac{\gamma_{E,\xi\to\xi''}(\mathbf{p})|g^{\pm}_{c,\xi''\to\xi'}|^2}{(\delta\omega \pm \mathbf{k_c}\cdot\mathbf{p}/M)^2 + \kappa^2}. \quad (2)$$

Here, 2κ is the cavity linewidth, $\delta\omega = \omega^{(X)}_{\xi} - \omega^{(X)}_{\xi'} + \omega_L - \Omega_c$ is the frequency difference between the initial and final (internal and cavity) state, with Ω_c the frequencies of the cavity modes, and $g^{\pm}_{c,\xi'\to\xi''}$ are the Fourier components at cavity-mode wave vector $\pm|\mathbf{k_c}|$ of the coupling strength to the empty cavity mode, $g_{c,\xi'\to\xi''}(\mathbf{x}) = \mathcal{E}_c(\mathbf{x})(\boldsymbol{\epsilon}_0\cdot\mathcal{D}_{\xi',\xi''})/\hbar$, with $\mathcal{E}_c$ and $\boldsymbol{\epsilon}_0$ the vacuum amplitude and polarization. Note that reabsorption and spontaneous emission of the cavity photon can be neglected while $\kappa \gg |g_{c,\xi'\to\xi''}\Omega_{L,\xi\to\xi''}/\Delta^{E}_{\xi,\xi''}|$.

Enhancement of *Rayleigh* scattering into the cavity is achieved by setting the laser on resonance with one cavity mode, $\omega_L = \Omega_c$, see Fig. 1(b), provided that $\Gamma^{\gamma}_{\xi\to\xi} \ll \Gamma^{\kappa}_{\xi\to\xi}$, i.e., $g^2_{c,\xi\to\xi}/\Gamma\kappa \gg 1$, where Γ is determined by the linewidths of the excited states which significantly contribute to the scattering process. This situation has been discussed in [9], where it has been predicted that the motion can be cavity cooled to a temperature which is in principle only limited by the cavity linewidth [13], provided that the laser is set on the low-frequency side of the cavity resonance. Note that cooling of the motion in the plane orthogonal to the cavity axis is warranted when the laser is a standing wave field, which is simply found in our model by allowing for the absorption of laser photons at wave vector $-\mathbf{k_L}$. In general, enhancement of scattering along the Raman transition $\xi \to \xi'$, decreasing the energy of the rovibrational degrees of freedom, is achieved by setting the laser such that the corresponding anti-Stokes spectral line is resonant with one cavity mode, and requires $g^2_{c,\xi\to\xi'}/\Gamma\kappa \gg 1$. The cooling strategy then consists of choosing a suitable cavity and of sequentially changing the laser frequency, so as to maximize the resonant drive of the different anti-Stokes spectral lines, and thereby cooling the molecule to the rovibrational ground state.

We simulate the cooling dynamics for OH radicals using a rate equation based on the rates (1) and (2). The considered Raman process is detuned from the excitation energy of 32 402 cm^{-1} (971.4 THz) between the $X^2\Pi_i$ ground state and the electronically excited state $A^2\Sigma^+$ as indicated in Fig. 2(b). The relevant rovibrational spectrum and the coupling of the molecule to the laser field and cavity modes were obtained by combining *ab initio* calculations for the vibronic degrees of freedom with available experimental data for the rotational constants. The level scheme is displayed in Fig. 2(b). The potential energy surfaces (PES) and the polarizabilities were calculated with highly correlated quantum chemical methods: the electronic structure calculations [14] were performed on the multiconfigurational self consistent field (MCSCF) level using a single atom basis set (aug-cc-pVTZ). Rates (1) and (2) were evaluated using the polarizability tensors, defined as $\alpha_{\xi\to\xi'} = \sum_{\xi''}\mathcal{D}_{\xi\to\xi''}\mathcal{D}_{\xi''\to\xi'}/\hbar\Delta_{\xi''}$ [15] and calculated with linear response theory at the MCSCF level [16–18]. In order to determine the internal level structure and transition strengths, the vibrational eigenvalues and eigenfunctions were evaluated with a relaxation method using propagation in imaginary time plus an additional diagonalization step [19]. The corresponding Placzek-Teller coefficients [20] were calculated for the transitions between the rotational sublevels.

In order to obtain a concise picture of the cooling dynamics, several assumptions were made without loss of generality. The molecules are prepared in the lower-lying $X^2\Pi_{3/2}$ component of the $X^2\Pi$ electronic ground state.

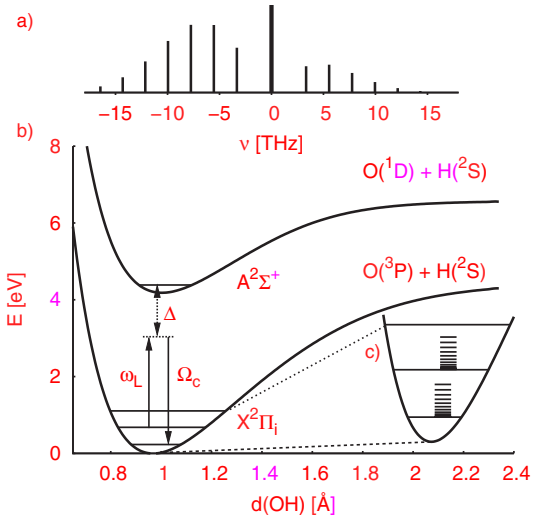

FIG. 2. (a) Simulated Raman spectra for the first nine rotational states of OH, which are relevantly occupied at room temperature. (b) Potential energy surfaces of the $X^2\Pi_i$ ground state and of the $A^2\Sigma^+$ excited state. The coherent Raman process is indicated by the arrows. (c) Rovibrational substructure.

PRL 99, 073001 (2007) PHYSICAL REVIEW LETTERS week ending 17 AUGUST 2007

The hyperfine splitting is neglected as angular momentum conservation for the rotational Raman transitions inhibits transitions between the hyperfine sublevels. At $T \approx 300$ K only the first 9 rotational states of OH are relevantly occupied, while only the vibrational ground state is populated. The selection rule $\Delta J = 0, \pm 2$ for the rotational transitions yields that the matrix elements of transitions between rotational states with opposite parity vanish, resulting in two separate ladders for the scattering processes with final states $|X, v = 0, J = 0, 1\rangle$ [21]. We assume that a preparation step has occurred, bringing the motional temperature to below 1 K. This could be realized with, e.g., helium-buffer-gas cooling [2], electrostatic filtering [22], or decelerator techniques [23,24]. The high-finesse optical cavity has a free-spectral range (FSR) of $15 \times 2\pi$ GHz, which can be realized with a Fabry-Perot-type cavity of length $L = 1$ cm. For simplicity we assume that the cavity only supports zeroth-order transverse modes. This actually underestimates the possibilities of scattering light into the cavity, since higher-order transverse modes can be combined in degenerate cavities, like confocal resonators. The cavity half-linewidth is set to $\kappa = 75 \times 2\pi$ kHz, and the coupling $g_{c,0\to0} = 2\pi \times 116$ kHz. This is achieved with a mode volume of 3.2×10^{-13} m^3, assuming a mode waist of $w_0 = 6$ μm, and a cavity finesse $F = 10^5$, i.e., a mirror reflectivity of 0.999 969. We also choose a laser wavelength of 532 nm, for which ample power is available as well as mirrors of the required quality. The frequency of the laser is far below that of the OH A-X rovibronic band. We assume to have single-frequency light of 10 W enhanced by a factor of 100 by a buildup cavity in a TEM_{00} mode, corresponding to a Rabi coupling $\Omega_{L,0\to0} = 2\pi \times 69$ GHz and frequency $\omega_L = \omega_0^{(A)} - \omega_0^{(X)} - \Delta$ with $\Delta \approx 2\pi \times 407$ THz. The latter value is sequentially varied during cooling, in order to drive (quasi-)resonantly the cooling transitions. In combination with the broad spectrum of cavity modes, the laser only needs to be varied over one FSR to address all anti-Stokes lines. Figure 3 displays the anti-Stokes Raman lines as a function of the frequency modulus the FSR. Addressing the Stokes lines (not drawn) can be avoided, given the small laser and cavity linewidths. In a confocal cavity, e.g., all higher-order transverse cavity modes will be degenerate with fundamental ones. In addition, our scheme is robust against a small number of coincidences between Stokes and anti-Stokes lines.

The cooling strategy is as follows. First, the external degrees of freedom are cooled to the cavity linewidth, corresponding to a final temperature $T \approx 4$ μK, by setting the Rayleigh transition quasiresonant with one cavity mode. The corresponding coefficients have been evaluated numerically, giving the rate of Rayleigh scattering for OH into the cavity $\Gamma^{\kappa}_{0\to0} \sim 1$ kHz, while the spontaneous rate $\Gamma^{\gamma}_{\xi\to\xi} \sim 0.5$–$2.5$ Hz. We verified the efficiency of cooling by solving the semiclassical equation for the mechanical energy [25]. For these parameters, starting from $T \sim 1$ K

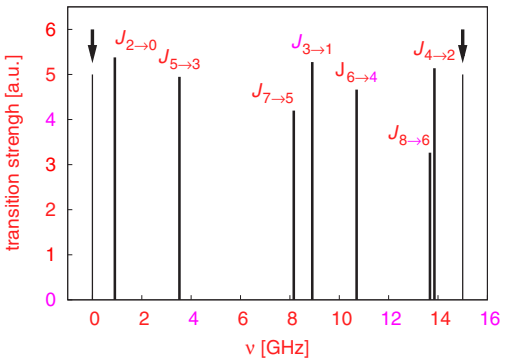

FIG. 3. Reduced spectrum of the relevant rotational anti-Stokes transitions: the lines are projected onto a single free-spectral range of the cavity, whose width is indicated by the arrows. The unfolded Raman spectrum spans 15 THz or up to 10^3 cavity modes. The frequencies of the lines are evaluated from quantum chemical calculations, and must be understood as a qualitative picture; high-resolution experimental input is needed to fix the absolute position with kHz accuracy.

for the external degrees of freedom, the cooling limit is reached in a time of the order of 1 s. Then, the rotational degrees of freedom are cooled by setting the laser frequency to sequentially address each anti-Stokes spectral line. A manually optimized sequence led to the result in Fig. 4, where the mean rotational quantum number $\langle J \rangle$ is plotted as a function of time. The final value $\langle J \rangle \approx 0.5$ corresponds to the final situation in which the two states $J = 0$ and $J = 1$, ground states of each ladder, achieve maximum occupation, equal to 50%. The insets in Fig. 4 show that after 0.3 s their occupation is about 40%, while after 1.8 s it reaches 49% (leading to a total population of 98.8%). The cooling rate for the rotational degrees of freedom of OH is of the order of 4 Hz, see Fig. 4, while the rate of heating due to spontaneous Raman scattering along the Stokes transitions is about 0.1 Hz. In the simu-

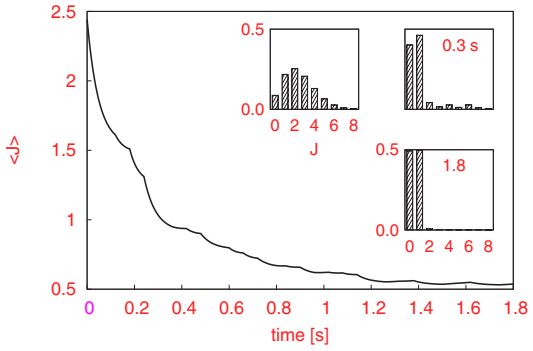

FIG. 4. Mean rotational quantum number versus time during the cooling process. The manually optimized cooling sequence first empties the levels $J = (2, 3)$, thereafter higher levels are addressed. The small figures show the state distributions at time 0, 0.3, and 1.8 s. The cavity length is fine-tuned to address the $J_{2\to0}$ and the $J_{3\to1}$ transition simultaneously.

lation the vibrational degrees of freedom are taken into account but no vibrational heating is observed. In a separate simulation, we checked that vibrational excitations are cooled with the same scheme.

The cooling time can be improved significantly for molecules with higher polarizabilities α, as the cooling rate scales with α^2. For instance, the polarizability of NO is approximately 4 times larger than for OH, and preliminary results show that it indeed cools down faster, although the cooling time is not reduced by a factor 16 because more rotational states are occupied at 300 K. For molecules like Cs_2, α is 2 orders of magnitude larger than for OH, and should yield faster cooling rates.

For molecules with low polarizability, like OH, reduction of the cooling time seems possible by further optimizing the sequential procedure. In addition, the efficiency could be improved by using degenerate cavity modes or by superradiant enhancement of light scattering, sustained by the formation of self-organized molecular crystals [26].

In summary, we presented a strategy for cooling external and internal degrees of freedom of a molecule. We simulated the cooling dynamics for OH using experimentally accessible parameter regimes, showing that this method allows for efficient preparation in the lowest rovibrational states, while the motion is cooled to the cavity linewidth. For OH the cooling time is of the order of seconds, and requires thus the support of trapping technologies which are stable over these times [2,3,27–29]. The cooling time of molecules with larger polarizabilities can scale down to a few ms, when the polarizability is about 10 times larger. Applications of this technique to polyatomic molecules has to deal with an increasing number of transitions to be addressed, which will slow down the process. A possible extension of this scheme could make use of excitation pulses, determined with optimal control techniques [7].

G. M. thanks the Theoretical Femtochemistry Group at LMU for the hospitality. Support by the European Commission (CONQUEST, No. MRTN-CT-2003-505089, EMALI, No. MRTN-CT-2006-035369), the Spanish MEC (Ramon-y-Cajal, Consolider Ingenio 2010 "QOIT", HA2005-0001), EUROQUAM (Cavity-Mediated Molecular Cooling), and the DFG cluster of excellence Munich Centre for Advanced Photonics, is acknowledged.

[1] See J. Doyle, B. Friedrich, R. V. Krems, and F. Masnou-Seeuws, Eur. Phys. J. D **31**, 149 (2004), and references therein.
[2] J. D. Weinstein, R. deCarvalho, T. Guillet, B. Friedrich, and J. M. Doyle, Nature (London) **395**, 148 (1998).
[3] M. Drewsen, A. Mortensen, R. Martinussen, P. Staanum, and J. L. Sørensen, Phys. Rev. Lett. **93**, 243201 (2004); P. Blythe, B. Roth, U. Fröhlich, H. Wenz, and S. Schiller, Phys. Rev. Lett. **95**, 183002 (2005).
[4] J. T. Bahns, W. C. Stwalley, and P. L. Gould, J. Chem. Phys. **104**, 9689 (1996).
[5] I. S. Vogelius, L. B. Madsen, and M. Drewsen, Phys. Rev. A **70**, 053412 (2004).
[6] P. W. Brumer and M. Shapiro, *Principles of Quantum Control of Molecular processes* (Wiley VCH, New York, 2003).
[7] D. J. Tannor and A. Bartana, J. Chem. Phys. A **103**, 10 359 (1999).
[8] P. Horak, G. Hechenblaikner, K. M. Gheri, H. Stecher, and H. Ritsch, Phys. Rev. Lett. **79**, 4974 (1997).
[9] V. Vuletić and S. Chu, Phys. Rev. Lett. **84**, 3787 (2000).
[10] P. Maunz, T. Puppe, I. Schuster, N. Syassen, P. W. H. Pinkse, and G. Rempe, Nature (London) **428**, 50 (2004).
[11] S. Y. T. van de Meerakker, P. H. M. Smeets, N. Vanhaecke, R. T. Jongma, and G. Meijer, Phys. Rev. Lett. **94**, 023004 (2005).
[12] J. R. Bochinski, E. R. Hudson, H. J. Lewandowski, and J. Ye, Phys. Rev. A **70**, 043410 (2004).
[13] P. Domokos and H. Ritsch, J. Opt. Soc. Am. B **20**, 1098 (2003).
[14] MOLPRO, version 2006.1, a package of *ab initio* programs, H.-J. Werner, P. J. Knowles, R. Lindh, F. R. Manby, M. Schütz, and others; see http://www.molpro.net.
[15] Convergency of the polarizability was checked by basis set enlargement. The obtained spontaneous emission rate $\Gamma = 2\pi \times 310$ kHz ($\tau = 514$ ns) for $A^2\Sigma^+$ is comparable to the value 685 ns; see J. Luque and D. R. Crosley, J. Chem. Phys. **109**, 439 (1998).
[16] J. Olsen and P. Jørgensen, J. Chem. Phys. **82**, 3235 (1985).
[17] P. Jørgensen, H. J. Aa. Jensen, and J. Olsen, J. Chem. Phys. **89**, 3654 (1988).
[18] DALTON, a molecular electronic structure program, Release 2.0 (2005); see http://www.kjemi.uio.no/software/dalton/dalton.html.
[19] K. Sundermann and R. de Vivie-Riedle, J. Chem. Phys. **110**, 1896 (1999).
[20] R. Gaufres and S. Sportouch, J. Mol. Spectrosc. **39**, 527 (1971).
[21] The anharmonicity in the vibrational ladder is included in the *ab initio* PES, the rovibrational coupling enters as $B(v)J(J+1) - D_j J^2(J+1)^2$, with $B_e = 18.871$ cm^{-1} and $\omega_e = 3735.21$ cm^{-1}; see K. P. Huber and G. Herzberg, *Molecular Spectra and Molecular Structure-IV. Constants of Diatomic Molecules* (Van Nostrand Reinhold, New York, 1979).
[22] S. A. Rangwala, T. Junglen, T. Rieger, P. W. H. Pinkse, and G. Rempe, Phys. Rev. A **67**, 043406 (2003).
[23] H. L. Bethlem, G. Berden, and G. Meijer, Phys. Rev. Lett. **83**, 1558 (1999).
[24] R. Fulton, A. I. Bishop, M. N. Shneider, and P. F. Barker, Nature Phys. **2**, 465 (2006).
[25] S. Stenholm, Rev. Mod. Phys. **58**, 699 (1986).
[26] P. Domokos and H. Ritsch, Phys. Rev. Lett. **89**, 253003 (2002); V. Vuletić, H. W. Chan, and A. T. Black, Phys. Rev. A **64**, 033405 (2001).
[27] H. L. Bethlem, G. Berden, F. M. H. Crompvoets, R. T. Jongma, A. J. A. van Roij, and G. Meijer, Nature (London) **406**, 491 (2000).
[28] D. DeMille, D. R. Glenn, and J. Petricka, Eur. Phys. J. D **31**, 375 (2004).
[29] T. Rieger, T. Junglen, S. A. Rangwala, P. W. H. Pinkse, and G. Rempe, Phys. Rev. Lett. **95**, 173002 (2005).

LETTERS

Nonlinear spectroscopy of photons bound to one atom

I. SCHUSTER, A. KUBANEK, A. FUHRMANEK, T. PUPPE, P. W. H. PINKSE, K. MURR AND G. REMPE*

Max-Planck-Institut für Quantenoptik, Hans-Kopfermann-Straße 1, D-85748 Garching, Germany

*e-mail: gerhard.rempe@mpq.mpg.de

Published online: 13 April 2008; doi:10.1038/nphys940

Optical nonlinearities typically require macroscopic media, thereby making their implementation at the quantum level an outstanding challenge. Here, we demonstrate a nonlinearity for one atom enclosed by two highly reflecting mirrors[1]. We send laser light through the input mirror and record the light from the output mirror of the cavity. For weak laser intensity, we find the vacuum-Rabi resonances[2–11]. But for higher intensities, we observe an extra resonance[12], which originates from the fact that the cavity can accommodate only an integer number of photons and that this photon number determines the characteristic frequencies of the coupled atom–cavity system[13–15]. We selectively excite such a frequency by depositing two photons at once into the system and find a transmission that increases with the laser intensity squared. The nonlinearity differs from classical saturation nonlinearities[16–19] and is direct spectroscopic proof of the quantum nature of the atom–cavity system. It provides a photon–photon interaction by means of one atom, and constitutes a step towards a two-photon gateway or a single-photon transistor[20].

The quantum nonlinearity has its origin in the fact that under the condition of strong coupling, a system composed of a single atom and a single cavity mode has properties that are distinctively different from those of the bare atom (without the cavity), or the bare cavity (without the atom), or just the sum of the two (Fig. 1a). In fact, the composite system forms a new quantum entity, the so-called atom–cavity molecule, made of matter and light, with its own characteristic energy spectrum. This spectrum consists of an infinite ladder of pairs of states, the dressed states (Fig. 1b). The first doublet contains one quantum of energy and can be probed by laser spectroscopy. For weak probing, the resulting spectrum is independent of the laser intensity and has been dubbed the vacuum-Rabi or normal-mode spectrum, consisting of a pair of resonances symmetrically split around the bare atomic and cavity resonances. This spectrum was first observed with atomic beams[1], and has been explored recently with single dipole-trapped atoms[2–4]. It constitutes a benchmark for strong atom–cavity coupling and is central to most cavity quantum electrodynamics (QED) experiments, including those outside atomic physics[5–11]. Note that the normal-mode spectrum on its own can equally well be described classically, by linear dispersion theory or a coupled oscillator model (atomic dipole and cavity field).

The next-higher-lying doublet contains two quanta of energy and lacks a classical explanation[12,21,22]. The corresponding dressed states have been observed (together with a few higher-order states) in microwave cavity QED[13–15] and even ion trapping, where phonons play the role of photons[23]. At optical frequencies, evidence for these states has indirectly been obtained in two-photon correlation experiments where the conditional response of the system on detection of an emitted photon is monitored[16,24–26]. These optical experiments observe the quantum fluctuations in dissipative cavity QED systems but operate away from a resonance to a higher-lying state. Direct spectroscopy using a two-colour technique to excite the second doublet step-wise has been attempted in a pioneering experiment with atomic beams[22]. An unambiguous signature of these states remained elusive owing to large fluctuations in the number of atoms traversing the cavity.

Using single trapped atoms, we exploit the anharmonicity of the energy-level spectrum to drive a multiphoton transition directly from the vacuum state to a specific higher-lying state. We observe the quantum character of our cavity QED field by measuring a photon flux, not a photon correlation. To explain our technique, we note that a two-state atom coupled to a single-mode light field has a discrete spectrum consisting of a ladder of dressed states, $|n+1,\mp\rangle$, with frequencies

$$\omega_{n+1,\mp} = n\omega_c + \frac{1}{2}(\omega_a+\omega_c) \mp \frac{1}{2}\sqrt{4g^2(n+1)+(\omega_a-\omega_c)^2} \quad (1)$$

and a ground state $|g,0\rangle$ with zero energy (atom with ground state $|g\rangle$ and mode in the vacuum state $|0\rangle$). Here, $n=0,1,2,\ldots$ is the principal quantum number of the mode (to be distinguished from the mean photon number), g is the atom–cavity coupling strength and ω_a and ω_c are the frequencies of the atom and the cavity, respectively. The frequencies of the coupled system are probed with monochromatic light of frequency ω_L (ref. 12). Resonances occur when $(n+1)\omega_L = \omega_{n+1,\mp}$. In Fig. 1c, these resonance conditions are plotted in the frame (Δ_a, Δ_c) where $\Delta_a = \omega_L - \omega_a$ and $\Delta_c = \omega_L - \omega_c$ are the atom and cavity detunings, respectively.

We now notice that if each laser photon is resonant with the atom, $\omega_L = \omega_a$ $(\Delta_a = 0)$, it is detuned from the single-photon resonances, $\omega_L \neq \omega_{1,\mp}$, and this for any value of the cavity frequency ω_c. Scanning the cavity frequency (vertical arrow in Fig. 1c) around the frequency of a weak laser therefore gives a suppressed and largely frequency-independent response, as further discussed in connection with Fig. 3. When increasing the laser intensity, however, two-photon transitions can occur at $\Delta_c = \mp g$, where two laser photons together are resonantly absorbed by the combined system and the second manifold of dressed states is populated for $2\omega_L = \omega_{2\mp}$. We keep the intensity at low enough values such that the atomic transition is never saturated. In this way, we rule out the possibility of nonlinearities due to a classical behaviour of the intracavity field[17]. This protocol of driving multiphoton transitions by avoiding the normal modes as well as atomic saturation is new and should in principle apply to other cavity QED systems. It can be interpreted as a two-photon gateway: single photons

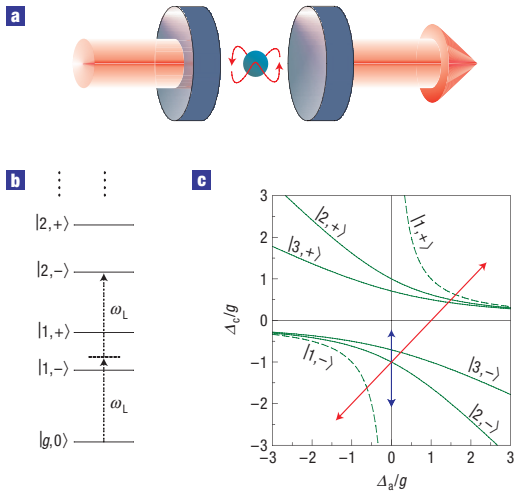

Figure 1 The atom–cavity molecule. a, Artist's conception of an atom enclosed by two cavity mirrors. The coupling of the atom to the intracavity light is so strong that the energy spectrum of the composite atom–cavity 'molecule' radically differs from the spectrum of its components. **b**, Schematic diagram of such a level structure illustrating how the dressed state $|2,-\rangle$ is directly accessed from the vacuum through a two-photon transition. **c**, Location of the classical (normal-mode) resonances (dashed curves) and the first two quantum resonances (states $|2,\mp\rangle$ and $|3,\mp\rangle$) (solid curves). The diagonal arrow is the scan direction shown in Fig. 2, which crosses all resonances. A vertical scan along $\Delta_a = 0$, as in Fig. 3, avoids the classical resonances. Resonances for the manifold $(n+1)$ are located at $\Delta_c = \pm g/\sqrt{n}$ for $\Delta_a = 0$.

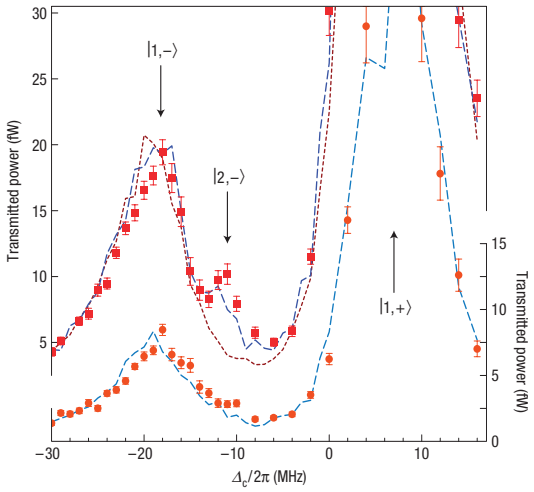

Figure 2 Quantum anharmonicity of the atom–cavity system. Transmitted power as a function of cavity detuning Δ_c for the input powers 0.5 pW (circles, right scale) and 1.5 pW (squares, left scale). In this and all following figures, 10 fW corresponds to about 0.01 intracavity photons, the error bars are s.d. and an offset of 0.5 fW due to detector dark counts has been removed from the data. The two peaks at $2\pi \times (-18, 7)$ MHz represent the two normal modes, which are reproduced by a theory considering only single-photon transitions (short-dashed line). Note that the maximum of the right peak is beyond the scale of the figure. The quantization of the intracavity light (long-dashed lines) is required to explain the appearance of the two-photon resonance at $-2\pi \times 11$ MHz at higher intensity.

cannot be accepted by the combined atom–cavity system, but two photons can.

Our implementation of a strongly coupled atom–cavity system consists of single ^{85}Rb atoms localized inside the mode of a high-finesse optical cavity by means of an auxiliary intracavity red-detuned dipole trap at 785 nm. We carry out spectroscopy on the system by shining near-resonant probe light at 780 nm onto the input mirror and recording the light exiting from the output mirror. While probing the system, we also monitor the localization of the atom. We then post-select only the events for which the condition of strong coupling was fulfilled. For sufficient statistics, we average over many trapping events (see Supplementary Information, Methods).

In a first experiment, the cavity transmission is monitored for an atom–cavity detuning $\Delta_a - \Delta_c \approx g$. For these parameters, the normal-mode spectrum becomes asymmetric and the splitting between states $|1,-\rangle$ and $|2,-\rangle$ increases compared with the case $\Delta_a \approx \Delta_c$. This has the advantage that this two-photon resonance is well separated from the normal modes even for moderate atom–cavity coupling constants. Figure 2 shows two scans with different probe laser intensities along the diagonal arrow in Fig. 1c. Both scans show the normal modes, but the higher-intensity scan shows a pronounced extra resonance.

The quantum anharmonicity[14] of the energy-level structure reveals itself in the position of the two-photon resonance relative to the normal modes, which is in excellent agreement with equation (1) for a coupling of $g = 2\pi \times 11.2$ MHz and a Stark-shifted atom–cavity detuning of $2\pi \times 10.5$ MHz. These values indicate that the coupling is about 70% of the maximally possible value $g_0 = 2\pi \times 16$ MHz at an antinode, and that the trap induces an average Stark shift of $2\pi \times 24.5$ MHz which also corresponds to about 70% of the Stark shift at an antinode of the standing-wave dipole trap (the trap depth is 170 nW and the bare atom–cavity detuning is preset to $2\pi \times 35$ MHz). Ideal couplings are not reached owing to two reasons: first, the atom performs an oscillation in the dipole trap wells; second, the position of the trapping wells shifts with respect to the antinodes of the probe light along the cavity axis as the distance from the cavity centre increases; therefore, atoms that are trapped slightly off the cavity centre are not maximally coupled.

Next, we carried out extensive numerical simulations to compare the measured spectrum with several cavity QED models[12]. The simulations closely imitate the experiment, starting from the trapping of single, slow atoms which are injected into the intracavity dipole trap, following up with the measurement protocol which is executed until the atom leaves the trap, and culminating in the same evaluation procedure (see Supplementary Information, Discussion). The first set of simulations (only shown for the higher-intensity scan, short-dashed line in Fig. 2) assumes at most one quantum of energy in the system, thereby enabling us to quantify the contribution due to single-photon transitions. We see that, whereas the normal-mode resonances are reproduced, there is a large deviation to the measured data precisely at the position of the two-photon resonance. In contrast, another set of simulations (long-dashed lines) was carried out for a quantized cavity mode with three Fock states, $|0\rangle, |1\rangle, |2\rangle$. Apart from the normal modes, these simulations also reproduce the two-photon resonance.

In a second experiment, we explore the quantum regime by scanning the cavity along the vertical arrow in Fig. 1c, using a bare atom–probe detuning of $2\pi \times 21$ MHz and dipole trap power of 140 nW. Figure 3 shows four scans with different probe

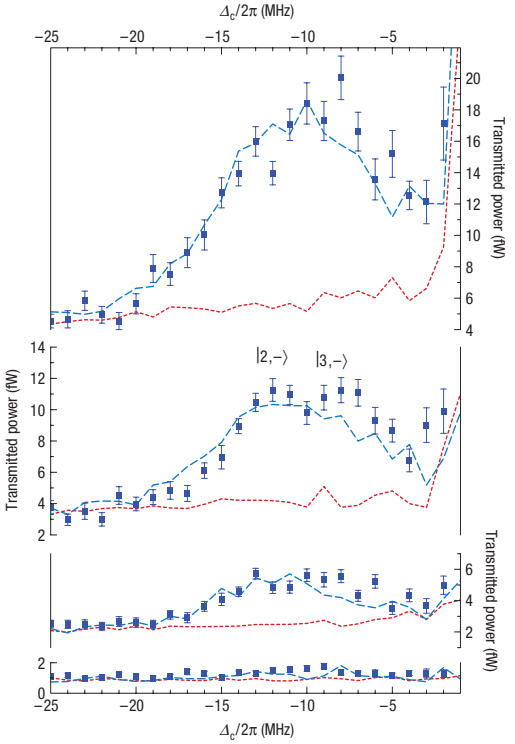

Figure 3 Multiphoton resonances and suppression of single-photon resonances. Transmitted power as a function of cavity detuning Δ_c for input powers of 0.5, 1.5, 2.4 and 3.3 pW (from bottom to top, data points). The simulations with single-photon (short-dashed lines) and multiphoton transitions (long-dashed lines), with the respective positions of the dressed states $|2,-\rangle$ and $|3,-\rangle$ are also shown.

laser intensities. The lowest-intensity scan (bottom panel) shows a largely flat signal, in agreement with our idea of avoiding the normal modes. Here, the photonic state is close to the vacuum state, with a mean intracavity photon number as low as 0.001. All higher-intensity scans, however, show a pronounced extra resonance. The deviation between the off-resonance signal, $\Delta_c/2\pi \leq -20$ MHz, and the on-resonance signal, $-15\,\text{MHz} \leq \Delta_c/2\pi \leq -5$ MHz, gets larger with increasing intensity. Here, we find that a simulation with at most one quantum of excitation (short-dashed lines) continues to predict a signal with no major modification in the structure, whereas the resonance is globally reproduced with simulations taking into account field quantization. We had to account for four Fock states, indicating that the resonance stems from a two-photon and a weak but rising three-photon transition, the latter transition contributing to broaden the resonance. We also notice an increase in the transmitted intensity at small cavity detunings $|\Delta_c|/2\pi \leq 3$ MHz. This is a systematic effect originating from the bare cavity resonance occurring at $\Delta_c = 0$ with a linewidth of $\kappa = 2\pi \times 1.25$ MHz, which could not be completely suppressed in the post-selection process (see Supplementary Information, Discussion and references therein).

Under coherent excitation, we expect a mainly quadratic scaling of the transmitted intensity at the frequency of the two-photon resonance and a linear scaling off resonance, that is, at large cavity detunings $|\Delta_c| \gg g$, where all theories

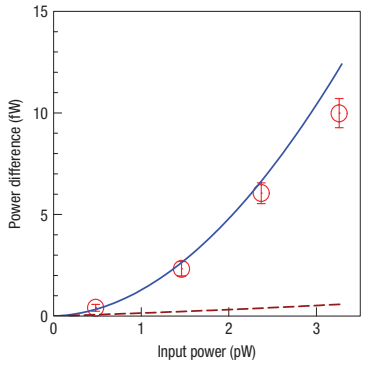

Figure 4 Nonlinear intensity response. Difference between the nonlinear response on the two-photon resonance and the linear single-photon response, together with the prediction from a quantum theory with an immobile atom (solid line). For reference, we also show the nonlinearity expected from the saturation of a two-state atom coupled to a classical field (optical bistability theory, dashed line).

coincide. To evaluate the quantum response of the system, the data used for Fig. 3 are averaged over the two-photon region ($-15\,\text{MHz} \leq \Delta_c/2\pi \leq -10$ MHz) as well as over the off-resonance region ($-25\,\text{MHz} \leq \Delta_c/2\pi \leq -20$ MHz), for each input intensity. The off-resonant region serves as a reference for the linear single-photon contribution. By taking the difference between the two regions, we isolate the contribution of the two-photon transition, and find a mainly quadratic response of the transmitted intensity versus the input intensity (Fig. 4, circles).

We proceed by comparing the data with a model that assumes the atom to be immobile. This model describes an ideal quantum system, with a well-defined coupling to the mode, as would be desirable for future applications. To this end, we match all of the spectra of Fig. 3 to this idealized theory with a common set of parameters (g, Δ_a), and find good agreement for $(g, \Delta_a) = 2\pi \times (11.5, 1)$ MHz (see Supplementary Information, Fig. S3). Note that the coupling g is close to the value obtained for the independent measurements in Fig. 2, whereas the atomic detuning Δ_a is close to zero. The theory spectra are then evaluated in the same way as the measured spectra to obtain the intensity response of the system. The resulting nonlinear curve (solid line in Fig. 4) describes the measured data reasonably well and also shows a mainly quadratic dependency. We hope to further approach the fixed-atom limit in our experiment by extending our cooling protocol from one to three dimensions[27].

For completeness, we also analysed the nonlinear theory of optical bistability[16,17] and found that it is inconsistent with all of the measurements presented here, as shown with simulations (see Supplementary Information, Discussion and Figs S1,S2). Specifically, the bistability theory predicts a behaviour close to the one we obtained with the theory of coupled oscillators. Explained differently, according to bistability theory, we are operating on the lower branch, where the corresponding nonlinear response is small (dashed line in Fig. 4). Indeed, the reported nonlinearity occurs with an occupation probability of the atomic excited state of at most 0.07. This is what makes it radically different from and dominant over the standard saturation nonlinearity for a two-state atom.

In summary, our experiment enters a new regime, with nonlinear quantum optics at the level of individual atomic and photonic quanta. In the future, we plan to investigate the photon statistics and the spectrum of the light transmitted through the

cavity. Once improved cooling forces are implemented to better localize the atom in the cavity mode, new multiphoton states could be produced by applying techniques originally developed for a single atom and single photons to the case of a single atom–cavity system and multiple photons. Other applications in quantum information science include a single-photon transistor, where one photon controls the propagation of another photon[20].

Received 10 January 2008; accepted 12 March 2008; published 13 April 2008.

References

1. Berman, P. R. (ed.) *Cavity Quantum Electrodynamics* (Advances in Atomic, Molecular, and Optical Physics, Academic, New York, 1994).
2. Boca, A. *et al.* Observation of the vacuum Rabi spectrum for one trapped atom. *Phys. Rev. Lett.* **93**, 233603 (2004).
3. Maunz, P. *et al.* Normal-mode spectroscopy of a single-bound-atom-cavity system. *Phys. Rev. Lett.* **94**, 033002 (2005).
4. Puppe, T. *et al.* Trapping and observing single atoms in a blue-detuned intracavity dipole trap. *Phys. Rev. Lett.* **99**, 013002 (2007).
5. Wallraff, A. *et al.* Strong coupling of a single photon to a superconducting qubit using circuit quantum electrodynamics. *Nature* **431**, 162–167 (2004).
6. Reithmaier, J. P. *et al.* Strong coupling in a single quantum dot-semiconductor microcavity system. *Nature* **432**, 197–200 (2004).
7. Yoshie, T. *et al.* Vacuum Rabi splitting with a single quantum dot in a photonic crystal nanocavity. *Nature* **432**, 200–203 (2004).
8. Peter, E. *et al.* Exciton-photon strong-coupling regime for a single quantum dot embedded in a microcavity. *Phys. Rev. Lett.* **95**, 067401 (2005).
9. Khitrova, G., Gibbs, H. M., Kira, M., Koch, S. W. & Scherer, A. Vacuum Rabi splitting in semiconductors. *Nature Phys.* **2**, 81–90 (2006).
10. Press, D. *et al.* Photon antibunching from a single quantum-dot-microcavity system in the strong coupling regime. *Phys. Rev. Lett.* **98**, 117402 (2007).
11. Hennessy, K. *et al.* Quantum nature of a strongly coupled single quantum dot-cavity system. *Nature* **445**, 896–899 (2007).
12. Carmichael, H. J., Tian, L., Ren, W. & Alsing, P. in *Cavity Quantum Electrodynamics* (ed. Berman, P. R.) 381–423 (Advances in Atomic, Molecular, and Optical Physics, Academic, New York, 1994).
13. Rempe, G., Walther, H. & Klein, N. Observation of quantum collapse and revival in a one-atom maser. *Phys. Rev. Lett.* **58**, 353–356 (1987).
14. Brune, M. *et al.* Quantum Rabi oscillation: A direct test of field quantization in a cavity. *Phys. Rev. Lett.* **76**, 1800–1803 (1996).
15. Schuster, D. I. *et al.* Resolving photon number states in a superconducting circuit. *Nature* **445**, 515–518 (2007).
16. Rempe, G., Thompson, R. J., Brecha, R. J., Lee, W. D. & Kimble, H. J. Optical bistability and photon statistics in cavity quantum electrodynamics. *Phys. Rev. Lett.* **67**, 1727–1730 (1991).
17. Lugiato, L. A. & Narducci, L. M. in *Fundamental Systems in Quantum Optics, Les Houches, Session LIII, 1990* (eds Dalibard, J., Raimond, J. M. & Zinn-Justin, J.) 941 (Elsevier Science, North-Holland, Amsterdam, 1992).
18. Srinivasan, K. & Painter, O. Linear and nonlinear optical spectroscopy of a strongly-coupled microdisk-quantum dot system. *Nature* **450**, 862–865 (2007).
19. Englund, D., Faraon, A., Stoltz, N., Petroff, P. & Vučković, J. Controlling cavity reflectivity with a single quantum dot. *Nature* **450**, 857–861 (2007).
20. Chang, D. E., Sørensen, A. S., Demler, E. A. & Lukin, M. D. A single-photon transistor using nano-scale surface plasmons. *Nature Phys.* **3**, 807–812 (2007).
21. Carmichael, H. J., Kochan, P. & Sanders, B. C. Photon correlation spectroscopy. *Phys. Rev. Lett.* **77**, 631–634 (1996).
22. Thompson, R. J., Turchette, Q. A., Carnal, O. & Kimble, H. J. Nonlinear spectroscopy in the strong-coupling regime of cavity QED. *Phys. Rev. A* **57**, 3084–3104 (1998).
23. Meekhof, D. M., Monroe, C., King, B. E., Itano, W. M. & Wineland, D. J. Generation of nonclassical motional states of a trapped atom. *Phys. Rev. Lett.* **76**, 1796–1799 (1996).
24. Mielke, S. L., Foster, G. T. & Orozco, L. A. Nonclassical intensity correlations in cavity QED. *Phys. Rev. Lett.* **80**, 3948–3951 (1998).
25. Foster, G. T., Orozco, L. A., Castro-Beltran, H. M. & Carmichael, H. J. Quantum state reduction and conditional time evolution of wave-particle correlations in cavity QED. *Phys. Rev. Lett.* **85**, 3149–3152 (2000).
26. Birnbaum, K. M. *et al.* Photon blockade in an optical cavity with one trapped atom. *Nature* **436**, 87–90 (2005).
27. Nußmann, S. *et al.* Vacuum-stimulated cooling of single atoms in three dimensions. *Nature Phys.* **1**, 122–125 (2005).

Supplementary Information accompanies this paper on www.nature.com/naturephysics.

Acknowledgements

We thank N. Syassen for early contributions. Partial support by the Bavarian PhD programme of excellence QCCC, the DFG research unit 635, the DFG cluster of excellence MAP and the EU project SCALA are gratefully acknowledged.

Author information

Reprints and permission information is available online at http://npg.nature.com/reprintsandpermissions. Correspondence and requests for materials should be addressed to G.R.

24. L. M. Duan, R. Raussendorf, *Phys. Rev. Lett.* **95**, 080503 (2005).
25. J. H. N. Loubser, J. A. van Wyk, *Diamond Res.* **11**, 4 (1977).
26. F. Jelezko *et al.*, *Phys. Rev. Lett.* **93**, 130501 (2004).
27. M. V. G. Dutt *et al.*, *Science* **316**, 1312 (2007).
28. M. Mehring, J. Mende, W. Scherer, *Phys. Rev. Lett.* **90**, 153001 (2003).
29. A. Peres, *Phys. Rev. Lett.* **77**, 1413 (1996).
30. M. Horodecki, P. Horodecki, R. Horodecki, *Phys. Lett. A* **223**, 1 (1996).
31. J. Harrison, M. J. Sellars, N. B. Manson, *Diamond Relat. Mater.* **15**, 586 (2006).
32. V. Giovannetti, S. Lloyd, L. Maccone, *Science* **306**, 1330 (2004).

33. We acknowledge financial support by the European Union (QAP, EQUIND, and NEDQIT) and Deutsche Forschungsgemeinschaft (SFB/TR21 and the JPN-GER cooperative program). N.M. is supported by the program KAKENHI (grant no. 18740175), and V.J. is supported by the Humboldt Foundation. We thank D. Twitchen from Element Six (UK) Ltd. for providing us with ultrapure chemical vapor deposition diamond samples.

Supporting Online Material

www.sciencemag.org/cgi/content/full/320/5881/1326/DC1
Materials and Methods
Figs. S1 to S4
Tables S1 to S3
References

3 March 2008; accepted 8 May 2008
10.1126/science.1157233

Strong Dissipation Inhibits Losses and Induces Correlations in Cold Molecular Gases

N. Syassen,[1] D. M. Bauer,[1] M. Lettner,[1] T. Volz,[1]* D. Dietze,[1]† J. J. García-Ripoll,[1,2] J. I. Cirac,[1] G. Rempe,[1] S. Dürr[1]‡

Atomic quantum gases in the strong-correlation regime offer unique possibilities to explore a variety of many-body quantum phenomena. Reaching this regime has usually required both strong elastic and weak inelastic interactions because the latter produce losses. We show that strong inelastic collisions can actually inhibit particle losses and drive a system into a strongly correlated regime. Studying the dynamics of ultracold molecules in an optical lattice confined to one dimension, we show that the particle loss rate is reduced by a factor of 10. Adding a lattice along the one dimension increases the reduction to a factor of 2000. Our results open the possibility to observe exotic quantum many-body phenomena with systems that suffer from strong inelastic collisions.

Strong interactions are responsible for many interesting quantum phenomena in many-body systems: high-temperature superconductivity (*1*), excitations with fractional statistic (*2*), topological quantum computation (*3*), and a plethora of exotic behaviors in magnetic systems (*4*). One of the main physical mechanisms that gives rise to strong correlations for bosonic particles can be understood as follows. At low temperatures and for strong elastic repulsive interactions, particles tend to stay far away from each other in order to keep the energy low. That is, the wave function describing the particles tends to vanish when two of them coincide at the same position. In order to fulfill these constraints, this wave function has to be highly entangled at all times, which may give rise to counterintuitive effects both in the equilibrium properties as well as in the dynamics. In one dimension, for example, this occurs in the so-called Tonks-Girardeau gas (TGG) (*5*, *6*), where the set of allowed wave functions for bosonic particles coincide (up to some transformation) with those of free fermions. Despite being bosons, the excitation spectrum, the evolution of the density distribution, etc. correspond to those of fermionic particles. In two dimensions, the same mechanism leads to the fractional quantum Hall effect (*7*), where the ground state as well as the low energy excitations fulfill the above-mentioned constraint, giving rise to the existence of anyons, which behave neither like bosons nor fermions but have fractional statistics (*2*).

We show that inelastic interactions can be used to reach the strong correlation regime with bosonic particles: This may seem surprising because inelastic collisions are generally associated with particle losses. This behavior can be understood by using an analogy in classical optics, where light absorption is expressed by an imaginary part of the refractive index. If an electromagnetic wave impinges perpendicularly on a surface between two media with complex refractive indices n_1 and n_2, then a fraction $|(n_1 - n_2)/(n_1 + n_2)|^2$ of the intensity will be reflected. In the limit $|n_2| \to \infty$, the light is perfectly reflected off the surface, irrespective of whether n_2 is real or complex. In our case, bosons interacting with large imaginary (*8*, *9*) scattering length almost perfectly reflect off each other for an analogous reason, thereby giving rise to the same constraints in the particles' wave function as the ones corresponding to elastic collisions and thus to the same physical phenomena. In our experiment, the correlations manifest themselves in a strong suppression of the rates at which particles are lost because of inelastic collisions.

Our experiment used molecules confined to one dimension by an optical lattice, both with and without a periodic potential along the one dimension. We started with the transfer of a Bose-Einstein condensate (BEC) of ^{87}Rb atoms into a three-dimensional (3D) optical lattice in such a way that the central region of the resulting Mott insulator contains exactly two atoms at each lattice site. A Feshbach resonance at 1007.4 G (*10*) was used to associate the atom pairs to molecules (*11*). Subsequently, the magnetic field was held at 1005.5 G. Atoms remaining after the association were removed with blast light. This procedure prepared a quantum state that contains one molecule at each site of a 3D optical lattice (*12*, *13*). The optical-lattice potential seen by a molecule is $-V_\perp\cos^2(kx) - V_\perp\cos^2(ky) - V_\parallel\cos^2(kz)$, where $\lambda = 2\pi/k = 830.440$ nm is the light wavelength. At the end of the state preparation, $V_\parallel$ is equal to $V_\perp$,

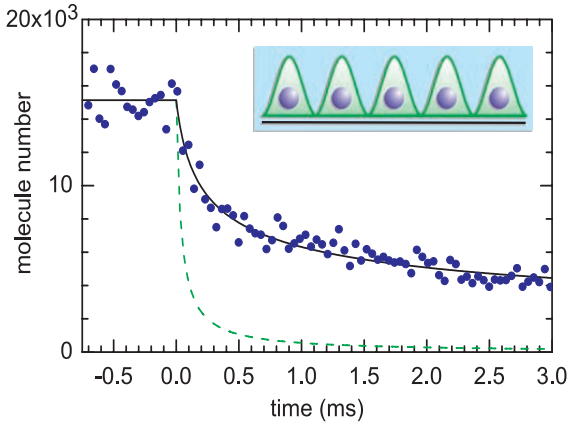

Fig. 1. Time-resolved loss of molecules at $V_\parallel = 0$. The loss begins at $t = 0$. The solid line shows a fit of Eq. 2 to the experimental data (•) with $t \leq 1$ ms. The best-fit value is $\chi n^3(0) = 4.3$/ms, corresponding to $K_{3D} = 2.2 \times 10^{-10}$ cm^3/s and, at $t = 0$, to $g^{(2)} = 0.11$. The dashed line shows the expectation for an uncorrelated system. The observed loss is much slower than the dashed line because of strong correlations.

[1]Max-Planck-Institut für Quantenoptik, Hans-Kopfermann-Straße 1, 85748 Garching, Germany. [2]Universidad Complutense, Facultad de Físicas, Ciudad Universitaria s/n, 28040 Madrid, Spain.

*Present address: Institute of Quantum Electronics, Eidgenössische Technische Hochschule (ETH)–Hönggerberg, 8093 Zürich, Switzerland.
†Present address: Institut für Photonik, Technische Universität Wien, Gußhausstraße 25-29, 1040 Wien, Austria.
‡To whom correspondence should be addressed. E-mail: stephan.duerr@mpq.mpg.de

which equals $127E_r$, where $E_r = \hbar^2k^2/2m$ is the molecular recoil energy and m is the mass of one molecule.

After state preparation, $V_\parallel$ was linearly ramped down to its final value. After this ramp, we have an array of tubes of 1D gases. We chose a ramp duration of 0.5 ms. For much faster ramps, we observed a substantial broadening of the momentum distribution along the tubes. For much slower ramps, particle loss during the ramp became noticeable. After the ramp, the system was allowed to evolve for a variable hold time at the final value of $V_\parallel$. During this hold time, molecules collided inelastically, leading to loss. After the hold time, all molecules were dissociated (*11*) into atom pairs by using the Feshbach resonance. The dissociation terminated the loss. Lastly, the magnetic field and the lattice light were switched off simultaneously, and the number of atoms was determined from a time-of-flight absorption image.

The experimental data represent an average over a large number of tubes of different lengths. This is not critical because the initial 1D density, $n(0) = 2/\lambda$, is identical in all tubes. The lattice beams that create $V_\perp$ have a finite waist. This results in a harmonic confinement with angular frequency $\omega_\parallel = 2\pi \times 71$ Hz along the tubes. This is negligible as long as we evaluate the loss only for much faster time scales. In the decay of the molecule number as a function of hold time at $V_\parallel = 0$ (Fig. 1), the ramp-down of $V_\parallel$ begins at $t = -0.5$ ms and ends at $t = 0$. The data do not show noticeable loss during the ramp-down. In order to avoid complications because of the harmonic confinement $\omega_\parallel$ along the tubes, we processed only data for $t \leq 1$ ms.

A quantitative understanding of the loss process is based on the 1D particle density n, which evolves according to (*14*)

$$\frac{dn}{dt} = -Kn^2g^{(2)} \qquad (1)$$

where $g^{(2)} = \langle n^2\rangle/\langle n\rangle^2$ is the pair correlation function that gives the reduction factor of the loss rate compared with an uncorrelated state where $g^{(2)} = 1$. K is the 1D loss rate coefficient, which can be related to the 3D scattering properties as follows: First, the scattering potential can be modeled as a delta interaction with 1D interaction strength g, yielding $K = -2\mathrm{Im}(g)/\hbar$ (*14*). Second, extending the arguments of (*15*) to the case of a complex-valued 3D scattering length a, one obtains $g = 2\hbar^2 a/\left\{ma_\perp^2\left[1 + a\zeta\left(\frac{1}{2}\right)/\sqrt{2}a_\perp\right]\right\}$, where $a_\perp$ is the size of the gas in the perpendicular direction and ζ denotes the Riemann zeta function with $\zeta(1/2) \approx -1.46$. The real and imaginary parts of a, $\mathrm{Re}(a)$ and $\mathrm{Im}(a)$, represent elastic and inelastic scattering, respectively.

For the ground state of the TGG, we can derive an analytic expression for $g^{(2)}$. By introducing a dimensionless interaction strength $\gamma = mg/\hbar^2 n$ and using the same techniques as in (*16*, *17*), we obtain $g^{(2)} = 4\pi^2/3|\gamma|^2$ in the limit $|\gamma| >> 1$. Inserting this expression in Eq. 1, we obtain

$$\frac{dn}{dt} = -\chi n^4 \qquad (2)$$

where $\chi = 4\pi^2\hbar^4K/3m^2|g|^2$. This equation gives a prediction for the particle losses for a low-energy

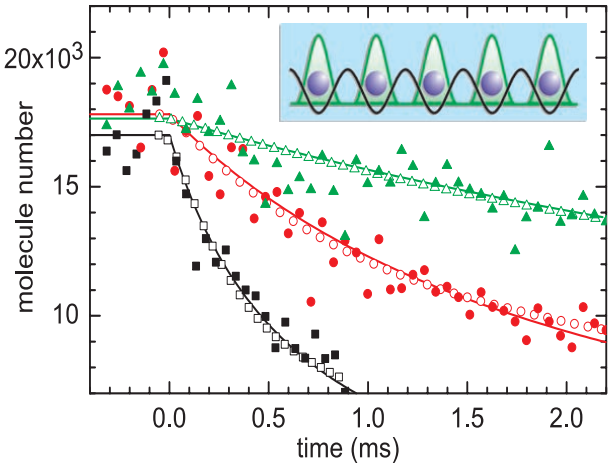

Fig. 2. Loss at $V_\parallel \neq 0$. Solid lines show fits of Eq. 3 to the experimental data (solid symbols). Open symbols show results of our numerical calculations. Black squares, red circles, and green triangles correspond to $V_\parallel/E_r$ values of 1.8, 3.9, and 6.0, respectively.

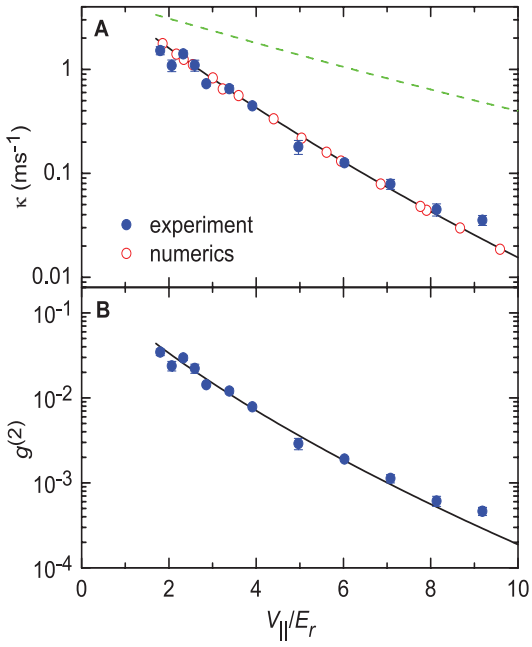

Fig. 3. Loss at different lattice depths $V_\parallel$. **(A)** Fits as in Fig. 2 yield the experimental results (•) for κ. A fit of Eq. 4 to the data yields the solid line. The best-fit value is $K_{3D} = 1.7 \times 10^{-10}$ cm^3/s. The experimental data and the analytic model agree well with results of our numerical calculations (°). For comparison, the dashed line shows the naïve estimate $2J/\hbar$, which is nowhere close to the data. Error bars indicate one statistical standard error. **(B)** Pair correlation function $g^{(2)} = \kappa/\Gamma$ calculated from the data in (A).

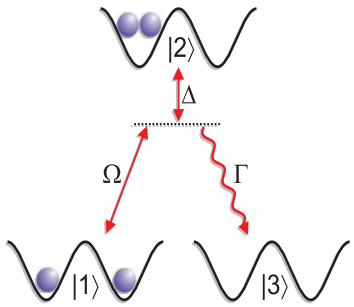

Fig. 4. Particle losses in a 1D lattice. The initial level $|1\rangle$ contains exactly one particle at each lattice site. State $|2\rangle$ is obtained after one tunneling process. Population in state $|2\rangle$ decays incoherently into state $|3\rangle$ with rate Γ. The tunneling coupling between states $|1\rangle$ and $|2\rangle$ can be described by a Rabi frequency Ω and a detuning Δ. In the limit $\Gamma >> \Omega$, the effective decay rate from $|1\rangle \rightarrow |3\rangle$ is $\Gamma_{eff} = \Omega^2/\{\Gamma[1 + (2\Delta/\Gamma)^2]\}$, and the population of level $|2\rangle$ after a time $t >> 1/\Gamma$ is Γ_{eff}/Γ times that of level $|1\rangle$ (*29*). The parameters are related to the Bose-Hubbard parameters by $\Gamma = -2\mathrm{Im}(U)/\hbar$, $\Delta = \mathrm{Re}(U)/\hbar$, and $\Omega = \sqrt{8}J/\hbar$.

TGG. Similar considerations apply to inelastic three-body collisions (*18*–*20*). Note that a TGG at finite temperature has recently been observed experimentally (*21*–*23*) but for the known case of strong elastic interactions.

A fit of Eq. 2 to the data in Fig. 1 with $t \leq 1$ ms yields $\mathrm{Im}(1/a) = 1/(24\ \mathrm{nm})$. Combined with $|\mathrm{Re}(a)| \ll |\mathrm{Im}(a)|$ (*14*), this yields $g^{(2)} = 0.11 \pm 0.01$ at $t = 0$. This shows that the loss rate is strongly reduced because of correlations. $g^{(2)} \propto n^2$ decreases with time, so that the loss rate is reduced even further.

From these results, we can determine the two-body loss coefficient for a BEC, $K_{3D} = -8\pi\hbar\mathrm{Im}(a)/m = 2.2 \times 10^{-10} \pm 0.2 \times 10^{-10}\ \mathrm{cm}^3/\mathrm{s}$. This agrees fairly well with the measurements discussed below and with a previous measurement (*24*) at 1005.8 G that yielded $K_{3D} = 1.5 \times 10^{-10}\ \mathrm{cm}^3/\mathrm{s}$. For comparison we note that, if losses were not inhibited, that is, $g^{(2)} = 1$, then the loss should follow the dashed line, which is calculated with K_{3D} from (*24*). Clearly, the loss rate is reduced.

This reduction is directly related to the fact that the spatial wave functions of the particles do not overlap, and thus they become strongly correlated. Further support for this conclusion comes from the time dependence of our data. If the system were weakly correlated, then $g^{(2)} \approx 1$ would be time independent. Equation 1 would then predict that the number of particles N follows $dN/dt \propto N^2$ instead of $dN/dt \propto N^4$ if we are close to the TGG ground state (*14*). We fit $dN/dt \propto N^p$ with an arbitrary power p to the data with $t \leq 1$ ms. This yields $p = 4.3 \pm 0.6$, in good agreement with $p = 4$.

We now turn to a situation with a lattice potential along the 1D tubes with $V_\parallel \ll V_\perp$. The motion perpendicular to the tubes remains frozen out as before, but the motion along the tubes is now described as hopping between discrete lattice sites. This is a natural way of amplifying the effects due to interactions and thus reaching more deeply into the strong-correlation regime (*25*, *21*). Apart from that, many paradigmatic models in solid state and other fields of physics assume a lattice structure. We performed measurements (Fig. 2) similar to that in Fig. 1 for various values of the lattice depth $V_\parallel$. Here, the temporal change of $g^{(2)}$ is negligible (*14*). Spatial integration of Eq. 1 yields

$$\frac{dN}{dt} = -\frac{\kappa}{N(0)} N^2(t) \qquad (3)$$

where we abbreviated $\kappa = Kn(0)\, g^{(2)}$. We fit this to the data with $N(t) \geq N(0)/2$ in order to neglect the harmonic confinement along the tube. The best-fit values for the loss rate κ obtained for different lattice depths $V_\parallel$ are shown in Fig. 3A.

A prediction for κ can be developed starting from the Lieb-Liniger Hamiltonian (*16*, *14*). In the presence of a periodic potential in the tight-binding limit, we obtain a Bose-Hubbard model (*26*) with tunneling amplitude J and on-site interaction $\mathrm{Re}(U)$. J and U can be expressed in terms of m, a, and a Wannier function. $\Gamma = -2\mathrm{Im}(U)/\hbar$ is the rate at which two particles at the same site are lost. In this model, losses occur when two particles occupy neighboring sites and one of them hops to the other's site. For strong inelastic interactions ($J/\hbar\Gamma \ll 1$), we obtain an effective loss rate Γ_{eff} for two neighboring particles (Fig. 4). An extension of this double-well model to many sites yields $\kappa = 4\Gamma_{\mathrm{eff}}$ (*14*) so that

$$\kappa = \frac{32J^2}{\hbar^2\Gamma}\left\{1 + \left[\frac{\mathrm{Re}(a)}{\mathrm{Im}(a)}\right]^2\right\}^{-1} \qquad (4)$$

This coefficient shows again that for strong inelastic interactions ($\Gamma \to \infty$) particle losses are inhibited. For large, finite values of Γ one can, as before, observe such an inhibition by looking at the particle losses. We fit Eq. 4 to the data in Fig. 3A. With $|\mathrm{Re}(a)| \ll |\mathrm{Im}(a)|$ there is only one free fit parameter. The best-fit value is $K_{3D} = 1.7 \times 10^{-10} \pm 0.3 \times 10^{-10}\ \mathrm{cm}^3/\mathrm{s}$, which is close to the result of Fig. 1. As $V_\parallel/E_r$ increases from 1.7 to 10, Γ increases from 45/ms to 82/ms.

In order to test the quality of this analytic model, we performed extensive numerical calculations by solving the master equation (*14*) with use of matrix product density operators (*27*). They reveal that the system maps to a very good approximation to a fermionized gas and that it loses its memory about the initial state in a time $\sim 1/\Gamma$. During this very short time, only little loss occurs, and after this short transient the loss is well described by a time-independent $g^{(2)}$ with κ from Eq. 4. We find good agreement between experimental data, analytic model, and numerical results in Figs. 2 and 3.

For $|\mathrm{Re}(a)| \ll |\mathrm{Im}(a)|$, Eq. 4 tells us that the larger the loss coefficient Γ, the smaller the actual loss rate κ. This means that fast on-site loss tends to preserve the initial state and thus suppresses tunneling in the many-body system. This can be interpreted as a manifestation of the continuous quantum Zeno effect (*28*): Fast dissipation freezes the system in its initial state. Without this Zeno effect, one might naïvely estimate that tunneling would occur at a rate $\sim 2J/\hbar$. If each such tunneling event would lead to immediate loss, then $2J/\hbar$ should set the time scale for the loss, but that estimate is too naïve, as the dashed line in Fig. 3A shows.

The value of K_{3D} extracted from Fig. 3A is used to calculate Γ and thus $g^{(2)} = \kappa/\Gamma$ (*14*) for each experimental data point. The results (Fig. 3B) agree well with the theoretical expectation (solid line) based on the same value of K_{3D}. The smallest measured value of $g^{(2)} = 4.6 \times 10^{-4} \pm 0.7 \times 10^{-4}$ represents an improvement of more than two orders of magnitude over previous experiments (*23*). Note that a noninteracting gas has $g^{(2)} = 1$ at any lattice depth. The observed suppression of $g^{(2)}$ is caused by the inelastic interactions, not by the lattice itself. Moreover, the strength of the correlations in our experiment is determined by the interparticle interactions. This situation differs fundamentally from experiments in very deep lattices where tunneling is negligible on the time scale of the experiment, interactions are irrelevant, and bosonic symmetrization of the wave function is possible but has no detectable consequences.

The mechanism introduced here could also give rise to other strongly correlated states, such as a Laughlin state (*7*) or one with anyonic excitation (*2*). The present paper opens up the possibility of observing exotic quantum many-body phenomena in systems that suffer from strong inelastic collisions. Furthermore, the rate coefficients for those collisions may be artificially increased by using photoassociation or Feshbach resonances, thus further reducing the actual loss rate in the strongly correlated regime.

References and Notes

1. P. W. Anderson, *Science* **235**, 1196 (1987).
2. F. Wilczek, *Phys. Rev. Lett.* **48**, 1144 (1982).
3. A. Y. Kitaev, *Ann. Phys. (N.Y.)* **303**, 2 (2003).
4. A. Auerbach, *Interacting Electrons and Quantum Magnetism* (Springer, Berlin, 1994).
5. L. Tonks, *Phys. Rev.* **50**, 955 (1936).
6. M. Girardeau, *J. Math. Phys.* **1**, 516 (1960).
7. H. L. Stormer, D. C. Tsui, A. C. Gossard, *Rev. Mod. Phys.* **71**, S298 (1999).
8. B. J. Verhaar, *Laser Phys.* **4**, 1050 (1994).
9. J. L. Bohn, P. S. Julienne, *Phys. Rev. A* **56**, 1486 (1997).
10. A. Marte *et al.*, *Phys. Rev. Lett.* **89**, 283202 (2002).
11. S. Dürr, T. Volz, A. Marte, G. Rempe, *Phys. Rev. Lett.* **92**, 020406 (2004).
12. T. Volz *et al.*, *Nat. Phys.* **2**, 692 (2006).
13. S. Dürr *et al.*, in *Atomic Physics 20: XXth International Conference on Atomic Physics*, C. Roos, H. Häffner, R. Blatt, Eds., American Institute of Physics (AIP) Conference Proceedings No. 869 (AIP, New York, 2006), pp. 278–283.
14. Modeling details are available on *Science* Online.
15. M. Olshanii, *Phys. Rev. Lett.* **81**, 938 (1998).
16. E. H. Lieb, W. Liniger, *Phys. Rev.* **130**, 1605 (1963).
17. D. M. Gangardt, G. V. Shlyapnikov, *Phys. Rev. Lett.* **90**, 010401 (2003).
18. Y. Kagan, B. V. Svistunov, G. V. Shlyapnikov, *J. Exp. Theor. Phys. Lett.* **42**, 209 (1985).
19. E. A. Burt *et al.*, *Phys. Rev. Lett.* **79**, 337 (1997).
20. B. Laburthe Tolra *et al.*, *Phys. Rev. Lett.* **92**, 190401 (2004).
21. B. Paredes *et al.*, *Nature* **429**, 277 (2004).
22. T. Kinoshita, T. Wenger, D. S. Weiss, *Science* **305**, 1125 (2004); published online 29 July 2004 (10.1126/science.1100700).
23. T. Kinoshita, T. Wenger, D. S. Weiss, *Phys. Rev. Lett.* **95**, 190406 (2005).
24. N. Syassen, T. Volz, S. Teichmann, S. Dürr, G. Rempe, *Phys. Rev. A* **74**, 062706 (2006).
25. T. Stöferle, H. Moritz, C. Schori, M. Köhl, T. Esslinger, *Phys. Rev. Lett.* **92**, 130403 (2004).
26. D. Jaksch, C. Bruder, J. I. Cirac, C. W. Gardiner, P. Zoller, *Phys. Rev. Lett.* **81**, 3108 (1998).
27. F. Verstraete, J. J. García-Ripoll, J. I. Cirac, *Phys. Rev. Lett.* **93**, 207204 (2004).
28. B. Misra, E. C. G. Sudarshan, *J. Math. Phys.* **18**, 756 (1977).
29. C. Cohen-Tannoudji, J. Dupont-Roc, G. Grynberg, *Atom-Photon Interactions* (Wiley, New York, 1992), pp. 49–59.

30. We acknowledge financial support of the German Excellence Initiative via the program Nanosystems Initiative Munich and of the Deutsche Forschungsgemeinschaft via SFB 631. J.J.G.-R. acknowledges financial support from the Ramon y Cajal Program and the Spanish projects FIS2006-04885 and CAM-UCM/910758.

Supporting Online Material

www.sciencemag.org/cgi/content/full/320/5881/1329/DC1
SOM Text

16 January 2008; accepted 15 April 2008
10.1126/science.1155309

PRL 99, 201301 (2007) PHYSICAL REVIEW LETTERS week ending 16 NOVEMBER 2007

Analogue of Cosmological Particle Creation in an Ion Trap

Ralf Schützhold* and Michael Uhlmann
Institut für Theoretische Physik, Technische Universität Dresden, D-01062 Dresden, Germany

Lutz Petersen, Hector Schmitz, Axel Friedenauer, and Tobias Schätz†
Max-Planck-Institut für Quantenoptik, Hans-Kopfermann-Str. 1, D-85748 Garching, Germany
(Received 4 June 2007; published 12 November 2007)

We study phonons in a dynamical chain of ions confined by a trap with a time-dependent (axial) potential strength and demonstrate that they behave in the same way as quantum fields in an expanding or contracting Universe. Based on this analogy, we present a scheme for the detection of the analogue of cosmological particle creation which should be feasible with present day technology. In order to test the quantum nature of the particle creation mechanism and to distinguish it from classical effects such as heating, we propose to measure the two-phonon amplitude via the 2nd red sideband transition and to compare it with the one-phonon amplitude (1st red sideband).

DOI: 10.1103/PhysRevLett.99.201301 PACS numbers: 04.62.+v, 32.80.Pj, 42.50.Vk, 98.80.Cq

Introduction.—The theory of quantum fields in curved space-times (see, e.g., [1]) comprises many fascinating and striking phenomena—one of them being the creation of real particles out of the (virtual) quantum vacuum fluctuations by a gravitational field. These effects include Hawking radiation given off by black holes as well as cosmological particle creation. A very similar mechanism—the amplification of quantum vacuum fluctuations due to the rapid expansion of the very early Universe—is (according to our standard model of cosmology) responsible for the generation of the seeds for cosmic structure formation. Hence, even though these effects are far removed from everyday experience, they are very important for the past and the future fate of our Universe.

Therefore, it would be desirable to render these phenomena accessible to an experimental investigation. Probably the most promising way for achieving this goal is to construct a suitable analogue which reproduces relevant features (such as the Hamiltonian) of quantum fields in curved space-times. Along this line of reasoning, proposals based on the analogy between phonons in dynamical Bose-Einstein condensates and quantized fields in an expanding or contracting Universe have been suggested [2]. Unfortunately, the detection of the created phonons in these systems is rather difficult (see also [3]).

On the other hand, the detection of single phonons in ion traps via optical techniques is already state of the art in current technology—which suggests the study of this setup instead. In this Letter, we shall derive the analogy between phonons in an axially time-dependent ion trap and quantum fields in an expanding or contracting Universe and propose a corresponding detection scheme for the analogue of cosmological particle creation. A similar idea has already been pursued in [4], but the proposal presented therein goes along with several problems, which will be discussed below [5].

Cosmological particle creation.—Let us start by briefly reviewing the basic mechanism of particle creation in an expanding or contracting Universe. For simplicity, we consider a real massless scalar field ϕ. Its curved space-time action has the generic form [1] ($\hbar = c = 1$ throughout)

$$\mathcal{A} = \frac{1}{2}\int d^4x\sqrt{|\mathfrak{g}|}[(\partial_\mu\phi)\mathfrak{g}^{\mu\nu}(\partial_\nu\phi) - \zeta\Re\phi^2], \quad (1)$$

where $\mathfrak{g}^{\mu\nu}$ denotes the metric and $\mathfrak{g} = \det\{\mathfrak{g}_{\mu\nu}\}$ its determinant (Jacobian). In general, scalar fields could be coupled to the Ricci (curvature) scalar $\Re$ via a dimensionless parameter ζ, but the main results remain valid for $\zeta = 0$. A spatially flat Universe can be described in terms of the Friedman-Robertson-Walker metric [6]

$$ds^2 = \mathfrak{a}^6(t)dt^2 - \mathfrak{a}^2(t)d\boldsymbol{r}^2, \quad (2)$$

with the time-dependent scale parameter $\mathfrak{a}(t)$ corresponding to the cosmic expansion/contraction. Here we have chosen a slightly unusual time-coordinate t related to the proper time τ via $d\tau = \mathfrak{a}^3(t)dt$ in order to simplify the subsequent formulas. After a normal-mode expansion, the wave equation derived from (1) and (2) reads

$$\ddot{\phi}_{\boldsymbol{k}} + [\mathfrak{a}^4(t)\boldsymbol{k}^2 + \zeta\mathfrak{a}^6(t)\Re(t)]\phi_{\boldsymbol{k}} = \ddot{\phi}_{\boldsymbol{k}} + \Omega_{\boldsymbol{k}}^2(t)\phi_{\boldsymbol{k}} = 0; \quad (3)$$

i.e., each mode $\boldsymbol{k}$ just represents a harmonic oscillator with a time-dependent potential strength $\Omega_{\boldsymbol{k}}^2(t)$. If the temporal variation of $\Omega_{\boldsymbol{k}}(t)$ is much slower than the internal frequency ($\dot{\Omega}_{\boldsymbol{k}} \ll \Omega_{\boldsymbol{k}}^2$ and $\ddot{\Omega}_{\boldsymbol{k}} \ll \Omega_{\boldsymbol{k}}^3$, etc.), the quantum state will stay near the ground state (adiabatic theorem). However, if the external time dependence $\Omega_{\boldsymbol{k}}(t)$ is too fast (nonadiabatic), the ground-state wave function cannot adapt to this change anymore and hence the evolution will transform the initial ground state into an excited state in general (cosmological particle creation). Because of the linearity of Eq. (3), the wave-function remains Gaussian (though with a different width) and hence the initial vacuum state $|0\rangle = |\psi(t \to -\infty)\rangle$ containing no particles

PRL 99, 201301 (2007) PHYSICAL REVIEW LETTERS week ending 16 NOVEMBER 2007

$\forall_{\boldsymbol{k}} \hat{a}_{\boldsymbol{k}}|0\rangle = 0$ evolves into a squeezed state

$$|\psi(t \to \infty)\rangle = \prod_{\boldsymbol{k}} \exp\{\xi_k \hat{a}^\dagger_{\boldsymbol{k}} \hat{a}^\dagger_{-\boldsymbol{k}} - \text{H.c.}\}|0\rangle = |0\rangle + \sum_{\boldsymbol{k}} \xi_k |1_{\boldsymbol{k}}, 1_{-\boldsymbol{k}}\rangle + \mathcal{O}(\xi_k^2), \quad (4)$$

which does contain pairs of particles $|1_{\boldsymbol{k}}, 1_{-\boldsymbol{k}}\rangle = |\boldsymbol{k}, -\boldsymbol{k}\rangle$ with opposite $\boldsymbol{k}$ (momentum conservation). The squeezing parameter ξ_k for each mode is determined by the solution of Eq. (3) and thus by the external time dependence $\Omega_{\boldsymbol{k}}(t)$, i.e., the rapidity of the cosmic evolution $\alpha(t)$. It governs the number of created particles per mode via

$$\langle \hat{n}_{\boldsymbol{k}} \rangle = \langle \psi(t \to \infty)|\hat{a}^\dagger_{\boldsymbol{k}} \hat{a}_{\boldsymbol{k}}|\psi(t \to \infty)\rangle = \sinh^2(|\xi_k|). \quad (5)$$

Ion-trap analogue.—Assuming a strong radial confinement of the ions, we consider their axial motion only. In a time-dependent harmonic axial potential described by the oscillator frequency $\omega_{\text{ax}}(t)$, the position q_i of the ith ion obeys the equation of motion

$$\ddot{q}_i + \omega_{\text{ax}}^2(t) q_i = \gamma \sum_{j \neq i} \frac{\text{sign}(i-j)}{(q_i - q_j)^2}, \quad (6)$$

where the factor γ encodes the strength of the Coulomb repulsion between the ions. Assuming a static situation initially, the classical solution to the above equation can be obtained via the scaling ansatz $q_i(t) = b(t) q_i^0$, where q_i^0 are the initial static equilibrium positions, leading to the evolution equation for the scale parameter $b(t)$

$$\ddot{b}(t) + \omega_{\text{ax}}^2(t) b(t) = \frac{\omega_{\text{ax}}^2(0)}{b^2(t)}. \quad (7)$$

In order to treat the quantum fluctuations of the ions (leading to the quantized phonon modes), let us split the full position operator $\hat{q}_i(t)$ for each ion into its classical trajectory $b(t) q_i^0$ and quantum fluctuations $\delta\hat{q}_i(t)$ via $\hat{q}_i(t) = b(t) q_i^0 + \delta\hat{q}_i(t)$. Since these fluctuations $\delta\hat{q}_i(t)$ are very small for ions, we may linearize the full equation of motion (6)

$$\left(\frac{\partial^2}{\partial t^2} + \omega_{\text{ax}}^2(t)\right) \delta\hat{q}_i = \frac{1}{b^3(t)} \sum_j M_{ij} \delta\hat{q}_j, \quad (8)$$

with a time-independent matrix M_{ij} arising from the Coulomb term in (6). Diagonalization of this matrix (normal-mode expansion) yields the phonon modes

$$\left(\frac{\partial^2}{\partial t^2} + \omega_{\text{ax}}^2(t) + \frac{\omega_\kappa^2}{b^3(t)}\right) \delta\hat{q}_\kappa = 0, \quad (9)$$

labeled by κ. The time-independent eigenvalues $\omega_\kappa^2 \geq 0$ of the matrix M_{ij} determine the phonon frequencies. The lowest mode is the center-of-mass mode corresponding to a simultaneous (rigid) motion of the ions. Since the ion distances do not change, the Coulomb term does not contribute in this situation $\omega_\kappa^2 = 0$. The next mode is the breathing mode with $\omega_\kappa^2 = 2\omega_{\text{ax}}^2(0)$. Comparing Eqs. (7) and (9), we see that this mode exactly corresponds to the scaling ansatz; i.e., the ion chain expands or contracts linearly. Hence this is the only mode which can be excited classically (for a purely harmonic potential). I.e., without imperfections such as heating, phonons in the other modes can only be created by quantum effects.

Comparing Eqs. (3) and (9) and identifying $\phi_{\boldsymbol{k}}$ with $\delta\hat{q}_\kappa$, we observe a strong similarity: The wave number $\boldsymbol{k}^2$ in (3) directly corresponds to ω_κ^2 in (9) and the scale factors $\alpha(t)$ and $b(t)$ enter in a similar way. However, an expanding Universe is analogous to a contracting ion chain and vice versa. In the mode-independent terms, the axial trap frequency ω_{ax} acts like the Ricci scalar $\Re$. Interestingly, both are related to the second time-derivatives of the corresponding scale factors $b(t)$ and $\alpha(t)$.

In view of the formal equivalence of Eqs. (7) and (9), we obtain the same effects as in cosmology—in particular, the mixing of creation and annihilation operators

$$\hat{a}_\kappa(t \to \infty) = \alpha_\kappa \hat{a}_\kappa(0) + \beta_\kappa \hat{a}^\dagger_\kappa(0), \quad (10)$$

which can be expressed in terms of the Bogolubov coefficients satisfying $|\alpha_\kappa^2| - |\beta_\kappa^2| = 1$. Note that the above relation is just the operator representation of the squeezing transformation in Eq. (4) with $|\beta_\kappa| \leftrightarrow \sinh(|\xi_k|)$.

Detection scheme.—In the following we describe how to realize the proposed experiment by applying operations closely related to those implemented on qubit-ions in quantum information processing [7]. We focus on initializing the system, simulating the nonadiabatic expansion of space, performing the readout of the final state (particle- or phonon-number distribution) and distinguishing it from a classically describable outcome, for example, caused by thermal heating. To perform a first realization, we will confine one single earth alkaline atomic ion to the axis of a linear radio-frequency trap [8] similar to that described in [9,10]. The required simulation basis can be composed by a $^2S_{1/2}$ electronic ground-state level of $^{25}Mg^+$, here the state $|F = 3; m_f = 3\rangle = |\downarrow\rangle$, and the associated harmonic oscillator levels $|n\rangle$ related to the axial harmonic confinement, as depicted in Fig. 1. At the start of each experiment, the ion will be laser cooled close to the ground state of the axial (external) motion and optically pumped into the electronic (internal) state $|\downarrow\rangle$ [11]. Then we will decrease adiabatically the axial confinement and subsequently reset it nonadiabatically to its initial value (as already proposed in [12] in another context). Since the ground-state wave function of the ion cannot adapt to the restored stiff confinement (nonadiabatic case), it will oscillate symmetrically around the minimum of the final trapping potential [13], i.e., without populating odd motional states. As shown above, this nonclassical oscillation is to be described via a squeezed state (see also [14]) depicted in Fig. 2.

We propose, in addition to established schemes described in [14] or [15], for example, an alternative method to distinguish classical noise (such as the initial thermal

PRL 99, 201301 (2007) PHYSICAL REVIEW LETTERS week ending 16 NOVEMBER 2007

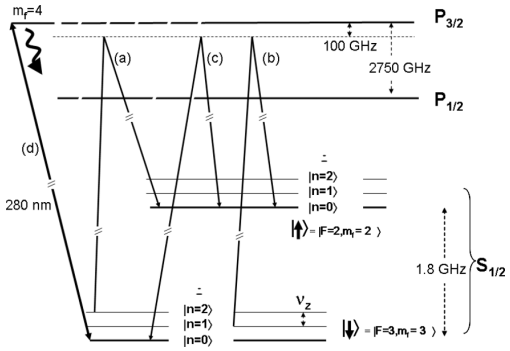

FIG. 1. Schematic of the relevant energy levels (not to scale) of one $^{25}Mg^{+}$ ion. Shown are the ground-state hyperfine levels supplying the two internal states ($|\downarrow\rangle$ and $|\uparrow\rangle$) and the first three equidistant harmonic oscillator levels $|n\rangle$, related to the harmonic axial confinement in a linear ion trap. Typically, the energy splitting of the motional levels and the Zeeman shift induced by an external magnetic field are of the same order of magnitude within 1–10 MHz, therefore much smaller than the Hyperfine splitting of 1.8 GHz, the fine structure splitting of 2750 GHz and the optical transition frequency of the order of 10^{15} Hz. We depict the resonant transition state sensitive detection named (d) and the relevant types of off resonant ($\approx$100 GHz) two-photon stimulated Raman transitions (a),(b), and (c) described in the text.

distribution or heating during the process) from a squeezed state generated by quantum effects considered here. In order to readout the final motional state, we will first couple it (via suitable lasers) to two internal states of the ion. Besides the electronic ground state $|F=3;m_f=3\rangle=|\downarrow\rangle$, the second internal state to span a two-level system (analogous to a qubit) is implemented via a second hyperfine state of $^{25}Mg^{+}$, $|F=2, m_f=2\rangle \equiv |\uparrow\rangle$, separated from the state $|\downarrow\rangle$ by the hyperfine splitting $\omega_0 \simeq 2\pi \times 1.8$ GHz. We will accomplish the coupling of the two internal states $|\downarrow\rangle$, $|\uparrow\rangle$ and the motional states $|n\rangle$ via two-photon stimulated Raman transitions [7] requiring two laser beams ($\lambda \approx$ 280 nm), with wave vector difference $\Delta\boldsymbol{k} = \boldsymbol{k_2} - \boldsymbol{k_1}$ aligned along the trap axis z ($|\Delta k| = \sqrt{2} \times 2\pi/\lambda =$ $2\pi/\lambda_{\text{eff}}$). Via detuning the frequency difference $\omega_2 - \omega_1$ from the hyperfine splitting $\omega_o \pm 2\pi m\nu_z$ by integer multiples m of the axial trapping frequency ν_z, we may drive the carrier-transition ($m=0$) or the first- ($m=1$) and second- ($m=2$) side band transitions, respectively. Note that the spectral resolution of the two-photon stimulated Raman transition is independent on the natural line width $\Gamma = 2\pi \times 43$ MHz of the resonant transition—but proportional to the inverse of the Rabi frequency, adjusted via the intensities or detuning of the laser beams allowing for the resolution of the individual motional states separated by $\nu_z \ll \Gamma$. In order to measure the population of the motional state $|n=2\rangle$, we will drive a sequence of transitions (cf. Fig. 1), synthesized by a second-side band (a) transition ($|\downarrow, n=2\rangle \rightarrow |\uparrow, n=0\rangle$) followed by a carrier (c) transition ($|\uparrow, n=0\rangle \rightarrow |\downarrow, n=0\rangle$). The final readout (d) described below is internal-state dependant and provides us with the population in state $|\downarrow\rangle$. After the sequence (a),(c),(d) of transitions this is almost exclusively equivalent to the population of the motional state $|n=2\rangle$ (because the probability of even higher excitations $|n \geq 3\rangle$ is expected to be much smaller and their Rabi frequencies are also different). This result can then be compared with the outcome after a first red-side band (b) transition ($|\downarrow, n=1\rangle \rightarrow |\uparrow, n=0\rangle$) followed by a carrier (c) transition ($|\uparrow, n=0\rangle \rightarrow |\downarrow, n=0\rangle$), providing the probability of motional excitation $|n=1\rangle$. As soon as we deduce a higher probability for motional state $|n=2\rangle$ than for motional state $|n=1\rangle$, we show the incompatibility with classical effects such as a thermal distribution and get strong evidence for the nonclassical effect of squeezing [16].

Finally, we have to readout the internal state efficiently. To this end, we apply an additional resonant laser beam (d), tuned to a cycling transition [7], coupling only state $|\downarrow\rangle$ resonantly to the $P_{3/2}$ level and providing spontaneous emission at rates of >10 MHz. This allows us to distinguish the "bright" $|\downarrow\rangle$ from the "dark" $|\uparrow\rangle$ state with high accuracy, even at a low detection efficiency (due to the restricted solid angle, etc.).

Envisioned results.—The above mentioned state of the art techniques allow the cooling of the axial motion close to the ground state $\langle\hat{n}\rangle \approx 0.05$ [8] (see also [10,11]) and to optically pump into the down state $|\downarrow\rangle$ with 99% [8] or even higher fidelity [10,11]. First experiments show a possible nonadiabatic variation of the axial motional frequency ν_z between 200 kHz and $\geq$2 MHz with a related rise time of the order of 1 μs, which is sufficiently fast compared to the oscillation period of the lower frequency. Numerical simulations (based on measured temporal variation curves) indicate that we should be able to transfer approximately 20% of the motional state population from the ground state $|n=0\rangle$ into state $|n=2\rangle$, which corresponds to a squeezed state with $\langle\hat{n}\rangle \approx 1$. Starting with a thermal distribution with $\langle\hat{n}\rangle \approx 0.05$ instead of the exact ground state $|n=0\rangle$, there will also be a small final population (a few percent) of the state $|n=1\rangle$; see Fig. 2. However, this

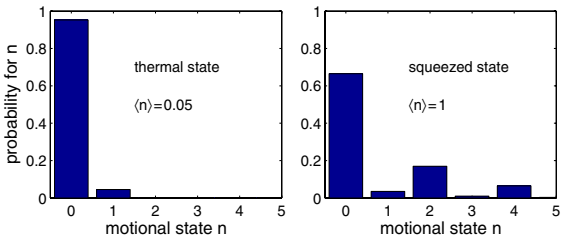

FIG. 2 (color online). Initial and final population of the motional states $|n\rangle$. Left: experimentally realized thermal state with $\langle\hat{n}\rangle = 0.05$. Right: simulated spectrum of the squeezed thermal state with $\langle\hat{n}\rangle = 1$. The predominant population of even motional states emphasizes the nonclassical character of this state.

PRL 99, 201301 (2007) PHYSICAL REVIEW LETTERS week ending 16 NOVEMBER 2007

residual effect will be significantly smaller than the $|n = 2\rangle$ population such that the signatures of squeezing can be measured as described above [16].

Conclusions.—Since the state of the art fidelities for the carrier and sideband transitions as well as the state sensitive detection exceed 99% [10,11], the initialization and measurement of the system can be provided with high accuracy. In order to benefit from these operational fidelities, the main task will be to minimize classical disturbances. For example, we have to carefully balance the applied voltages for confinement during their nonadiabatic changes to prevent classical excitation of the axial motional mode. In comparison to quantum information processing with trapped ions, the requirements for the present proposal may be a bit easier to achieve because the duration of the experiment will be short (around 3 ms) compared to the inverse of the thermal heating rate for motional quanta inside the trap (≤ 0.005 quanta/ms [8]) and because the thermal and the squeezed motional spectra show fundamentally different characteristics; see Fig. 2. It should also be emphasized that it is impossible to energetically resolve individual motional states with pulse durations short compared to the inverse of their frequency difference (see also [4,5]). This impossibility in resolution is related to the Heisenberg uncertainty principle $\Delta E \Delta t \geq \hbar/2$ that allows the creation of pairs of particles (phonons) out of the vacuum (ground) state in first place. Increasing the system towards 8 modes (ions) might be feasible by this proposal with state of the art techniques [17], further scaling might benefit from the technical progress driven by the attempts of the quantum information community.

Apart from experimentally testing the analogue of cosmic particle creation [18] (which might ultimately allow the study of the impact of decoherence and interactions, etc.), the investigation of nonadiabatic switching of trapping potentials and its influence on the quantum state of motion might also shed light on possible problems in schemes where the fast shuttling of ions in a multiplex trap architecture is required for scaling towards a universal quantum computer.

This work was supported by the Emmy-Noether Programme of the German Research Foundation (DFG, Grants No. SCHU 1557/1-2,3 and No. SCHA 973/1-2) and partly by the MPQ Garching and the DFG Cluster of Excellence Munich-Centre for Advanced Photonics.

*schuetz@theory.phy.tu-dresden.de
†Tobias.Schaetz@mpq.mpg.de

[1] N. D. Birrell and P. C. W. Davies, *Quantum Fields in Curved Space* (Cambridge University Press, Cambridge, England, 1982).
[2] See, e.g., C. Barceló, S. Liberati, and M. Visser, Living Rev. Relativity **8**, 12 (2005); as well as R. Schützhold, Lect. Notes Phys. **718**, 5 (2007), and references therein.
[3] R. Schützhold, Phys. Rev. Lett. **97**, 190405 (2006).
[4] P. M. Alsing, J. P. Dowling, and G. J. Milburn, Phys. Rev. Lett. **94**, 220401 (2005).
[5] Let us compare our scenario with the proposal in Ref. [4]. In contrast to the creation of real particles (phonons) whose number can be measured *after* the variation of the trap (facilitating a nearly unlimited measurement time), Ref. [4] is more devoted to the analogue of the Unruh or Gibbons-Hawking effect and proposes a measurement *during* the dynamics, which poses several problems. In order to detect a phonon (via laser pulses), one has to resolve the phonon energy, which requires at least a pulse duration proportional to the inverse of the phonon frequency. Thus, if the rate of change of the axial trap frequency is much larger than the phonon frequencies—as assumed in [4]—the strength of the trap must change by many orders of magnitude during the detection time, which poses many problems—the ions leave the trap, breakdown of the Lamb-Dicke limit, etc. Furthermore, as we see in Eqs. (7) and (9), a temporal change of the axial trap frequency ω_{ax} does not immediately imply a proportional variation of the eigenfrequencies of the phonon modes—which has been implicitly assumed in [4]; see Eq. (4) therein. [Even if we switch off the trap suddenly, the ions start moving on a time scale given by $1/\omega_{\mathrm{ax}}(0)$, i.e., the strength of their initial Coulomb repulsion.] Finally, the mixing of the creation and annihilation operators of the phonon modes in the nonadiabatic regime as in Eqs. (10) has not been taken into account adequately in [4]; see Eq. (4) therein.
[6] Note that $\alpha(t)$ is treated as an external parameter with a given time dependence; i.e., we do not consider the backreaction of the field ϕ onto the dynamics of $\alpha(t)$.
[7] D. J. Wineland *et al.*, J. Res. Natl. Inst. Stand. Technol. **103**, 259 (1998).
[8] T. Schaetz *et al.*, J. Mod. Opt. (to be published); see also L. Petersen (Diploma thesis) arXiv:0704.3535.
[9] M. A. Rowe *et al.*, Quantum Inf. Comput. **2**, 257 (2002).
[10] F. Schmidt-Kaler *et al.*, Appl. Phys. B **77**, 789 (2003).
[11] B. King *et al.*, Phys. Rev. Lett. **81**, 1525 (1998).
[12] D. J. Heinzen and D. J. Wineland, Phys. Rev. A **42**, 2977 (1990).
[13] D. Leibfried *et al.*, Rev. Mod. Phys. **75**, 281 (2003).
[14] D. M. Meekhof *et al.*, Phys. Rev. Lett. **76**, 1796 (1996).
[15] T. Bastin, J. von Zanthier, and E. Solano, J. Phys. B **39**, 685 (2006).
[16] Note that $p(n = 2) > p(n = 1)$ is a strong indication but not a rigorous proof for a squeezed state, which requires measuring the corresponding off-diagonal elements of the density matrix or the associated quadratures. In order to exclude the possibility of a classical (coherently driven) state with $p(n = 2) > p(n = 1)$ and the resulting higher excitations $n > 2$, we would detect the population of the motional state $|n = 0\rangle$ via a another sideband transition $(|\downarrow, n\rangle \rightarrow |\uparrow, n - 1\rangle)$ which is not able to transfer population out of the state $|\downarrow, n = 0\rangle$.
[17] D. Leibfried *et al.*, Nature (London) **438**, 639 (2005); H. Haeffner *et al.*, Nature (London) **438**, 643 (2005).
[18] For the simulation of other relativistic effects in ion traps, see also: L. Lamata, J. León, T. Schätz, and E. Solano, Phys. Rev. Lett. **98**, 253005 (2007).

Simulating the Quantum Magnet with Trapped Ions

Axel Friedenauer, Hector Schmitz, Jan Glückert, Diego Porras, and Tobias Schätz*
Max-Planck-Institut für Quantenoptik,
Hans-Kopfermann-Straße 1, 85748 Garching, Germany

(Dated: 02.06.2008, accepted for publication in Nature Physics, arXiv:quant-ph/0802.4072v1)

To gain deeper insight into the dynamics of complex quantum systems we need a quantum leap in computer simulations. We can not translate quantum behaviour arising with superposition states or entanglement efficiently into the classical language of conventional computers. The solution to this problem, proposed in 1982 [1], is simulating the quantum behaviour of interest in a different quantum system, where the interactions can be controlled and the outcome detected sufficiently well.

Here we study the building blocks for simulating quantum spin Hamiltonians with trapped ions [2]. We experimentally simulate the adiabatic evolution of the smallest non-trivial spin system from paramagnetic into the ferromagnetic order with a quantum magnetisation for two spins of 98%. We prove that the transition is not driven by thermal fluctuations, but is of quantum mechanical origin – the source of quantum fluctuations in quantum phase transitions [3]. We observe a final superposition state of the two degenerate spin configurations for the ferromagnetic order ($|\uparrow\uparrow\rangle+|\downarrow\downarrow\rangle$) corresponding to deterministic entangled states achieved with 88% fidelity. This method should permit scaling to a higher number of coupled spins [2], allowing implementation of simulations that are intractable on conventional computers.

PACS numbers:

I. INTRODUCTION

It is not possible to efficiently describe the time evolution of quantum systems on a classical device, like a conventional computer, since their memory requirements grow exponentially with their size. For example, a classical memory needs to hold 2^{50} numbers to store arbitrary quantum states of 50 spin-1/2 particles. To be able to calculate its evolution demands to derive a matrix of $(2^{50})^2 = 2^{100}$ elements, already exceeding by far the capacity of state of the art computers. Each doubling of computational power permits only one additional spin-1/2 particle to be simulated. To allow for deeper insight into quantum dynamics we need a "quantum leap" in simulation efficiency.

As proposed by Richard Feynman [1], a universal quantum computer would accomplish this step. A huge variety of possible systems are under investigation, with individual trapped ions [4, 5] as quantum bits (qubits) being a very promising architecture. After addressing the established criteria summarized by DiVincenzo [6] on up to 8 ions [7, 8] with operational fidelities exceeding 99% [7–9], there seems to be no fundamental reason why such a device would not be realisable.

An analogue quantum computer, much closer to the original proposal by Feynman, might allow for a shortcut towards quantum simulations. We want to simulate a system by a different one being described by a Hamiltonian that contains all important features of the original system. The simulator needs to be controlled, manipulated and measured in a sufficiently precise manner and has to be rich enough to address interesting questions

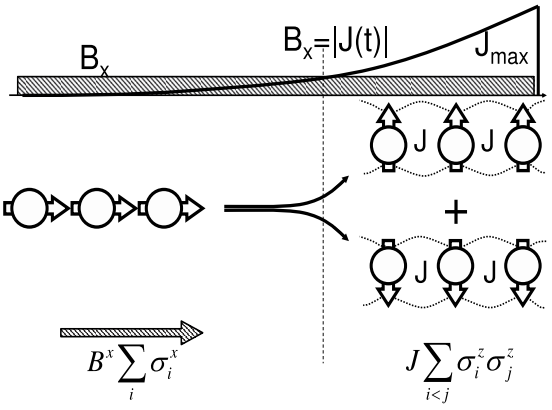

FIG. 1: Phase transition of a quantum magnet: Each ion can simulate a magnetic spin, analogue to an elementary magnet. We initialise the spins in the paramagnetic state $|\rightarrow\rightarrow\ldots\rightarrow\rangle$, the ground state of the Hamiltonian $H_{\mathrm{B}} = -B_x(\sigma_1^x + \sigma_2^x + \ldots + \sigma_N^x)$. This is equivalent to aligning the spins parallel to the simulated magnetic field. Adding an effective spin-spin interaction $J(t)$ (at constant B_x) and increasing it adiabatically to $|J_{\max}| \gg |B_x|$, we expect the system to undergo a quantum phase transition into a ferromagnet, the new ground state of the system (J is symbolized as little chains, trying to keep neighbouring spins aligned). Ideally, the two possible ferromagnetic orders $|\uparrow\uparrow\ldots\uparrow\rangle$ and $|\downarrow\downarrow\ldots\downarrow\rangle$ are degenerate ground states. The spin system should evolve into the superposition state $|\uparrow\uparrow\ldots\uparrow\rangle+|\downarrow\downarrow\ldots\downarrow\rangle$, a maximally entangled "Schrödinger Cat" state/magnet.

*Electronic address: tobias.schaetz@mpq.mpg.de

about the original system. For large coupled spin systems optical lattices might be advantageous [10], while smaller spin systems and degenerate quantum gases might be simulated by trapped ions [2, 11]. Instead of implementing a Hamiltonian with a universal set of gates, direct simulation of the Hamiltonian Hamiltonian can be implemented by adiabatic evolution of the initial state into the corresponding final state of interest.

Here, in a proof-of-principle experiment, we simulate the adiabatic transition from a quantum para- to a quantum (anti-)ferromagnet and illustrate the advantages of the adiabatic quantum simulation (see FIG. 1). We demonstrate the individual access, via rf- and laser fields, to all relevant parameters in the underlying Hamiltonian, representing one out of a large spectrum of quantum spin-Hamiltonians.

II. ADIABATIC QUANTUM SIMULATION

The adiabatic quantum simulation of generic spin-Hamiltonians proposed by Porras and Cirac [2] can be illustrated considering a string of charged spin-1/2 particles confined in a common harmonic potential. Two electronic states of each ion simulate the two-level system of a spin-1/2 magnetic moment, $|\uparrow\rangle$ and $|\downarrow\rangle$. Note that the inter-ion distance of several µm renders any direct spin-spin coupling negligible. The quantum Ising Hamiltonian,

$$H_{\mathrm{Ising}} = H_{\mathrm{B}} + H_{\mathrm{J}} = -B_x \sum_i \sigma_i^x + \sum_{i<j} J_{ij} \sigma_i^z \sigma_j^z \ , \quad (1)$$

consists of two terms. The first denotes the interaction of each individual spin, represented by the Pauli operator σ_i^k (k can be x, y, or z), with a uniform magnetic field B_x pointing into direction x. The second term stands for the spin-spin interaction which tries to align the spins (σ_i^z) parallel or anti-parallel along the z-axis dependent on the sign of the interaction amplitude J_{ij}. To simulate the first term in Eq. 1, the eigenstates of σ_i^z, $|\uparrow\rangle$ and $|\downarrow\rangle$, can be coupled with an electromagnetic field. The latter is simulated by a state-dependent forcing [12, 13], further explained with the help of FIG. 2.

To understand the experiment discussed below, we can consider two extreme scenarios and interactions between nearest neighbours only, $J_{i,i+1} = J$. For the case of $J = 0$ and $B_x > 0$, the ground state of the spin-system has all spins aligned with B_x along the x-axis. This corresponds to the paramagnetically ordered state $|\rightarrow\rightarrow \ldots \rightarrow\rangle$, the eigenstate of the Hamiltonian $-B_x \sum_i \sigma_i^x$ with the lowest energy.

For the opposite case of $B_x = 0$ and $J < 0$ ($J > 0$), the system has an infinite number of degenerate ground states, defined by any superposition of the lowest energy eigenstates of $\sum_{i<j} J_{ij} \sigma_i^z \sigma_j^z$, namely $|\uparrow\uparrow \ldots \uparrow\rangle$ and $|\downarrow\downarrow \ldots \downarrow\rangle$ which represents ferromagnetic order (or $|\uparrow\downarrow\uparrow \ldots \uparrow\downarrow\rangle$ and $|\downarrow\uparrow\downarrow \ldots \downarrow\uparrow\rangle$, the anti-ferromagnetic order, respectively). Initialising the spin system in an eigenstate in the σ^x-basis, starting with $J(t{=}0) = 0$ and $B_x > 0$ and adiabatically increasing $|J(t)|$ to $|J_{\max}| \gg |B_x|$ should evolve the system from the paramagnetic arbitrarily close into the (anti-)ferromagnetic order, as depicted in FIG. 1. A quantum phase transition is supposed to occur at $B_x = |J|$ in the thermodynamic limit of an infinite amount of spins [3, 15].

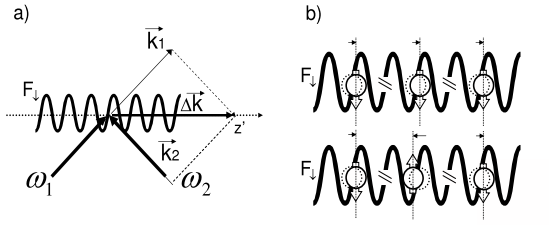

FIG. 2: Simulating the quantum magnet: a) Two perpendicular polarized laser beams of frequency ω_1 and ω_2 induce a state dependent optical dipole force $F_\downarrow = -3/2\, F_\uparrow$ along the trap axis a by the AC-Stark shift (here, only $F_\uparrow$ is depicted). b) For a standing wave $\omega_1 = \omega_2$, the force conditionally changes the distance between neighbouring spins simulating a spin-spin interaction [2] ($F_\uparrow$ ($F_\downarrow$) symbolised by the arrow to the right (left)). Only if all spins are aligned (top), the distance between the spins (ions) remains unchanged. Therefore the total Coulomb energy of the spin system is not increased, defining ferromagnetic order, the quantum magnet, to be the ground state. For $\omega_1 \neq \omega_2$, the sinusoidal force pattern can be seen as a wave moving along the trap axis a pushing or pulling the ions repeatedly at a frequency $\omega_1 - \omega_2$. We chose $\omega_1 - \omega_2$ close to the resonance frequency of the ions oscillating out of phase (stretch mode). The energies of different spin states now depend on the coupling of the spin state to the stretch mode. Energy can be coupled efficiently into the state with different spin orientations (e.g. bottom), defining the not affected upper case as a ground state [14]. The interpretation in terms of an effective spin-spin interaction is further described in methods.

III. EXPERIMENTAL IMPLEMENTATION

We experimentally demonstrate the above features on two spins as follows: We confine two $^{25}Mg^+$ ions in a linear Paul trap [16] and laser-cool them to the Coulomb-crystalline phase where the ions align along the trap axis a. The motion of the ions along a can be described in the basis of normal modes: the oscillation-in-phase-mode (com) and the oscillation-out-of-phase-mode (stretch). The related oscillation frequencies amount to $\omega_{\mathrm{com}} = 2\pi \times 2.1$ MHz and $\omega_{\mathrm{stretch}} = 2\pi \times 3.7$ MHz, respectively.

In our implementation we define the $2\,S_{1/2}$ hyperfine ground states as $|\downarrow\rangle \equiv |F = 3, m_f = 3\rangle$ and state $|\uparrow\rangle \equiv |F = 2\,, m_f = 2\rangle$, which are separated by $\omega \cong 2\pi \times 1.7$ GHz. An external magnetic field B (different from the simulated magnetic field in Eq.1) of 5.5 G orients the magnetisation axis for the projection $\hbar m_f$ of

each ion's angular momentum F. In this field adjacent Zeeman sublevels of the $F = 3$ and $F = 2$ manifolds split by 2.7 MHz per level.

We coherently couple the states $|\downarrow\rangle$ and the $|\uparrow\rangle$ with a resonant radio-frequency field at ω_0 to implement single spin rotations [14, 17],

$$R(\Theta,\phi) = \cos(\Theta/2)\, I - i\sin(\Theta/2)\cos(\phi)\,\sigma^x - i\sin(\Theta/2)\sin(\phi)\,\sigma^y\,, \quad (2)$$

where I is the identity operator, σ^x and σ^y denote the Pauli spin matrices acting on $|\downarrow\rangle$ and $|\uparrow\rangle$, $\Theta/2 = B_x t$ is proportional to the duration t of the rotation and ϕ is the phase of the rf-oscillation, defining the axis of rotation in the x-y-plane of the Bloch sphere.

We provide the effective spin-spin interaction by a state dependent optical dipole force [12, 14, 18]. The relative amplitudes $F_\downarrow = -3/2\, F_\uparrow$ are due to AC-Stark shifts induced by two laser beams at wavelength λ of 280 nm, depicted in FIG. 2a, perpendicular in direction and polarisation with their effective wave-vector difference pointing along the trap axis a. They are detuned 80 GHz blue of the $^2\mathrm{P}_{3/2}$ excited state, with intensities allowing $J/\hbar$ as large as $2\pi \times 22.1$ kHz. We use a walking wave force-pattern by detuning the two laser frequencies by $2\pi \times 3.45$ MHz $= \omega_{\mathrm{stretch}} + \delta$ with $\delta = -2\pi \times 250$ kHz. This choice avoids several technical problems of the original proposal [2] (see methods), while at the same time, resonantly enhancing the effective spin-spin interaction by a factor of $|\omega_{\mathrm{stretch}}/\delta| = 14.8$ compared to the standing wave case [19].

After laser cooling we initialise the quantum simulator by optical pumping [20] to the state $|\downarrow\rangle|\downarrow\rangle\,|n \cong 0\rangle$. We rotate both spins in a superposition state via a $R(\pi/2, -\pi/2)$-pulse (see Eq. 2) on the rf-transition to initialise the state $\Psi_\mathrm{i} = |{\rightarrow}\rangle|{\rightarrow}\rangle|n \cong 0\rangle$. Note that this paramagnetic state $|{\rightarrow}\rangle|{\rightarrow}\rangle \equiv (|\uparrow\rangle + |\downarrow\rangle)(|\uparrow\rangle + |\downarrow\rangle) = |\uparrow\uparrow\rangle + |\uparrow\downarrow\rangle + |\downarrow\uparrow\rangle + |\downarrow\downarrow\rangle$ has a 25% probability to be projected into either $|\uparrow\uparrow\rangle$ or $|\downarrow\downarrow\rangle$ (normalisation factors are suppressed throughout).

We simulate the effective magnetic field by continuously applying a radio-frequency field with phase $\phi = 0$ and an amplitude such that it corresponds to a single qubit rotation $R(\Theta, 0)$ with full rotation period $\Theta = 2\pi$ in 118 µs and deduce $B_x = 2\pi \times 4.24$ kHz. Precise control of the phase ϕ of the rf-oscillator relative to the initialisation pulse allows to align B_x parallel to the spins along the x-axis in the equatorial plane of the Bloch sphere, ensuring that $|\Psi_\mathrm{i}\rangle$ is an eigenstate of this effective magnetic field.

At the same time, we switch on the effective spin-spin interaction $J(t)$ ($t \in [0;T]$) and increase its amplitude adiabatically up to $J(T)$. At time T, we switch off the interactions and analyse the final state of the two spins via the state sensitive detection described above. In a sequence of experiments at constant B_x we increase T and therefore $J(t)/B_x$. After 50 steps of 2.5 µs each we reach the maximal amplitude $J(t = 125\ \mu\mathrm{s})/B_x = J_{\max}/B_x = 5.2$ (see methods) and achieve a quantum-magnetisation $\mathcal{M} = P_{\downarrow\downarrow} + P_{\uparrow\uparrow}$, the probability of being in a state with ferromagnetic order, of $\mathcal{M} = (98 \pm 2)\%$.

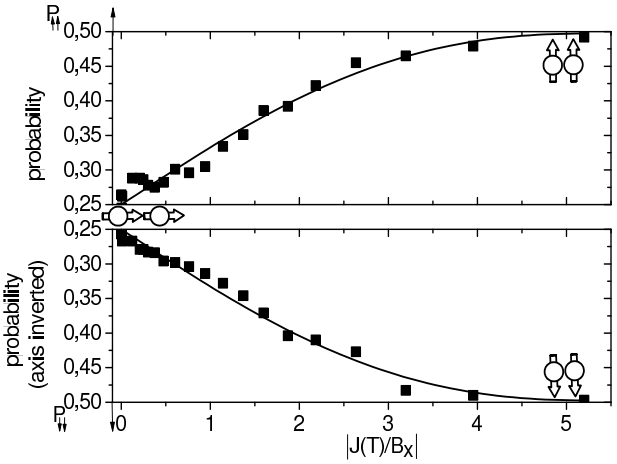

FIG. 3: Quantum magnetisation of the spin system: We initialise the spins in the paramagnetic state $|{\rightarrow}\rangle|{\rightarrow}\rangle = (|\uparrow\rangle + |\downarrow\rangle)(|\uparrow\rangle + |\downarrow\rangle) = |\uparrow\uparrow\rangle + |\uparrow\downarrow\rangle + |\downarrow\uparrow\rangle + |\downarrow\downarrow\rangle$, the ground state of the Hamiltonian $H_\mathrm{B} = -B_x(\sigma_1^x + \sigma_2^x)$. A measurement of this superposition state would already project into each $|\uparrow\uparrow\rangle$ and $|\downarrow\downarrow\rangle$ with a probability of 0.25. After applying B_x we adiabatically increase the effective spin-spin interaction $J(t = 0) = 0$ to $J(T)$. State sensitive fluorescence detection allows to distinguish the final states $|\uparrow\uparrow\rangle$, $|\downarrow\downarrow\rangle$, $|\uparrow\downarrow\rangle$ or $|\downarrow\uparrow\rangle$. Averaging over 10^4 experiments provides us with its probability distribution $P_{\downarrow\downarrow}$ (two ions fluoresce), $P_{\uparrow\uparrow}$ (no ions fluoresces), and $P_{\uparrow\downarrow}$ or $P_{\downarrow\uparrow}$ (one ion fluoresces). We repeat the measurement for increasing ratios $J(T)/B_x$. The experimental results for the ferromagnetic contributions $P_{\uparrow\uparrow}$ and $P_{\downarrow\downarrow}$ are depicted as squares, the solid lines representing the theoretical prediction. For $J(T)/B_x \ll 1$, the paramagnetic order is preserved. For $J(T)/B_x \gg 1$, the spins undergo a transition into the ferromagnetic order, the ground state of the Hamiltonian $H_\mathrm{J} = J_{\max}\sigma_1^z\sigma_2^z$, with a related quantum magnetisation $\mathcal{M} = P_{\downarrow\downarrow} + P_{\uparrow\uparrow}$ of $\geq (98 \pm 2)\%$. Note that we invert the ordinate of the lower frame to emphasise the unbroken symmetry of the evolution.

After the adiabatic evolution described above, we project the final spin state into the σ^z-measurement basis by a laser beam tuned resonantly to the $|\downarrow\rangle \leftrightarrow {}^2\mathrm{P}_{3/2}\,|F = 4, m_f = 4\rangle$ cycling transition [14]. An ion in state $|\downarrow\rangle$ fluoresces brightly, leading to the detection of on average 40 photons during a 160 µs detection period with our photo multiplier tube. In contrast, an ion in state $|\uparrow\rangle$ remains close to dark (on average 6 photons). We repeat each experiment for the same set of parameters 10^4 times and derive the probabilities $P_{\downarrow\downarrow}, P_{\uparrow\uparrow}$ and $P_{\downarrow\uparrow}$ for the final state being projected into state $|\downarrow\downarrow\rangle$, $|\uparrow\uparrow\rangle$ and $|\downarrow\uparrow\rangle$ or $|\uparrow\downarrow\rangle$, respectively (and further described in methods).

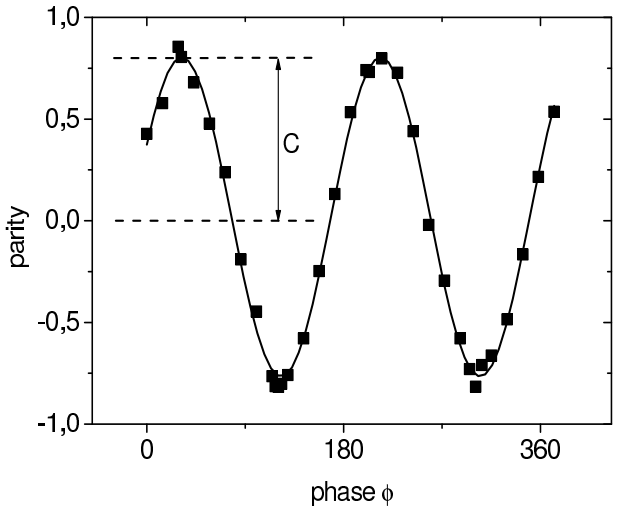

FIG. 4: Entanglement of the quantum magnet: Measurement of the parity $\mathcal{P} = P_{\downarrow\downarrow} + P_{\uparrow\uparrow} - (P_{\downarrow\uparrow} + P_{\uparrow\downarrow})$ of the final ferromagnetic state after the simulation reached $J_{\max}/B_x = 5.2$. As we vary the phase ϕ of a subsequent analysis pulse $R(\pi/2, \phi)$, the parity of the two spins oscillates as $C\cos(2\phi)$. Together with the final state populations $P_{\downarrow\downarrow}$ and $P_{\uparrow\uparrow}$ depicted in FIG. 3, we can deduce the Bell state fidelity $\mathcal{F} = 1/2(P_{\downarrow\downarrow} + P_{\uparrow\uparrow}) + C/2$ of $(88 \pm 3)\%$ for the final superposition state $|\uparrow\uparrow\rangle + |\downarrow\downarrow\rangle$, a maximally entangled state, highlighting the quantum nature of this transition. We find qualitatively comparable results for the antiferromagnetic case $|\uparrow\downarrow\rangle + |\downarrow\uparrow\rangle$. Each data point averages 10^4 experiments.

IV. ENTANGLEMENT

In our experiment we can detect both ferromagnetic contributions, $P_{\uparrow\uparrow}$ and $P_{\downarrow\downarrow}$, separately. Any imperfection in the simulation acting as a bias field B_z along the z-axis, would energetically prefer one of the ferromagnetic states over the other and therefore unbalance their contribution to the final state. We carefully cancel all bias fields (see methods) to balance the populations $P_{\uparrow\uparrow}$ and $P_{\downarrow\downarrow}$, as can be seen in FIG. 3. The results are in good agreement with theoretical predictions for our experiment, shown as solid lines. We expect the final state to be a coherent superposition of the two ferromagnetic states $|\uparrow\uparrow\rangle + |\downarrow\downarrow\rangle$, a maximally entangled Bell state. To quantify the experimentally reached coherence we measure the parity [21] $\mathcal{P} = P_{\downarrow\downarrow} + P_{\uparrow\uparrow} - (P_{\downarrow\uparrow} + P_{\uparrow\downarrow})$ after applying an additional $R(\pi/2, \phi)$-pulse to both ions after $J_{\max}$ is reached, with a variable rf-phase ϕ relative to the rf-field simulating B_x. The measured data shown in FIG. 4 have a component that oscillates as $C\cos(2\phi)$, where $|C|/2$ characterises the coherences between the $|\uparrow\uparrow\rangle$ and $|\downarrow\downarrow\rangle$ components in the state produced. Deducing a contrast C of (78±2)% from the best-fit we derive the Bell state fidelity [21] $\mathcal{F} = 1/2(P_{\downarrow\downarrow} + P_{\uparrow\uparrow}) + C/2$ of $(88 \pm 3)\%$.

We also simulate the adiabatic evolution of a system not initialised in the ground state of the initial Hamiltonian. In particular we prepare the paramagnetic eigenstate $|\leftarrow\leftarrow\rangle = (|\downarrow\rangle - |\uparrow\rangle)(|\uparrow\rangle - |\downarrow\rangle)$, with the spins aligned anti-parallel with respect to the simulated magnetic field via a $R(\pi/2, \pi/2)$ rf-initialisation pulse. The adiabatic evolution should preserve the spin system in its excited state leading now into the anti-ferromagnetic order $|\uparrow\downarrow\rangle + |\downarrow\uparrow\rangle$. After evolution to $J = J_{\max}$ we find $P_{\downarrow\uparrow} + P_{\uparrow\downarrow} \geq (95 \pm 2)\%$. To investigate the coherence between the $|\downarrow\uparrow\rangle$ and the $|\uparrow\downarrow\rangle$ components, we first rotate the state via an additional $R(\pi/2, 0)$-pulse which would ideally take $|\uparrow\downarrow\rangle + |\downarrow\uparrow\rangle \longrightarrow |\uparrow\uparrow\rangle + |\downarrow\downarrow\rangle$, followed by the measurement of the parity as explained above. We deduce a lower bound for the fidelity of the anti-ferromagnetic entangled state $\mathcal{F} = \left|\langle\Psi_{\text{final}}| \downarrow\uparrow + \uparrow\downarrow\rangle\right|^2 = 1/2\,(P_{\uparrow\downarrow} + P_{\downarrow\uparrow}) + C/2$ of $(80 \pm 4)\%$.

An equally valid viewpoint of this experiment interprets $|\leftarrow\leftarrow\rangle$ as the ground state of the Hamiltonian $-H_{\text{Ising}}$. Because the sign of all spin-spin interactions is also reversed in $-H_{\text{Ising}}$ it is equivalent to a change of sign in the spin-spin interaction J.

The entanglement of the final states confirms that the transition from paramagnetic to (anti-) ferromagnetic order is not caused by thermal fluctuations driving thermal phase transitions. The evolution is coherent and quantum mechanical, the coherent counterpart to the so-called quantum fluctuations [3, 15] driving quantum phase transitions in the thermodynamic limit. In this picture tunnelling processes [15] induced by B_x coherently couple the degenerate (in the rotating frame) states $|\uparrow\rangle$ and $|\downarrow\rangle$ with an amplitude proportional to $(B_x/|J|)$. In a simplified picture for N spins the amplitude for the tunnelling process between $\Psi_{N\uparrow} = |\uparrow\uparrow \ldots \uparrow\rangle$ and $\Psi_{N\downarrow} = |\downarrow\downarrow \ldots \downarrow\rangle$ is proportional to $(B_x/|J|)^N$, since all N spins must be flipped. In the thermodynamic limit $(N \to \infty)$ the system is predicted to undergo a quantum phase transition at $|J| = B_x$. At values $J > B_x$ the tunnelling between $\Psi_{\infty\uparrow}$ and $\Psi_{\infty\downarrow}$ is completely suppressed. In our case of a finite system $\Psi_{2\uparrow}$ and $\Psi_{2\downarrow}$ remain coupled and the sharp quantum phase transition is smoothed into a gradual change from paramagnetic to (anti-)ferromagnetic order.

V. CONCLUSION AND OUTLOOK

We demonstrated the feasibility of simple quantum simulations in an ion trap by implementing the Hamiltonian of a quantum magnet undergoing a robust transition from a paramagnetic to an entangled ferromagnetic or anti-ferromagnetic order. While our system is currently too small to solve classically intractable problems, it uses an approach that is complementary to a universal quantum computer in a way that can become advantageous as the approach is scaled to larger systems. Since our scheme only requires inducing the same overall spin-dependent optical force on all the ions [2], it does not rely on the use of sequences of quantum gates, thus its scaling to a higher number of ions can be simpler. Furthermore the desired outcome might not be affected by decoherence

as drastically as typical quantum algorithms, because a continuous loss of quantum fidelity might not spoil completely the outcome of the experiment (for example the (anti-)ferromagnetic ordering transitions are hardly affected by phase decoherence), while universal quantum computation will almost certainly require involved subagorithms for error correction [4]. Decoherence in the simulator might even mimic the influence of the natural environment [22] of the studied system, if we judiciously construct our simulation (for example the decoherence we mainly observe in our demonstration implements a dephasing environment).

Despite technical challenges, we expect that this work is the start to extensive experimental research of complex many-body phases with trapped ion systems. Linear trapping setups may be used for the quantum simulation of quantum dynamics beyond the ground state where chains of 30 spins would already allow to outperform current simulations with classical computers. We may also adapt our scheme to new ion trapping technologies [13]. For example, a modest scaling to systems of 20×20 spins in 2D would yield insight into open problems in solid state physics, e.g. related to spin-frustration. This could pave the way to address a broad range of fundamental issues in condensed matter physics which are intractable with exact numerical methods, like, for example, spin liquids in triangular lattices, suspected to be closely related to phases of high-T_c superconductors [23].

Acknowledgments

This work was supported by the Emmy-Noether Programme of the German Research Foundation (DFG, Grant No. SCHA 973/1-2), the MPQ Garching, the DFG Cluster of Excellence Munich-Centre for Advanced Photonics, and the European project SCALA. We thank Dietrich Leibfried for his invaluable input and Ignacio Cirac and Gerhard Rempe for most interesting comments and generous support.

[1] R. P. Feynman, Int. J. Theo. Phys. **21**, 467 (1982).
[2] D. Porras and J. I. Cirac, Phys. Rev. Lett. **92**, 207901 (2004).
[3] S. Sachdev, *Quantum Phase Transitions* (Cambridge University Press, 1999).
[4] M. Nielsen and I. Chuang, *Quantum Computation and Quantum Information* (Cambridge University Press, 2000).
[5] see for example: `http://qist.lanl.gov/qcomp_map.shtml`.
[6] D. P. DiVincenzo, in *Scalable quantum computation*, edited by S. Braunstein, H. Lo, and P. Kok (Wiley, 2001).
[7] D. Leibfried, E. Knill, S. Seidelin, J. Britton, R. B. Blakestad, J. Chiaverini, D. B. Hume, W. M. Itano, J. D. Jost, C. Langer, et al., Nature **438**, 639 (2005).
[8] H. Häffner, W. Hänsel, C. F. Roos, J. Benhelm, D. C. al kar, M. Chwalla, T. Körber, U. Rapol, M. Riebe, P. Schmidt, et al., Nature **438**, 643 (2005).
[9] J. Benhelm, G. Kirchmair, C. F. Roos, and R. Blatt, Nature Physics (2008).
[10] M. Greiner, O. Mandel, T. Esslinger, T. Hänsch, and I. Bloch, Nature **415**, 39 (2002).
[11] D. Porras and J. I. Cirac, Phys. Rev. Lett. **93**, 263602 (2004).
[12] D. J. Wineland, M. Barrett, J. Britton, J. Chiaverini, B. L. DeMarco, W. M. Itano, B. M. Jelenkovic, C. Langer, D. Leibfried, V. Meyer, et al., Phil. Trans. R. Soc. Lond. A **361**, 1349 (2003).
[13] J. Chiaverini and W. E. Lybarger, quant-ph/0711.0233 (2007).
[14] D. J. Wineland, C. Monroe, W. Itano, D. Leibfried, B. King, and D. Meekhof, J. Res. Natl. Inst. Stand. Technol. **103**, 259 (1998).
[15] S. Sachdev, Science **288**, 475 (2000).
[16] T. Schätz, A. Friedenauer, H. Schmitz, L. Petersen, and S. Kahra, J. Mod. Opt. **54**, 2317 (2007).
[17] L. Allen and J. H. Eberly, *Optical Resonance and Two-Level Atoms* (Dover, New York, 1987).
[18] D. Leibfried, B. DeMarco, V. Meyer, D. Lucas, M. Barrett, J. Britton, W. Itano, B. Jelenkovic, C. Langer, T. Rosenband, et al., Nature **422**, 412 (2003).
[19] D. Porras and J. I. Cirac, arXiv, quant-ph/0601148v3 (2006).
[20] B. E. King, C. Wood, C. Myatt, Q. Turchette, D. Leibfried, W. Itano, C. Monroe, and D. Wineland, Phys. Rev. Lett. **81** (1998).
[21] C. Sackett, D. Kielpinski, B. King, C. Langer, V. Meyer, C. Myatt, M. Rowe, Q. Turchette, W. Itano, D. J. Wineland, et al., Nature **404**, 256 (2000).
[22] S. Lloyd, Science **273**, 1073 (1996).
[23] J. Orestein and A. J. Millis, Science **288**, 468 (2000).